Two-Dimensional Transition Metal Dichalcogenides for Near Infrared Photodetection with an Eye toward Retinal Electrophysiology

By

Thayer S. Walmsley

Dissertation

Submitted to the Faculty of the

Graduate School of Vanderbilt University

in partial fulfillment of the requirements

for the degree of

DOCTOR OF PHILOSOPHY

in

Physics

August 13th, 2021

Nashville, Tennessee

Approved:

Deyu Li, Ph.D.

Norman Tolk, Ph.D.

Sait Umar, Ph.D.

Sharon Weiss, Ph.D.

Yaqiong Xu, Ph.D.

Copyright © 2021 by Thayer Walmsley

All Rights Reserved

This work is dedicated to my loving and supporting wife, Aubri, and my precious pup of a writing partner, Ollie.

ACKNOWLEDGEMENTS

I would first and foremost like to thank my advisor Dr. Yaqiong Xu. She welcomed me into her research group with open arms and has been incredibly understanding, helpful and supportive ever since. She has gone above and beyond to ensure that my aspirations are realized. Her ability to challenge me to thoroughly understand and explore results have honed my scientific and reasoning skills. Additionally, I would like to thank my committee. Dr. Deyu Li has been incredibly impactful in helping me explore the biological considerations of 2D materials. Dr. Sharon Weiss has helped me consider novel 2D properties in well understood 3D phenomena. And the coursework as well as advice offered by Dr. Sait Umar and Dr. Norman Tolk have been instrumental in my development as a physicist. The perspective of a first principle examination imparted by Dr. Umar and the push from Dr. Tolk toward seeing applications (and his appreciation and support for taking my scientific expertise into the legal realm) have helped me tremendously.

My wife, Aubri Walmsley, has been instrumental in enabling my studies and her enduring love has been critical to my success. None of this would have been possible without her. I would also like to thank my mother, Jill Walmsley, and my father, Dr. G. Storm Walmsley, for supporting me and inspiring to pursue my dreams. Without them I wouldn't be the success that I am today. They have always been there to celebrate my achievements and help me overcome my failures. Numerous other members of my family have not only encouraged me but also sparked and flamed my interest in science. Both my grandfathers, Dr. George L. Walmsley and Keith Thayer have been instrumental in my passion for hard work and innovation. My uncle Joey Thayer has also played a pivotal role in my love for chemistry.

I am immensely appreciative for all my fellow group members in Dr. Xu's Lab who contributed to my experimental work and engaged in helpful scientific discussions. Tu Hong, Tianjiao Wang, and

Yuchen Zhang have been excellent mentors. Xiaosi Zhang and Christian D. Ornelas have been wonderful friends and contemporaries. I would also like to thank my friends outside of the lab. I wouldn't have made it through my first two years without my wonderful and supportive office mates, Benjamin Hardy and Brook Musangu. The constant support and encouragement from my friends Tye and Shannon Haas as well as Jackson and Kalee Daugherty were vital in making it through tough weeks.

Our collaborators who enabled this work also deserve significant thanks. The device fabrication and assistance from Dr. Kraig Andrews, Dr. Arthur Bowman, and Dr. Upendra Rijal under the direction of Dr. Zhixian Zhou have been critical to exploring NIR photodetection in 2D TMDCs. Additionally, Dr. Edward Levine and Dr. Hannah Lee have been indispensable in exploring retina electrophysiology through tissue preparation and biological insights.

Additionally, the facilities and personnel at Vanderbilt Institute of Nanoscale Science and Engineering (VINSE) have been instrumental. Dr. Dmitry Koktysh, Dr. Alice Leach, Dr. Bill Martinez, and Dr. Anthony Hmelo have been instrumental to my work. I would also like to thank the National Science Foundation and the National Institute of Health, without their financial support none of this work would have been possible.

PREFACE

This dissertation chronicles the quest to find suitable two-dimensional (2D) transition metal dichalcongeindes (TMDCs) for near infrared (NIR) photodetection while also considering retinal electrophysiology. Chapter 1 offers an introduction to 2D materials and TMDCs with an overview of NIR photodetection. Additionally, given the recurrent experimental setup and discussion of photocurrent generation mechanisms in Chapters 2, 3, and 4 these topics are also discussed in the general introduction offered by Chapter 1. Chapters 2, 3, and 4 presents work that explored the electrical and optoelectronic properties of different devices based on 2D TMDC materials ($PdSe_2$), structures (BP-MoS_2 vertical junction), and phases (CDW phase of 1T-$TiSe_2$) with more detailed relevant introductory material. Chapter 5 then turns to a biological application and the status of retina electrophysiology with an emphasis on demonstrating expected results and robust protocols for custom microelectrode arrays. Chapter 6 concludes by summarizing key results and suggesting that data science can play a pivotal role in overcoming some hurdles to the scaling of 2D materials.

TABLE OF CONTENTS

ACKNOWLEDGEMENTS iii
PREFACE vi
LIST OF TABLES ix
LIST OF FIGURES x
LIST OF PUBLICATIONS xvii
Chapter 1 Introduction to 2D Transition Metal Dichalcogenides and Scanning Photocurrent Microscopy 1
1.1 Introduction to 2D Materials and Transition Metal Dichalcogenides (TMDCs) 1
1.2 Near Infrared Photodetection 6
1.3 Scanning Photocurrent Microscopy (SPCM) 9
1.3.1 Experimental Setup 10
1.4 Photocurrent Generation Mechanisms 11
Chapter 2 NIR Light-Matter Interactions in 2D Phototransistors 16
2.1 Introduction to Metal-Semiconductor Junctions 16
2.2 $PdSe_2$ Phototransistors 17
2.2.1 Results and Discussion 19
Chapter 3 NIR Detection Using Van-der Waals Heterojunctions 34
3.1 Introduction to Van-der Waals Heterojunctions 34
3.2 BP-MoS_2 Heterojunctions 37
3.2.1 Results and Discussion 39
3.3 $MoSe_2$ Based Heterojunctions 52
Chapter 4 Charge Density Wave Materials for NIR Detection 55
4.1 Introduction to Charge Density Wave States and $TiSe_2$ 55
4.2 $TiSe_2$-Metal Junctions 59
4.2.1 Device Fabrication 60
4.2.2 Results and Discussion 67
Chapter 5 Retina Electrophysiology 78
5.1 Introduction to Retina Electrophysiology 78
5.2 Results and Discussion 83
5.3 Pressure Devices 92
Chapter 6 Conclusion and Future Outlook 96

6.1 Discoveries in NIR TMDC Photodetection 96
6.2 Perspective on 2D Material Devices 97
APPENDIX 100
A.1 Laser Optical Path 100
A.2 Electrode Preparation 101
A.3 Substrate Preparation 101
A.4 Electrode Transfer 101
A.5 Electron Beam Lithography (EBL) to Enable Wire Bonding and Finishing Devices 102
A.6 Retina Electrophysiology Setup 105
A.7 Retina Preparation and Experimental Protocols 106
A.7.1 K^+ Stimulation Protocol 107
A.7.2 Light Stimulation Protocol 107
REFERENCE 108

LIST OF TABLES

Table 3.1 Summary of BP, MoS_2, and BP-MoS_2 Heterojunction Response Times. 38

Table 4.1 Summary of 2D TMDC CDW and Superconducting Phase Transitions...................... 57

LIST OF FIGURES

Figure 1.1 Material Dimensionality. The 3D, 2D, 1D, and 0D allotropes of carbon are shown as graphite, graphene, a carbon nanotube, and a fullerene in (a), (b), (c), and (d), respectively. The added black arrows signify the number and direction of dimensions General forms of the density of states for 3D, 2D, 1D, and 0D states are shown in (e), (f), (g), and (h). The blue shows the representative dimension with the higher dimension traced in gray. (a) and (b), are reproduced under (CC0 1.0) and (CC BY 2.5), from Mattman723 and Zhantongz, respectively. (c) and (d) are reproduced under (CC BY 3.0) from Mstroeck. (e) – (h) are reproduced from Ref. [6] under (CC BY 4.0). 2
Figure 1.2 2D Transition Metal Dichalcogenides. (a) Periodic table highlighting some significant elements for 2D materials. (b) and (c) ball and stick models representing the popular TMDC MoS_2 and graphene analog for phosphorus, respectively. (d) Diagram of the characteristic X – M – X structure as well as the common 1T and 2H phases for TMDCs. (a) – (c) Reproduced with from Ref [10] under (CC BY 4.0). (d) Reproduced with permission from Ref. [11]. Copyright © 2015 American Chemical Society. This is an unofficial adaptation of an article that appeared in an ACS publication. ACS has not endorsed the content of this adaptation or the context of its use. 3
Figure 1.3 Publication Perspectives on 2D Materials. (a) Total number of published article on 2D materials. (b) Total number of published articles on optoelectronics and photonics. (c) Portion of articles for specified 2D materials other than graphene from (b). Data collected from the Web of Science as of April 2019. Reproduced from Ref. [22] under (CC BY 3.0). 5
Figure 1.4 Varied Band Gaps in 2D Materials. Reproduced from Ref [7], under (CC BY 4.0).5
Figure 1.5 The Electromagnetic Spectrum. Public domain image reproduced from NASA JPL. 6
Figure 1.6 NIR Biological Windows. (a) Penetration depth in the first (in red) and second (in gray) biological windows with respective to certain aspects of biological tissue. (b) Comparison of standard NIR photodetectors with respect to the two NIR biological windows. Reprinted with permission from Ref [23]. Copyright © 2009 Macmillan Publishers Limited. 8
Figure 1.7 Scanning Photocurrent Setup. Schematic presenting the crucial elements that enable the electrical and optoelectronic characterization of the 2D TMDC devices discussed in this work........ 11
Figure 1.8 Relevant Photocurrent Generation Mechanisms. Schematic representation of photocurrent-generation mechanisms in semiconducting 2D materials. M and S indicate metal electrode contacts and 2D semiconductor channels, respectively. (a) Photon-excited electron-hole pairs (EHPs) separated by internal electric fields at metal-semiconductor Schottky barriers. Red shaded areas indicate an elevated temperature ΔT induced by laser heating, leading to (b) a voltage difference ΔV_{PTE} or (c) overall conductance change ΔG across the channel. Image and caption adapted and reprinted under (CC BY 4.0) from Ref [27]. 12
Figure 1.9 Examples of PVE, PTE and PBE Induced Photocurrent Signals. (a) Relative dominance of the PVE ($V_G < 0V$)and PBE ($V_G > 0V$) in a BP integrated Si waveguide. (b) and (c) show photocurrent signals in a non-uniform WSe_2 double gated phototransistor. (b) Above band gap illumination showing PVE dominance in PN and NP regions as well as the PTE in the PP region. (c) Below band gap illumination confrimng the PTE for the PP region. (a) is reproduced with permission from Ref [31]. Copyright © 2015 Macmillan Publishers Limited. (b) and (c) are reproduced with permission from Ref [32]. Copyright © 2014 American Chemical

Society.. 15
Figure 2.1 Metal-Semiconductor Junction Schematic (a) A metal and N-type semiconductor before coming into contact. (b) A metal-semiconductor with a Schottky barrier height governed by the Schottky-Mott rule. 17
Figure 2.2 Puckered Pentagonal Structure of $PdSe_2$. (a) Regular pentagons tessellated in a plane. (b) Puckered pentagonal arrangement in $PdSe_2$. Pd and Se atoms are represented by gray and yellow balls, respectively. (b) reproduced with permission from Ref. [43]. Copyright © 2017 American Chemical Society. 18
Figure 2.3 Comparison of Puckered strucutres in BP and $PdSe_2$. (a) Puckcered hexagonal structure of BP. (b) Puckered pentagonal structure of $PdSe_2$. (a) and (b) reproduced with permission from Ref. [43]. Copyright © 2017 American Chemical Society. 19
Figure 2.4 $PdSe_2$ Phototransistors. (a) A schematic of the $PdSe_2$ device. (b) An optical image of the as-fabricated $PdSe_2$ device. The $PdSe_2$ flake is outlined in a purple dashed lines and the electrodes are outlined in gray dashed lines. The scale bar is 5 µm. 21
Figure 2.5 Electrical Transport of $PdSe_2$ Phototransistors. (a) Gate-dependent electrical transport of the PdSe2 phototransistor. On/off characteristics seen by the right log scaled y-axis in red. (b) The output characteristics of the device at various gate voltages. 22
Figure 2.6 Schottky Barrier Height Extraction. (a) The Arrhenius plots for several back-gate bias voltages measured with drain voltage bias at 100 mV. The slope of each curve yields the effective Schottky barrier height at the corresponding gate bias. (b) The extracted effective Schottky barrier height at the various back-gate bias voltage, where the flatband electron Schottky barrier height is measured to be 180 meV. 23
Figure 2.7 SPCM of $PdSe_2$ Phototransistors. (a) Reflection and (b) scanning photocurrent images of a typical $PdSe_2$ phototransistor under 1060 nm illumination as well as zero back gate and zero drain–source bias. Metal electrodes and few-layer $PdSe_2$ channel are outlined by gray and purple dashed lines, respectively. The horizontal scale bars in (a) and (b) are 5 microns. (c) Gate-dependent photocurrent signals along the vertical black dashed line in (b). In (c), the vertical direction is y position and the horizontal direction is back gate voltage. The corresponding scale bars are 2.5 microns and 10 V, respectively. (e) Green and black curves represent photocurrent responses along the green and black dotted lines in (c), respectively. 25
Figure 2.8 Band Bending Conditions of $PdSe_2$ Phototransistors. Schematic of the band bending in the $PdSe_2$ in response to a back gate voltage showing below the flat band voltage in (a) when the material is electrostatically n-doped, the flat band condition in (b), above the flat band voltage in (c) when the material is electrostatically p-doped. 26
Figure 2.9 Thermal Photocurrent Generation Analysis in $PdSe_2$ Phototransistors. (a) Conductance of a $PdSe_2$ device as a function of temperature; (b) photocurrent response of the device as a function of drain-source bias (red dots represent experimental data and black line is a linear fitting); and (c) a line profile of the photocurrent response across the metal-PdSe2 junction is shown by the black dots. The red solid curve is the related Gaussian fitting. The green arrow denotes the photocurrent "tail" on the electrode. The yellow background indicates the position of the electrode. 27
Figure 2.10 Wavelength Dependence of $PdSe_2$ Phototransistors. (a) Wavelength dependent photocurrent response for various devices thicknesses under zero back gate voltage and zero drain-source bias. Each layer of $PdSe_2$ is ~0.6 nm resulting in corresponding thicknesses of ~5.4nm (9L), ~9nm (15L), ~16.8 nm (28L) and ~19.8nm (33L). 29
Figure 2.11 Analysis of Potential Distributions in $PdSe_2$ Phototransistors. (a) Scanning

photocurrent images (20 μm by 20 μm) taken with drain–source biases from 150mV to -150 mV in increments of 50mV excluding the zero bias image and under zero back gate voltage. The scale bar is 5 microns. The electrodes of the device are outlined in gray. The $PdSe_2$ flake is outlined in purple dashed lines. (b) Corresponding photocurrent intensity along the black dashed lines in (a). (c) Electrostatic potential computed by numerically integrating the photocurrent intensity curves from (b). 31
Figure 2.12 Photoresponse Dynamics and Power Dependence of $PdSe_2$ Phototransistors. (a) Photocurrent signals as a function of time under 1060 nm illumination. (b) Zoom-in of the rising and decaying regions of the photocurrent signals from (a) showing the rise and decay time constants of ∼156 μs and ∼163 μs, respectively. (c) Power-dependent photocurrent behavior of the device, where the red solid line shows the trend line of $I_{PC} \propto P^{0.85}$. 32
Figure 3.1 LEGO Building Approach to 2D Materials. Schematic illustrating the concept of 2D material Lego Building. Reprinted with permission from Ref [71]. Copyright © 2013 Macmillan Publishers Limited. 34
Figure 3.2 Comparison of Vertical and Lateral Heterojunctions. (a) – (d) Schematic and imaging of a vertical 2D TMDC heterostructure. (e) – (h) Schematic and imaging of a horizontal 2D TMDC heterostructure. Both hterostuctures are grown via chemical vapor deposition. Reprinted with permission from Ref [77]. Copyright © 2014 Macmillan Publishers Limited. ... 35
Figure 3.3 Summary of the numerous 2D HeteroStructures. Schematics of a lateral (a) vs vertical (b) heterojunction. Reprinted with permission from Ref [82]. Copyright © 2020 Wiley-VCH GmbH. 36
Figure 3.4 BP-MoS_2 Heterojunctions. (a) A schematic of the BP-MoS_2 heterojunction device. (b) An optical image of the as-fabricated device. BP and MoS_2 are outlined in purple and blue dashed lines, respectively. The electrodes are outlined in gray dashed lines. The scale bar is 10 μm. 41
Figure 3.5 Electrical Transport Properties in BP-MoS_2 Heterojunctions. (a) Gate-dependent transport characteristics of the BP (black) and MoS_2 (red) channels of the device, respectively. (b) The electrical transport properties of the heterojunction under various gate voltages. 42
Figure 3.6 SPCM and Power Dependence of BP–MoS_2 Heterojunctions. (a) The reflection and f) scanning photocurrent images of the BP–MoS_2 heterojunction under a zero drain-source bias and zero gate voltage. The gray dashed lines show the outline of the electrodes. The purple and blue dashed lines represent BP and MoS_2 flakes, respectively. 43
Figure 3.7 Photocurrent Generation in BP–MoS_2 Heterojunctions. Band diagram for the BP-MoS_2 heterojunction under (a) 650nm and (b) 1000 nm wavelength illumination. (c) Gate-dependent output characteristics under no illumination (black), 650nm illumination (red) and 1000nm illumination (blue). (d) Drain-Source bias dependent measurement under no illumination (black), 650nm illumination (red) and 1000nm illumination (blue). The yellow region highlights the PVE. 45
Figure 3.8 Photoresponse Dynamics in BP–MoS_2 Heterojunctions. (a) Photocurrent response as function of time under 650nm wavelength illumination while light is modulated on and off by an optical chopper at 200 Hz. The heterojunction is under -20V back-gate voltage. A zoom in of the rising (b) and decaying (c) of the photocurrent response at 650nm (black squares) and 1000nm (maroon circles). The same optical chopper frequency of 200 Hz is used and the device is under -20V back-gate voltage. 46
Figure 3.9 Tunable Photoresponse Speed in BP–MoS_2 Heterojunctions.(a) Rise and (b) decay constants as a function of wavelength and gate voltage. (c) Simplified energy band

diagram of the MoS_2-Au contact. Red, black, and blue curvature correspond to the behavior of back-gate voltages of -20V, 0V, and 20V, respectively. 47
Figure 3.10 Band diagram of BP–MoS_2 Heterojunction . Band diagram for the BP-MoS_2 heterojunction under (a) 1000 nm and (b) 650 nm wavelength illumination. The band gap of BP is ~0.3 eV and the respective E_F - E_V is 0.1 eV. The band gap of the MoS_2 is ~1.9 eV and the respective $E_C – E_F$ is 0.2 eV. [83, 122] 48
Figure 3.11 $MoSe_2$-Based Heterojunction (a) Optical micrograph outlining the constituent 2D materials. (b) Electrical transport properties of the device. Inset shows the linear ohmic nature of the device at different gate voltages (c) Representative photocurrent mapping of the device under -30mV bias and at 780nm wavelength illumination. (d) Wavelength dependence of the photocurrent response at their respective junctions. 52
Figure 3.12 Bias and Time Dependent Photocurrent Response in $MoSe_2$ based Heterojunctions. Bias and power depdenet photocurrent itensity under 650nm wavelength illumination for the (a) MoS_2 and the (b) WSe_2 side of the $MoSe_2$ heterojunctions. Temporally resolved photocurrent measurements under 650nm wavelength illumination showing fast response times for both the (c) MoS_2, under 0 mV drain-source bias, and the (d) WSe_2, under -30 mV drain-source bias, side of the $MoSe_2$ heterojunctions. 54
Figure 4.1 Energy Bands and Atomic Spacing for Normal and CDW State for a 1D crystal. Illustration for normal state (a) and CDW State (b) energy bands and atomic spacing for a 1D crystal (temperature above the transition temperature). Reproduced under (CC BY 4.0) from Ref [133]. 56
Figure 4.2 Illustration of commensurate and Incommensurate CDW. (a) Commensurate and (b) Incommensurate CDW states depeicted in 1D. Purple dashed lines indicate the increased atomic spacing arising from Figure 4.1b. 56
Figure 4.3 Phase Diagram for 1T-$TiSe_2$. The phase diagram created from measurements on hBN encapsulated thin (< 10nm) ion gel top gated $TiSe_2$ FETS. Reproduced with permission from Ref [143]. Copyright © 2016 Macmillan Publishers Limited. 59
Figure 4.4 Comparison of Transferred and Deposited Gold on 2D Materials. (a) – (c) Cross-sectional schematics and TEM images of transferred Au electrodes on top of MoS_2. (d) Optical image of the MoS_2 device with transferred electrodes (upper) and with the transferred electrodes mechanically released (lower). (e) – (g), Cross-sectional schematics and TEM images of conventional electron-beam-deposited Au electrodes on top of MoS_2. (h), Optical image of a MoS_2 flake with deposited electrodes (upper) and with the deposited electrodes mechanical released (lower). Image (a), (b), (c), (d), (e), (f), (g), and (h) reprinted with permission from Ref [35]. Copyright © 2018, Macmillan Publishers Ltd., part of Springer Nature. 63
Figure 4.5 Schematic of the Gold Transfer Procedure The preparation of the electrodes is shown in (a) and (b). (d) and (c) are the two steps that culmniate in the device fabrication shown in (e). The final step that is required to enable wire bonding to the device is shown in (f). 65
Figure 4.6 Basic Electrical and Optolectroinc Characterization of Gold Transferred Graphene FETs. Fabrication of graphene FET using the gold transfer procedure. (a) Optical image of the finished device. Scale bar is 5 μm. (b) Gate and (inset of b) drain-source bias electrical transport behavior of the device. Scanning photocurent imaging of the device with the electrodes outlined in gray and the few-layer graphene outlined in purple. Scale bar is 5 μm. (d) Gate depdent scanning photocurrent image taken with x fixed, shown as the dashed line in (c), showing the change in polarity of the photocurrent response as the bands are modulated by the back gate voltage. Y-axis is postion and x-axis is back gate voltage with scale bars of 5 μm and

5V, respectively. 67
Figure 4.7 Electrical Transport in few-layer 1T-$TiSe_2$. (a) A schematic illustrating the layout of a $TiSe_2$ device. (b) Temperature-dependent resistance measurements show the characteristic resistivity peak (black). A broad maximum is noted at ~180K. A ratio for R_{max}/R_{300} of ~1.3 is observed, indicating the high quality of the mechanically exfoliated $TiSe_2$. The first derivative of the temperature-dependent resistance with respect to temperature is shown in red. The minimum of this curve, ~206 K, corresponds to the CDW phase transition temperature. The green background represents the CDW phase. Inset in (c) is an optical micrograph of a $TiSe_2$ device. The scale bar is 10 μm. 69
Figure 4.8 Raman Spectroscopy of few-layer 1T-$TiSe_2$. (a) Raman spectrum of a typical few-layer $TiSe_2$ flake at room temperature. Two strong peaks are seen at ~134 cm^{-1} and ~197 cm^{-1}, respectively, which match well with predicted E_g and A_{1g} optical phonon modes. A weak peak is observed at ~305 cm^{-1}, which may result from the overlap of the two phonon processes or as a remnant of the silicon substrate. (b) Illustration of the E_g and A_{1g} crystal lattice vibrations in $TiSe_2$. Reprinted with permission from Ref [156]. Copyright © 2018 John Wiley and Sons...... 70
Figure 4.9 SPCM of $TiSe_2$ Metal Junctions under 1064 nm illumination. (a) Spatially resolved photocurrent and (b) reflection images of the device at 145 K show strong photocurrent responses under 1064nm wavelength excitation of ~1.86 mW at $TiSe_2$-metal junctions. The power of the 1064 nm laser is ~1.86 mW. The inset of (a) shows a circuit diagram of the $TiSe_2$ device depicting the current direction for the respective laser scanning locations. The laser scan across the drain (source) contact, resulting in the observed negative (positive) photocurrent signals. Photocurrent responses across the $TiSe_2$-metal junctions at (c) 145 K and (d) 280 K, respectively. The black dots and red solid curves are experimental data and the related Gaussian fittings, respectively. The photocurrent "tail" on the electrode is highlighted by the blue arrow. The yellow backgrounds represent the positions of the electrodes.. 72
Figure 4.10 SPCM of $TiSe_2$ Metal Junctions under 650 nm illumination. (a) Spatially resolved photocurrent and (b) reflection images of the device at 145 K show strong photocurrent responses at $TiSe_2$-metal junctions. The power of the 650 nm laser is ~0.14 mW. The inset of (a) shows a circuit diagram of the $TiSe_2$ device depicting the current direction for the respective laser scanning locations. The laser scan across the drain (source) contact, resulting in the observed negative (positive) photocurrent signals. Photocurrent responses across the $TiSe_2$-metal junctions at (c) 145 K and (d) 280 K, respectively. The black dots and red solid curves are experimental data and the related Gaussian fittings, respectively. The photocurrent "tail" on the electrode is highlighted by the blue arrow. The yellow backgrounds represent the positions of the electrodes. 73
Figure 4.11 Power Dependence of $TiSe_2$-Metal Junctions (a) Power dependent measurements for 650nm (red triangles) and 1064nm (black squares) laser illumination. (b) High power 1064nm laser illumination. 74
Figure 4.12 Improved Photoresponse Dynamics in the CDW phase of 1T-$TiSe_2$ (a) Representative sample of the temporal photocurrent response under 1064nm illumination and below the T_{CDW} at 145K. Snapshots of the rising (b) and decaying (c) portions of the temporal photocurrent response below the T_{CDW} at 145K (in black circles) and above the T_{CDW} at 225k (in blue squares). 75
Figure 4.13 Improved responsivity and response time in the CDW phase of 1T-$TiSe_2$. (a) Temperature dependent response time constants showing the step-wise increase in response time above the T_{CDW}. Rise and decay time constants are indicated by black and red triangles,

respectively. (b) Temperature dependent responsivity measurements under 650nm (red triangles) and 1064nm illumination showing the doubling of the rate of change in responsivity with respect to temperature below the T_{CDW}. The green background in (a) and (b) indicates the CDW phase. 76
Figure 5.1 Characteristic Intracellular Action Potential. The voltage characteristic resulting ion movement due to a stimulus inducing the opening and closing of sodium and K^+ channels. Reproduced from Ref. [203] under (CC BY 4.0). 78
Figure 5.2 Comparsion of Common Electrophysiological Techniques. (a) A reconstructed image of a nanopipette patch-clamping scheme. (b) Summary of a voltage sensitive dye experiment showing the modulation in fluorescence nitensity with time to elucidate the action potential. (c) An optical image of an implantable MEA with a penny shown for scale. Images were reprinted from Ref [204] for (a) under (CC BY 3.0), [205] for (b) under (CC BY 3.0), [206] for (c) © 2007 Society for Neuroscience. 80
Figure 5.3 Structure of the Retina. The retinal structure showing the layers that light must travel through to stimulate the retina as well as propagate back through to produce action potentials at the RGC layer. 82
Figure 5.4 Structure of RGCs. Dendrites branch out from the cell body. An axon runs from individual RGCs and are bundled together at the back of the eye to form the optical nerve head. Reproduced with permission from Ref [219]. Copyright © 1992 Cambridge University Press. . 83
Figure 5.5 Simplified Diagram of Electrophysiology Setup. (a) Schematic of pMEA setup with heated cannula, overflow cannula, and suction channel shown in red, purple, and blue, respectively. (b) Custom designed MEA holder with the large reference electrode visible on the left. (c) Transmission imaging of a retina (with the filter paper support) placed on top of the MEA. Each dark area corresponds to a sensing electrode. 85
Figure 5.6 Standard K^+ Retina Experiment. (a) A median waveform extracted from all the spikes (shown in the inset, y-scale bar 50 µV and x-scale bar 500 µs) a trial of an experiment. (b) Histogram and raster (rug) plot of action potential firing rate as a function of time. (c) Box-and-whisker plot indicating the significance of the K^+ stimulation. 86
Figure 5.7 Observed Biphasic and Triphasic Extracellular Action Potentionals. (a) – (c) show characteristic biphasic action potentials of varying waveforms. (e) – (f) show characteristic triphasic action potentials of varying waveforms. 88
Figure 5.8 Volume Conductor Theory of Biphasic and Triphasic Extracellular Spikes. (a) and (b) show the conceptual frame for the polarity and biphasic nature of a spike at a soma according to volume conductor theory. In (a), the firing of an action potential results in a depolarization (negative) potential relative to a distant reference electrode that then results in (b) positive potential as the cell repolarizes. (c) – (e) show the conceptual frame for the polarity and triphasic nature of a spike along an axon according to volume conductor theory. As an action potential fires, the sensing region near the electrode becomes a potential source for a nearby depolarized membrane (c), as the action potential propagates the contact region becomes depolarized (d), and finally as the action potential continues the contact region becomes repolarized (e). Reprinted with permission from Ref [224]. Copyright © 2014 Thieme. 89
Figure 5.9 Observed ON and OFF Transiet RGC Response. (a) ON and (b) OFF transient light responses. Light stimulation (one second pulse) is indicated by red lines. 90
Figure 5.10 Variable Length Light Responses Showing Sustained ON and OFF RGCs. Sustained ON RGC light responses of 3 (a), 5 (b) and 10 (c) seconds. Sustained OFF RGC light responses of 3 (d), 5 (e) and 10 (f) seconds. Red background indicates the period of light stimulation.. 91

Figure 5.11 Photocurrent Integrity in Pressurizable Graphene Microfluidic Culture Chamber. Optical images two electrodes in a channel area that is covered with graphene (a) before and (b) after being pressurized. Corresponding photocurrent imaging is shown in (c) and (d). All scale bars are 20 µm. 93
Figure 5.12 DIC and Fluoresce Images of Neuroblastoma. (a) DIC and (b) corresponding green CTB fluorescence images of neuroblastoma cells on graphene coverslip devices. All scale bars are 20 µm. 94
Figure 5.13 Green CTB Retinal imaging. Axons radiating from the optical nerve head (opaque portion near the bottom of the image) can clearly be observed. Scale bar is 50 µm. 95
Figure 6.1 Example of Basic Edge Detection. (a) Optical imaging of $TiSe_2$ flakes on a Si/SiO_2 substrate. (b) An overlay of basic edge detection using the sobel method via the Image Process Toolbox available in Matlab. 98
Figure 6.2 First Transistor Fabricated at Bell Laboratories. The point contact transistor consisting of a plastic wedge holding gold foil in contact with germanium. The emitter and collector leads are connected to the gold foil on each side of the wedge. The base lead is connected to the germanium. Reproduced from Unitronic under Creative Commons Attribution-Share Alike 3.0 Unported license (CC BY-SA 3.0). 99
Figure A.0.1 Laser Optical Path for TMDC Scanning Photocurrent Microscopy Setup. .. 100
Figure A.0.2 Retina Electrophysiology Setup. 105

LIST OF PUBLICATIONS

Portions of this dissertation have been adapted and/or reprinted from the following publications:

Thayer S. Walmsley, Bhim Chamlagain, Upendra Rijal, Tianjiao Wang, Zhixian Zhou, and Ya-Qiong Xu, "Gate-tunable Photoresponse Time in Black Phosphorus-MoS_2 Heterojunctions," *Advanced Optical Materials* 7, 1800832 (2019).

Thayer S. Walmsley, Kraig Andrews, Tianjiao Wang, Amanda Haglund, Upendra Rijal, Arthur Bowman, David Mandrus, Zhixian Zhou, and Ya-Qiong Xu, "Near-infrared Optical Transitions in $PdSe_2$ Phototransistors," *Nanoscale* 11, 14410 (2019).

Christian D. Ornelas, Arthur Bowman, **Thayer S. Walmsley**, Tianjiao Wang, Kraig Andrews, Zhixian Zhou, and Ya-Qiong Xu, "Ultrafast Photocurrent Response and High Detectivity in Two-dimensional $MoSe_2$-based Heterojunctions," *ACS Applied Materials & Interfaces* 12, 46476 (2020).

Xiaosi Zhang, **Thayer S. Walmsley**, and Ya-Qiong Xu, "In situ Monitoring of Electrical and Optoelectronic Properties of Suspended Graphene Ribbons during Laser-induced Morphological Changes," *Nanoscale Advances* 2, 4034 (2020).

Thayer S. Walmsley and Ya-Qiong Xu, "Enhanced Photocurrent Response Speed in Charge-Density-Wave Phase of $TiSe_2$-Metal Junctions," *Nanoscale* (2021).

Chapter 1 Introduction to 2D Transition Metal Dichalcogenides and Scanning Photocurrent Microscopy

1.1 Introduction to 2D Materials and Transition Metal Dichalcogenides (TMDCs)

The successful isolation and characterization of graphene (a two-dimensional hexagonal arrangement of carbon atoms) opened up a new dimension to materials science, prompting the exploration and exploitation of its unique mechanical, electrical, and optical properties. It has been found that it is nearly 300 times stronger than steel yet as flexible as rubber, permits 200 times faster charge transport than silicon, and is nearly transparent (more so than glass).[1, 2] This has led graphene based devices to touch nearly every scientific discipline from biology in the form of flexible sensors, to chemistry in the form of catalysts, to physics in the form of transistors as well as many disciplines in between. Despite the diverse applications enabled by its special properties, the lack of a sizeable band gap has limited its ability to be used in some electronic and optoelectronic devices.[3, 4] The desire to overcome this limitation accompanied by the realization that atomic layers of materials are stable, a phenomena thought to be previously ruled out due to thermodynamic instability[5], has resulted in an explosion of research into 2D materials. But before continuing to a discussion of these other materials, it is worth considering what is meant by the dimensionality of materials.

Living in a three dimensional (3D) world an impulse exists to describe the dimensionality of materials through length, width, and height. And while this is precisely true for 3D materials such as graphite, the 3D assembly of many layers of graphene, as shown in Figure 1.1a. This description is usually not satisfactory as one steps down into lower dimensions, since atoms can be considered to have their own length, width, and height, meaning a truly lower dimensional space is not actually obtained. To remedy this, two approaches are offered and used in

understanding 2D materials in this work as well as lower dimensional materials in general. One is that the relative magnitude of the dimension that is "removed" is much smaller than the remaining ones. For example the length and width (~ microns) of a graphene sheet, as shown in Figure 1.1b, are much greater than its relative height (sub-nanometer). This is similar for one dimensional (1D) materials, such as carbon nanotubes shown in Figure 1.1c. Though this is useful in classifying and understanding 1D and 2D materials, the lack of a relative dimension breaks down in zero dimensional materials (0D) such as a fullerenes, spheres of carbon, shown in Figure 1.1d.

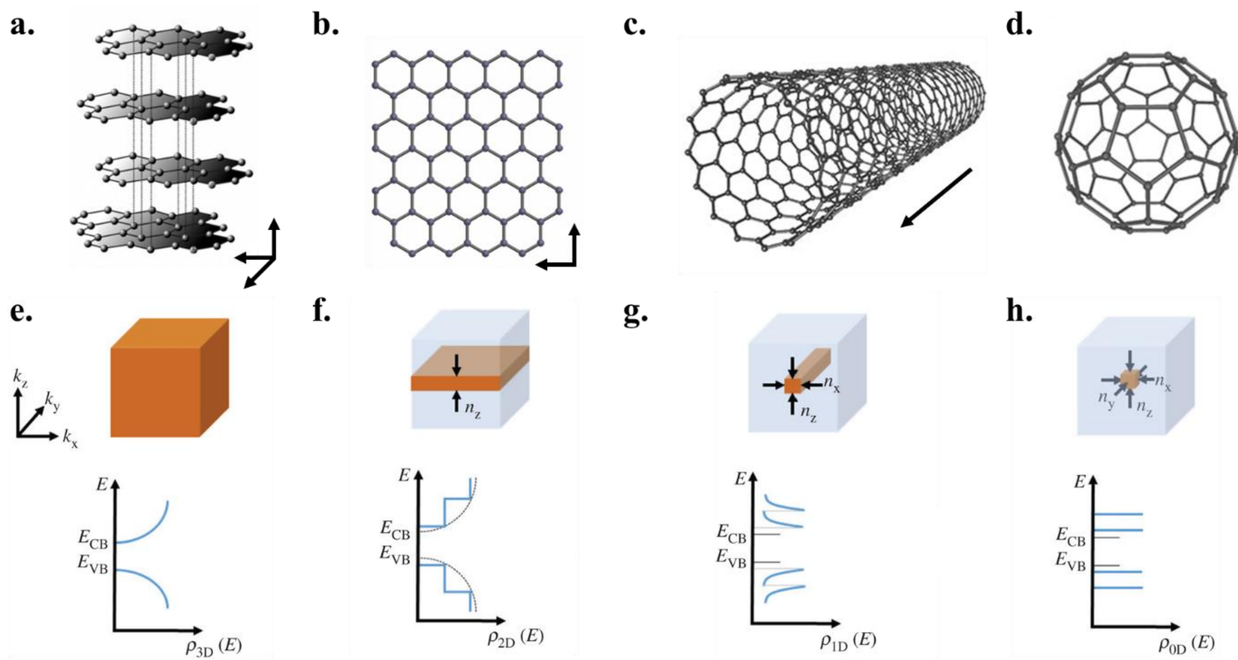

Figure 1.1 Material Dimensionality. The 3D, 2D, 1D, and 0D allotropes of carbon are shown as graphite, graphene, a carbon nanotube, and a fullerene in (a), (b), (c), and (d), respectively. The added black arrows signify the number and direction of dimensions General forms of the density of states for 3D, 2D, 1D, and 0D states are shown in (e), (f), (g), and (h). The blue shows the representative dimension with the higher dimension traced in gray. (a) and (b), are reproduced under (CC0 1.0) and (CC BY 2.5), from Mattman723 and Zhantongz, respectively. (c) and (d) are reproduced under (CC BY 3.0) from Mstroeck. (e) – (h) are reproduced from Ref. [6] under (CC BY 4.0).

Another approach is to consider properties such as the density of states. The distribution of electrical states play a pivotal role in the formation of band gaps and electrical transport as the

effective dimension in which charges can exist or move in is reduced with decreasing dimension.[6] This is diagrammed for 3D, 2D, 1D, and 0D carbon allotropes in Figure 1.1e – 1.1h, respectively. This quantum confinement is likely the reason for the unique properties in 2D materials as well the observation of thickness dependent qualities.[7] 1D and 0D materials also have shown some extremely interesting properties, which include superdiffusive phonon transport in aligned 1D atomic chains of $NbSe_3$, which offer a new route to thermal superconductors.[8] Ironically, heavy metal based *size-dependent* 0D quantum dots are excellent light emitters.[9]

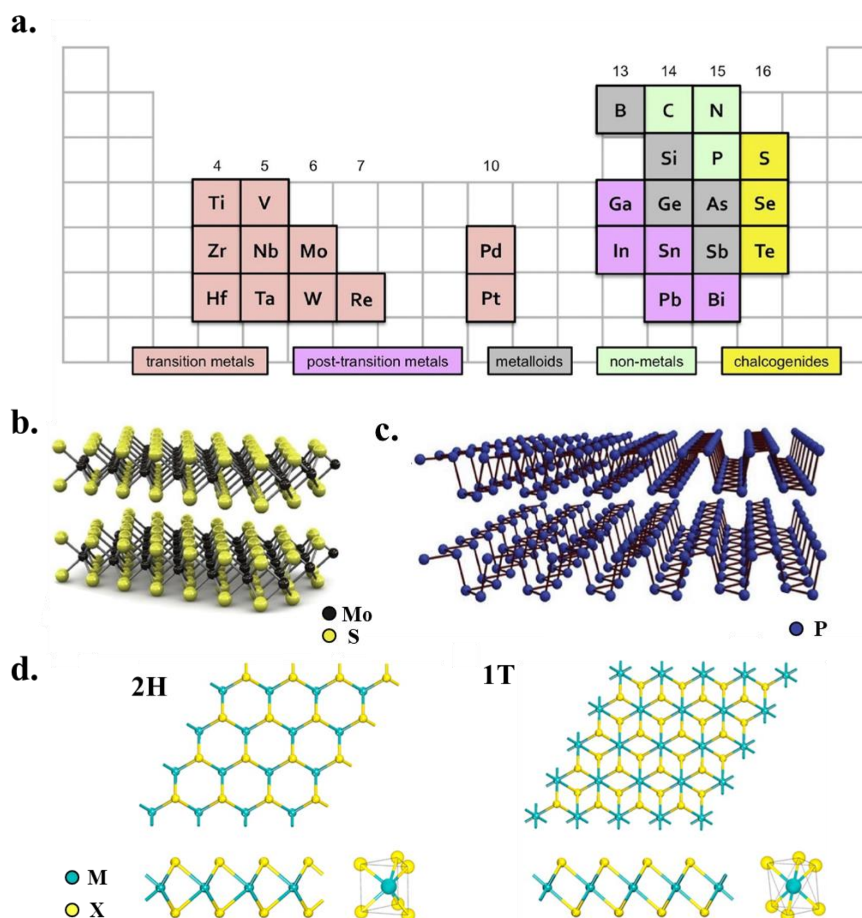

Figure 1.2 2D Transition Metal Dichalcogenides. (a) Periodic table highlighting some significant elements for 2D materials. (b) and (c) ball and stick models representing the popular TMDC MoS_2 and graphene analog for phosphorus, respectively. (d) Diagram of the characteristic X – M – X structure as well as the common 1T and 2H phases for TMDCs. (a) – (c) Reproduced with from Ref [10] under (CC BY 4.0). (d) Reproduced with permission from Ref. [11]. Copyright © 2015 American Chemical Society. This is an unofficial adaptation of an article that appeared in an ACS publication. ACS has not endorsed the content of this adaptation or the context of its use.

Returning to 2D materials, one finds that beyond graphene, and other single element materials like the phosphorous analog phosphorene (Figure 1.2c), a group of materials known as transition metal dichaclogenides (TMDCs) have attracted significant attention. These materials are characterized by the X−M−X structure, where the X represents a chalcogen atom from group sixteen (primarily S, Se, and Te), and the M is a transition metal from groups four though seven or ten, as shown in Figure 1.2a and 1.2b. This is also shown in Figure 1.2d, along with a comparison of two common phases. The 2H phase is the alignment in orientation between the different X atoms layers while the 1T phase presents a 60º relative rotation of these layers. Though many TMDs are well understood in their bulk form, relatively few have received significant attention in their few-layer or monolayer form. Of these materials, MoS_2 is the most widely studied with a thickness dependent band ranging from a direct band gap of ~ 1.9 eV in its monolayer form and to an indirect gap of ~1.3eV in bulk.[12-14] It has also shown strong electronic performance with a field-effect mobility of ~700 $cm^2V^{-1}s^{-1}$ and ON/OFF ratios upwards of 10^8 [15, 16] as well as strong optoelectronic properties in ultra-high photo responsivities (~880 AW^{-1}).[17, 18] Interestingly, a prolific use of both bulk graphene (graphite) and bulk MoS_2 is as a mechanical lubricant. And the primary property that make these solids slippery are enabled by the same weak interlayer van-Der Waals forces that allow facile mechanical exfoliation and isolation of individual atomic layers. Beyond the semiconducting MoS_2, other 2D TMDCs have also revealed more semiconductors ($MoSe_2$, WS_2, etc.) as well as semimetals (WTe_2, $TiSe_2$ etc.) and metals (VSe_2, etc.).[19-21] To offer perspective on the study of 2D materials a graphical summary of publications is shown in Figure 1.3. This keenly illustrates the relative impact of graphene in total publications (Figure 1.3a) as well as in optoelectronic devices (Figure 1.3b). Furthermore the dominance of MoS_2 is seen in Figure 1.3c.

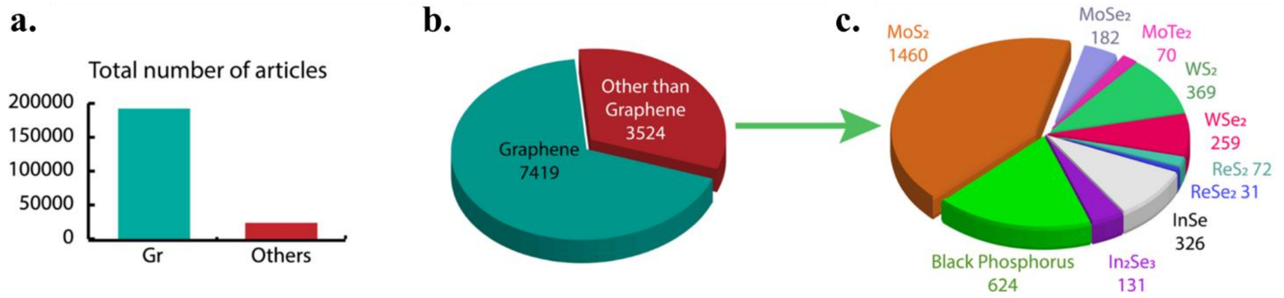

Figure 1.3 Publication Perspectives on 2D Materials. (a) Total number of published article on 2D materials. (b) Total number of published articles on optoelectronics and photonics. (c) Portion of articles for specified 2D materials other than graphene from (b). Data collected from the Web of Science as of April 2019. Reproduced from Ref. [22] under (CC BY 3.0).

Though TMDCs dominate the literature on optoelectronic devices there are a bevy of other 2D materials such as Transiton Metal Carbides (Ti_3C_2, Cr_2C etc.), Transition Metal Oxides (Fe_2O_3, MnO_3, etc.), 2D Perovskites ($SrTiO_3$ etc.) as well as others that have merited optoelectronic investigation due to their varied and thickness dependent band gaps as shown in Figure 1.4.

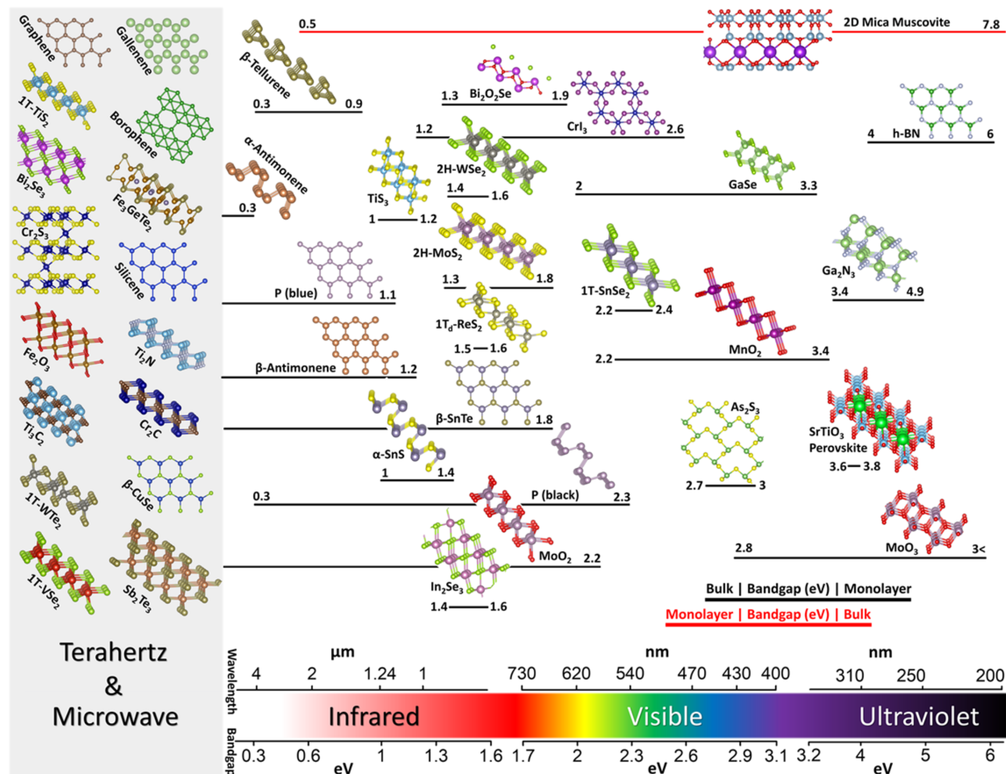

Figure 1.4 Varied Band Gaps in 2D Materials. Reproduced from Ref [7], under (CC BY 4.0).

1.2 Near Infrared Photodetection

Photodetectors plays such a pivotal role in scientific discovery that the Nobel Prize in Physics has recognized them outright four times, two of which in photography and two of which for the photoelectric effect, and implicitly numerous other times such as in their use detecting neutrino oscillations in the 2015 Nobel Prize. Clearly these photodetectors manifest themselves in markedly different forms, but the necessity of a material to sense incident light is central to all of them. For a single material to sense the nearly infinite continuum of electromagnetic radiation that is light is a tall and unreasonable task, so the electromagnetic spectrum is divided up into different portions with certain materials possessing sensitivities accordingly. This emphasizes the central role that materials play in finding effective photodetectors for target wavelength ranges. A general picture of the electromagnetic spectrum with illustrative examples is shown in Figure 1.5.

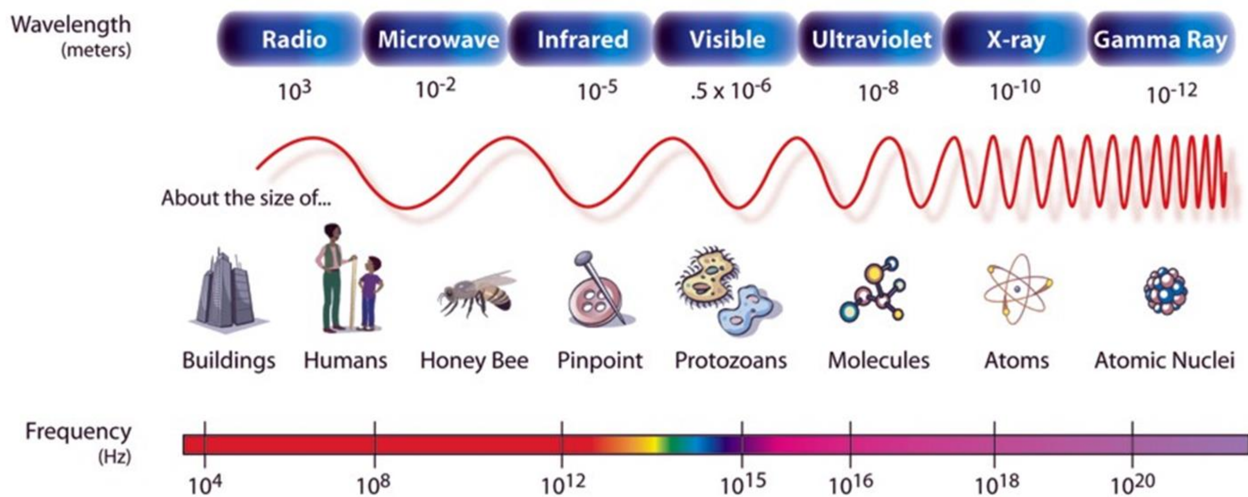

Figure 1.5 The Electromagnetic Spectrum. Public domain image reproduced from NASA JPL.

This work focuses on a portion of this spectrum, the part just outside the visible: the near infrared (NIR). The exact delineation for the wavelength range for the NIR is variable, but for the purposes of this work and its eye toward retina electrophysiology the range is considered to be 650nm to 1350nm as this is the range which light has its maximum penetration depth in tissue.[23]

The first biological window is the primary focus of this work as it offers the aforementioned advantages and a lower wavelength offers the potential for higher resolution. And though the results in this work primarily report on the shorter side of this range (containing the entirety of the first biological window and 100 nm into the second), significant insights are still gleaned for full NIR photodetection. A delineation of this window and its importance is shown in Figure 1.6a. In addition to biological investigations, NIR photodetectors are pivotal to many military technologies, portions of the telecommunications band, some astronomical investigations, and assessing the quality of food or petrochemical products.

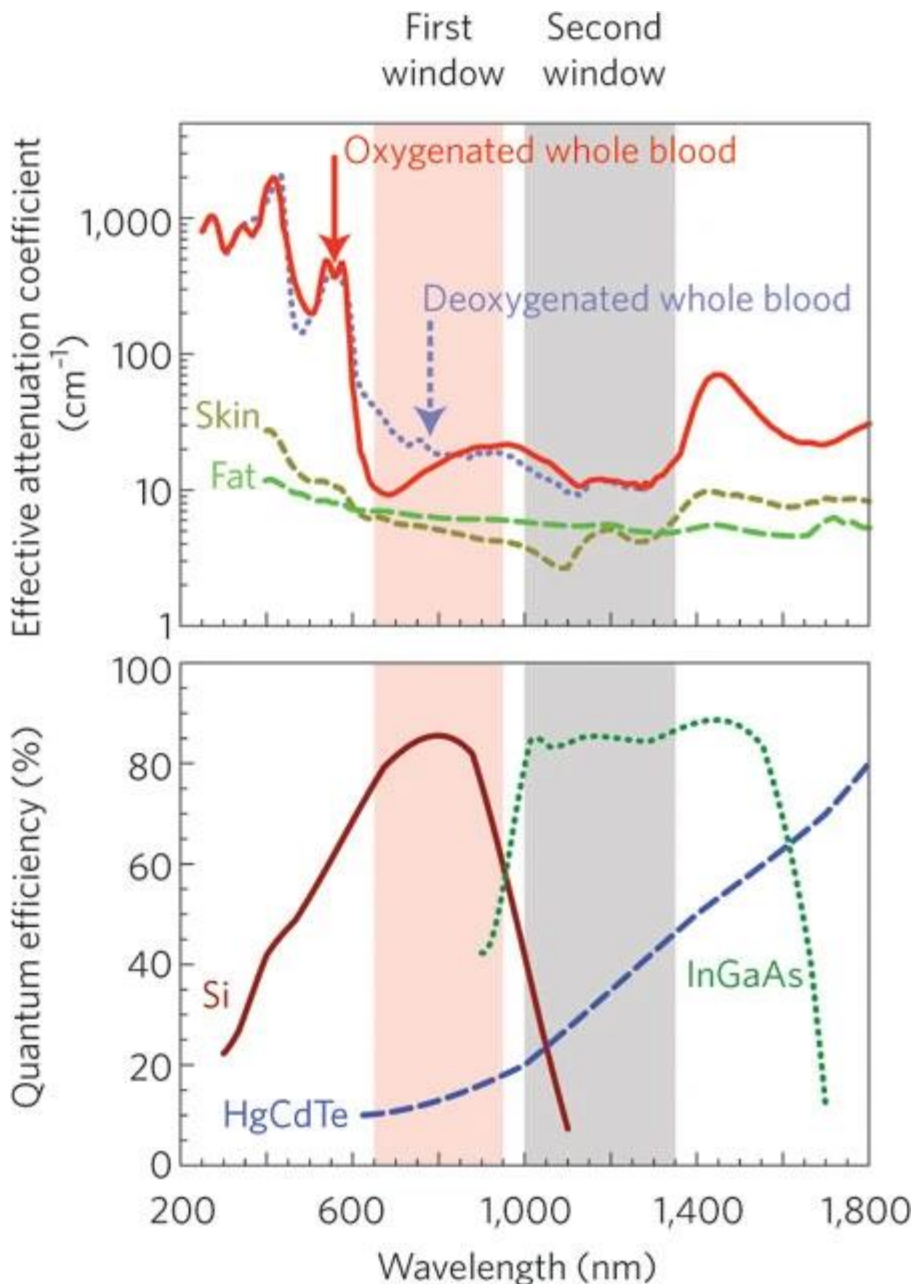

Figure 1.6 NIR Biological Windows. (a) Penetration depth in the first (in red) and second (in gray) biological windows with respective to certain aspects of biological tissue. (b) Comparison of standard NIR photodetectors with respect to the two NIR biological windows. Reprinted with permission from Ref [23]. Copyright © 2009 Macmillan Publishers Limited.

Though commercial NIR photodetectors exist, they suffer from some severe limitations. Germanium based photodetectors are unable to simultaneously show high speed and high responsivity due to thickness tradeoffs of the absorption layer.[24] Silicon based photodetectors rapidly lose sensitivity after ~ 1000nm limiting their use in the full NIR range. And other NIR

photodetectors based on inorganic semiconductors, like InGaAs or HgCdTe, suffer from intensive and expensive fabrication processes in the form of molecular beam epitaxy and/or require low operating temperatures.[25] The relative weakness of these photodetectors is shown in Figure 1.6b. Additionally, these bulk materials are unable to offer other properties like the flexibility and optical transparency that 2D materials can possess.

1.3 Scanning Photocurrent Microscopy (SPCM)

Many different experimental techniques with different aims are used to investigate the electronic and optoelectronic properties of 2D materials. Some of these include angle resolved photoemission spectroscopy that can provide a detailed look at band structures and pump-probe spectroscopy that can explore dynamical processes. Given the central role that scanning photocurrent microscopy plays in this work and its ability to investigate 2D materials as device candidates for NIR detection as well as in the exploration of fundamental physical properties a brief overview of this experimental technique and the setup is provided.

Scanning Photocurrent Microscopy (SPCM) is a powerful experimental technique that employs rasterized laser excitations to generate a spatial mapping of current values. The resulting mapping can shed light on the photocurrent generation mechanisms present as well as other properties such as internal electric field, charge transport, and recombination dynamics. Furthermore, the technique facilitates the facile addition of other experimental equipment that enables spatially resolved wavelength-, temporal-, temperature-, gate-, and bias-dependent measurements.

The origins of SPCM are found within the scanning probe microscopy. Similar to scanning tunneling microscopy, atomic force microscopy (AFM), and electrostatic force microscopy a local excitation source is used but instead of a probe tip a focused laser beam is used. This beam locally

excites charge carriers in a device which subsequently relax through thermal, recombination, diffusion, and drift processes. Provided that the charge carriers reach these electrodes before they recombine a current signal is measured. The current signal that is a result of these excitations is termed the photocurrent, I_{PC}. To exclude the current that may be flowing in the device as result of other factors such as external biases it is defined as the difference between the total current (with illumination), I_{total}, and the dark current (without illumination), I_{dark}, as shown in equation (1). This photocurrent is sometimes referred to as the short circuit current. Additionally, a drain-source bias can be applied to lower the potential barrier and thus counteract this current which results in a voltage value known as the open circuit voltage.

$$I_{PC} = I_{total} - I_{dark} \qquad (1)$$

1.3.1 Experimental Setup

A schematic of the critical elements related to the electrical and optoelectronic characterization are presented in Figure 1.7. The supercontinuum laser (NKT Photonics, SuperK Select model) provides a tunable wavelength in the range of 650 nm to 1100 nm. The scan mirror (Nutfield Technology, RS 15) uses piezoelectric motors to control a pair of mirrors to guide the laser with nanometer scale precision. Photocurrent signals are located via simultaneous imaging taken with a Si photodetector (Thorlab, PDA 36A). The optical chopper (Scitec, model 300CD) enables light ON/OFF modulation to perform temporally resolved scanning photocurrent measurements. Though the rise/decay time of the optical chopper is ~300ns, the minimum timing resolution of the system is limited by the current preamplifier (DL instruments, model 1211) at ~8 µs.[21, 26] The laser is focused in to a diffraction limited laser spot (< ~1 μm^2) by an Olympus LUCPlanFLN 40x objective (N.A. = 0.6). The sample is mounted on a chip carrier (Spectrum Semiconductor Materials) and held in a Janis ST-500 microscopy cryostat. The cryostat can be liquid nitrogen cooled. A multifunctional data acquisition unit (National Instruments, USB 6363

model) provides drain-source bias, enables data collection, and controls the scan mirrors. A back gate voltage is provided via a Keithley Model 6487 Picoammeter/Voltage Source. Further details regarding the optical path of the laser are provided in appendix A.1.

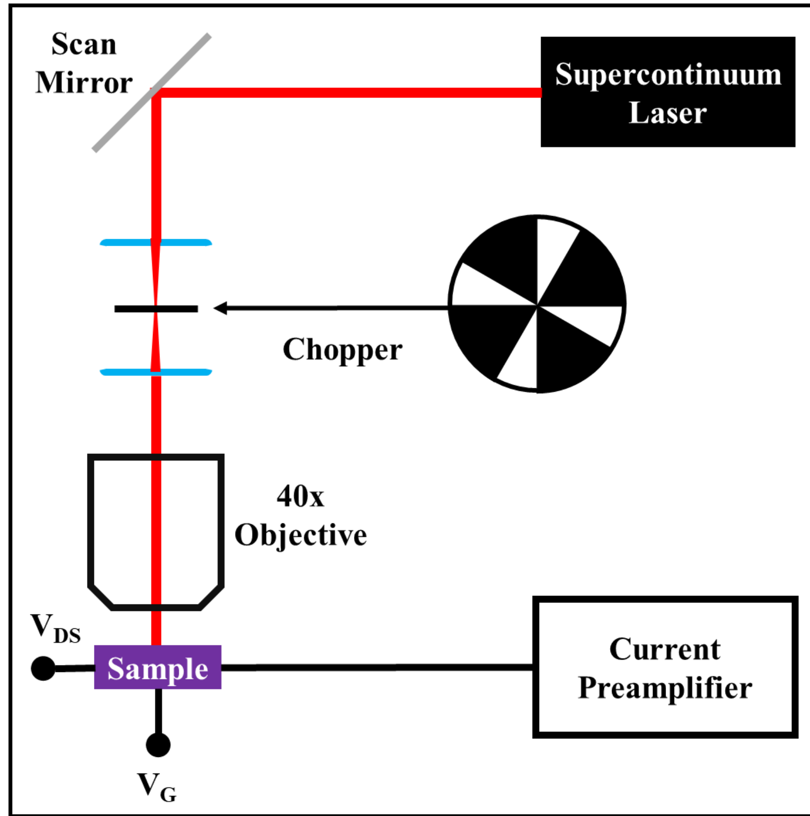

Figure 1.7 Scanning Photocurrent Setup. Schematic presenting the crucial elements that enable the electrical and optoelectronic characterization of the 2D TMDC devices discussed in this work.

1.4 Photocurrent Generation Mechanisms

A critical element for engineering optoelectronic devices is an understanding of the underlying photocurrent generation mechanisms. This requirement is further compounded when looking at the novel physics often present in 2D materials. There are several mechanisms that can contribute to photocurrent generation. The three that play the most prominent role in this work are

the photovoltaic (PVE), photo-thermoelectric (PTE), and photo-bolometric effects (PBE).

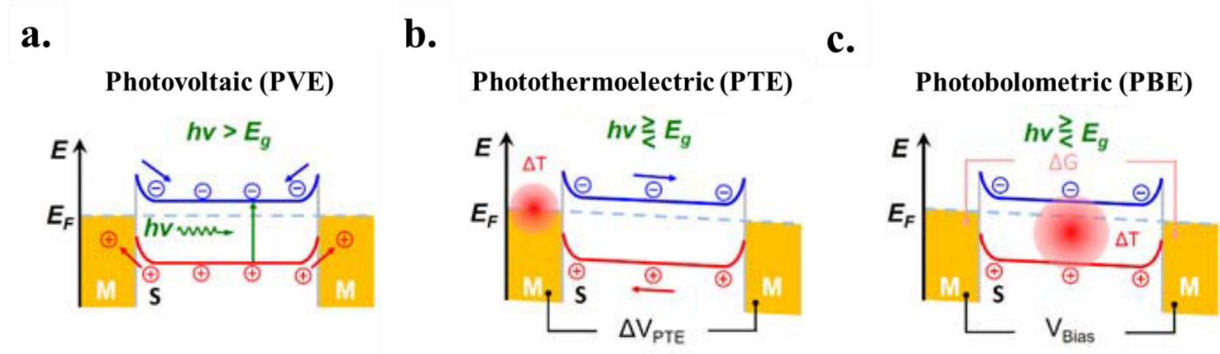

Figure 1.8 Relevant Photocurrent Generation Mechanisms. Schematic representation of photocurrent-generation mechanisms in semiconducting 2D materials. M and S indicate metal electrode contacts and 2D semiconductor channels, respectively. (a) Photon-excited electron-hole pairs (EHPs) separated by internal electric fields at metal-semiconductor Schottky barriers. Red shaded areas indicate an elevated temperature ΔT induced by laser heating, leading to (b) a voltage difference ΔV_{PTE} or (c) overall conductance change ΔG across the channel. Image and caption adapted and reprinted under (CC BY 4.0) from Ref [27].

The PVE is the result of photo-excited electron-hole pairs being separated by internal electric fields present in the device. This typically occurs in PN junctions or from Schottky barriers that arise at metal-semiconductor junctions. A schematic of this for a metal-semiconductor junction is shown in Figure 1.8a. The prominence of this photocurrent generation mechanism can be investigated through gate- and bias- dependent photocurrent measurements. Since the application of a gate voltage can change the band alignment potentially altering the direction and magnitude of the internal electric field, changes in polarity and intensity typically reveal PVE-induced photocurrent. Furthermore, the application of a bias is important as it can modulate the lateral band alignment often significantly enhancing the photocurrent response.

The PTE is the result of a light induced heat gradient between the semiconductor and metal contacts, as shown in Figure 1.8b. The resulting temperature difference, ΔT, induces a voltage difference, ΔV_{PTE}, due to the modified energy levels. This voltage scales linearly with the difference in Seebeck coefficients, S, of the materials. Though this change is characterized by the

difference of the metal and semiconductor, it primarily depends on the semiconductor since the Seebeck coefficient of metals is on the order of 1μVK^{-1}. This relationship is shown by equation (2). Given the difficulty in expressing the Seebeck coefficient in terms of known quantities, it is typically expressed for semiconductors through the Mott relation as shown by equation (3), where k_b is the boltzman constant, e is the charge of the electron, T is temperature, G is the conductance of the semiconductor, V_G is the back gate voltage, and E_F is the Fermi energy.[28] Due to the prominence of this effect at metal-semiconductor junctions, its presence is often easily identifiable by a photocurrent "tail" within the metal region as the heat induced voltage differential results in a deviation from the Gaussian shape of a typical photocurrent response.[29] Furthermore, this effect can be seen both in global illumination of devices where there is distinct portions of a device or when a laser is incident locally on the metal semiconductor junction. [30]

$$\Delta V_{PTE} = (S_{Semiconductor} - S_{Metal})\,(\Delta T) \approx (S_{Semiconductor})\,(\Delta T) \quad (2)$$

$$S_{Semiconductor} = \left(\frac{\pi^2 k_b^2 T}{3e}\right)\left(\frac{dln(G)}{dV_G}\right)\left(\frac{dV_G}{dE}\bigg|_{E=E_F}\right) \quad (3)$$

The PBE is another heat induced effect but it is the result of a uniform heating that changes the conductance, ΔG, of the semiconductor channel, as diagrammed in Figure 1.8c. This change will be represented as a linear increase in photocurrent, I_{PBE}, with applied drain-source bias, V_{DS} as shown in equation (4). A notable difference between the PBE and PTE is that the presence of the PBE can only be induced under an application of external bias but the PTE can play a role in unbiased devices.

$$I_{PBE} = (\Delta G)(V_{DS}) \quad (4)$$

Examples of the presence of these effects as well as the impact on polarity and intensity of photocurrent responses is shown in Figure 1.9. The photocurrent response from a Si waveguide integrated with a black phosphorous (BP) (p-type) photodetector for the NIR regime, is shown in in Figure 1.9a. At negative gate voltages (p-type electrostatic doping) strong PVE dominant photocurrent signals are seen in comparison to weaker PBE dominant photocurrent signals at positive gate voltages (n-type electrostatic doping) that result in signals of the opposite polarity of the applied bias.[31] The photocurrent response from a double gated WSe_2 (n-type) phototransistor of non-uniform thickness is shown in Figure 1.9b and 1.9c. Laser illumination (640nm) above the band gap, shown in Figure 1.9b, result in strong photocurrent signals in the PN and NP regions due to the PVE but significant photocurrent signals in the PP region are also observed. These strong PP photocurrent signals are due to the PTE as confirmed by below band gap excitations (885 nm) shown in Figure 1.9c. Above the band gap EHPs are able to be excited and separated by the internal electric fields generated by opposite electrostatic doping but below the band gap these EHPs are absent and the non-uniform device thickness produces a heat gradient under illumination, creating a PTE potential difference which drives current. Suppressed NN photocurrent signals from above the band gap excitations are possibly due to asymmetric Schottky contacts for holes and electrons and nonlinear IV-characteristics. For below band gap excitations it is likely due to the lower Seebeck coefficient of n-doped WSe_2. [32]

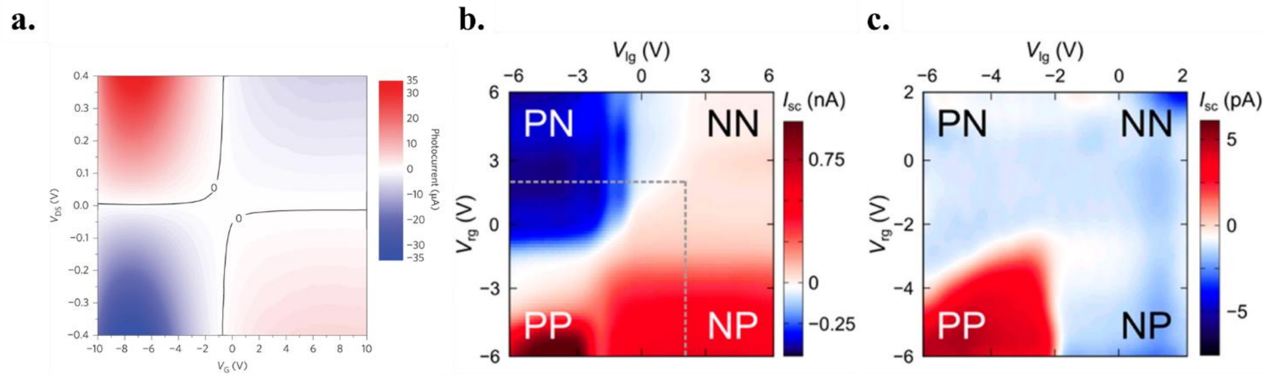

Figure 1.9 Examples of PVE, PTE and PBE Induced Photocurrent Signals. (a) Relative dominance of the PVE ($V_G < 0V$)and PBE ($V_G > 0V$) in a BP integrated Si waveguide. (b) and (c) show photocurrent signals in a non-uniform WSe_2 double gated phototransistor. (b) Above band gap illumination showing PVE dominance in PN and NP regions as well as the PTE in the PP region. (c) Below band gap illumination confrimng the PTE for the PP region. (a) is reproduced with permission from Ref [31]. Copyright © 2015 Macmillan Publishers Limited. (b) and (c) are reproduced with permission from Ref [32]. Copyright © 2014 American Chemical Society.

Chapter 2 NIR Light-Matter Interactions in 2D Phototransistors

2.1 Introduction to Metal-Semiconductor Junctions

Metal-semiconductor junctions are at the heart of every semiconductor device. They are among the oldest useful electronic devices and continue to play a pervasive role today. The distribution of electronic states which give rise to the band gap in semiconductors and the interactions of those with metals define the resulting properties of metal-semiconductor devices. These junctions possess a Schottky barrier of varying heights, depending on the relative value of the work function of the materials. To understand the different carrier contributions and polarity of photocurrent signals in 2D material devices it is often useful to create a band diagram. The materials are often examined first in isolation (Figure 2.1a) and then in contact (Figure 2.1b). For the metal in these diagrams, the metal's work function, Φ_M, must be known. For the semiconductor in these diagrams, it is typically easiest to know the work function, Φ_{SC}, and the electron affinity, χ_{sc}, of the semiconductor. The bending of the conduction and valence bands enable the Fermi levels to align and is governed by the Schottky-Mott Rule which predicts a potential barrier known as the Schottky barrier height, Φ_B. For N-type semiconductors it is defined by equation (5).[33, 34] This model provides a strong foundation for understanding 2D material junctions but it neglects the phenomena of Fermi level pinning, frequent in 2D TMDCs. This effect can render the Schottky barrier height less sensitive to the metal work function.[35] In either case the resulting Schottky barrier height can have a profound effect on the performance of electrical and optoelectronic devices.[36]

$$\phi_B = \phi_M - \chi_{SC} \quad (5)$$

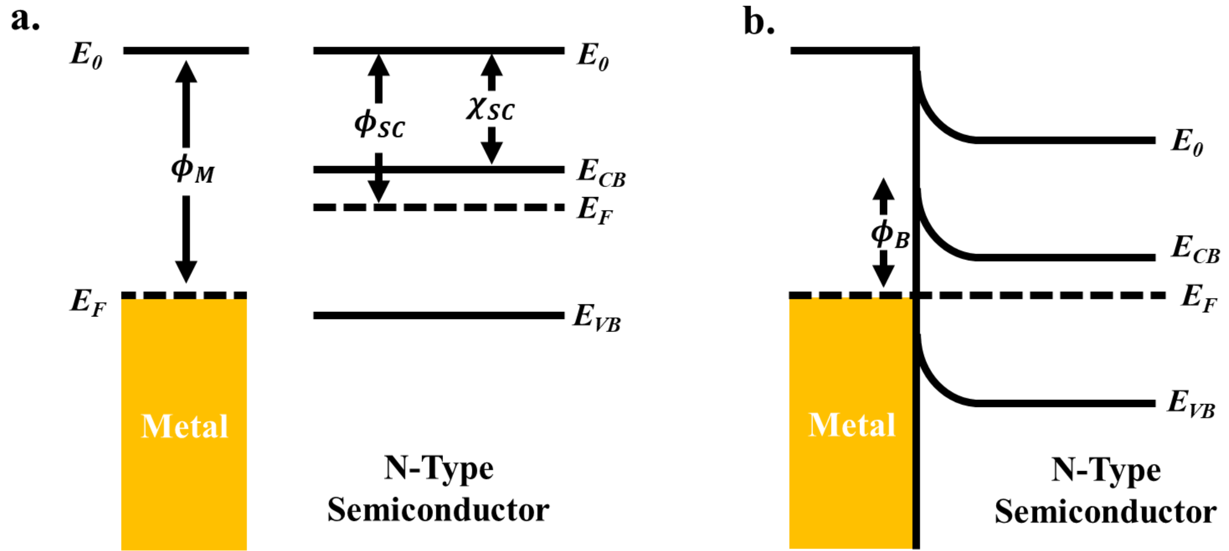

Figure 2.1 Metal-Semiconductor Junction Schematic (a) A metal and N-type semiconductor before coming into contact. (b) A metal-semiconductor with a Schottky barrier height governed by the Schottky-Mott rule.

In addition to being present in all semiconductor devices, metal-semiconductor junctions have been demonstrated as 2D material electronic and optoelectronic devices in their own right in the form of field-effect transistors (FET), highly rectifying diodes, photodiodes, and photodetectors.[37, 38]

2.2 $PdSe_2$ Phototransistors

The atomic composition and arrangement of 2D materials are the foundations for their intrinsic properties. In examining TMDCs, significant attention has been paid to group 6 materials (those where M in the characteristic X-M-X structure is Mo or W), which possess a similar hexagonal structure to graphene. But by looking beyond this group to the dozens of other TMDCs intriguing properties are found as result of atomic composition and arrangement. Such as among group 7 TMDCs, a high external quantum efficiency and a thickness-independent band gap of ReS_2 make it an attractive candidate for optoelectronics.[39] Additionally, a novel structure with mirror-symmetric single-crystal domains has been shown in this group by monolayer $ReSe_2$ and

is suggestive of novel anisotropic electronic and optoelectronic properties.[40]

More recently, the exploration of group 10 noble metal TMDCs has begun. Excellent near-infrared (NIR) photodetection capabilities have been demonstrated in $PtSe_2$ field-effect transistors (FETs).[41] Ultrahigh photogain has been achieved in back-gate modulated PtS_2 devices.[42] Of particular interest from this class of materials is $PdSe_2$. The high theoretically predicted mobility, upward of 42,000 $cm^2V^{-1}s^{-1}$, air stability of the electronic properties, and thickness-dependent band gap ranging from ~ 0 eV in bulk to an indirect band gap of ~1.43 eV in a monolayer structure make it an interesting material to further probe its optoelectronic properties.[43-45] Furthermore, the unique buckled pentagonal structure of $PdSe_2$ is highly intriguing. This is illustrated when considering pentagons tessellated in a 2D space. If one tries to completely fill this space, it quickly becomes clear that this is not possible. An example of this tessellation and the associated pentagonal structure of $PdSe_2$ that is enabled by puckering is shown in Figure 2.2a and 2.2b, respectively.

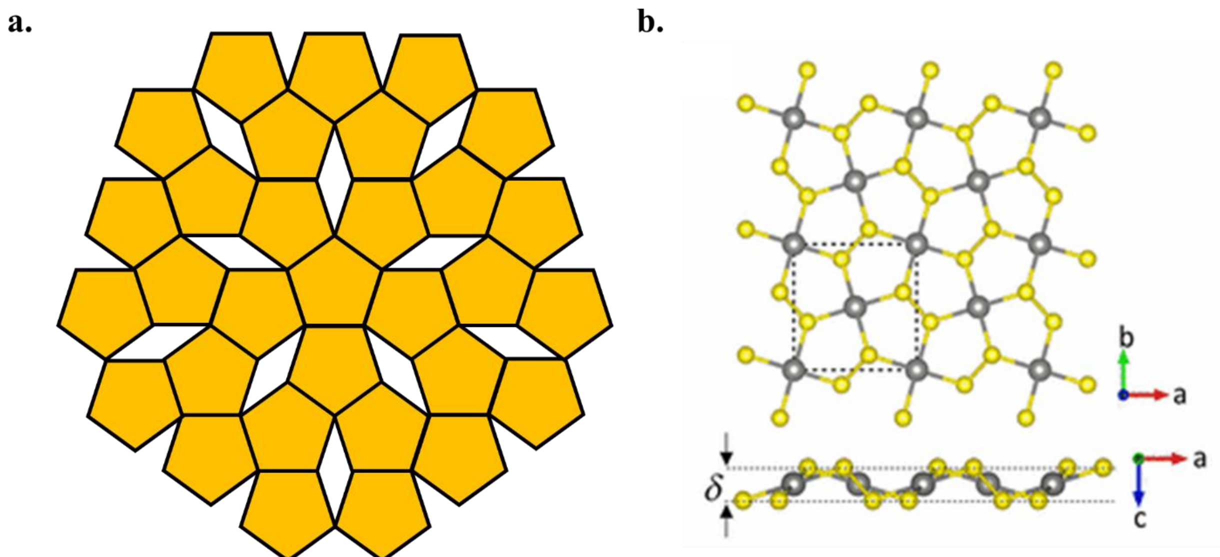

Figure 2.2 Puckered Pentagonal Structure of $PdSe_2$. (a) Regular pentagons tessellated in a plane. (b) Puckered pentagonal arrangement in $PdSe_2$. Pd and Se atoms are represented by gray and yellow balls, respectively. (b) reproduced with permission from Ref. [43]. Copyright © 2017 American Chemical Society.

With the dominance of the hexagonal arrangement of atoms in popular 2D materials such as MoS_2 and graphene or the buckled hexagonal arrangement of atoms in BP, the novel structure present in $PdSe_2$ offers many interesting opportunities for anisotropic electrical, optical, and optoelectronic devices.[43-49] A comparison of these puckered structures for BP and $PdSe_2$ is shown in Figure 2.3a and 2.3b, respectively.

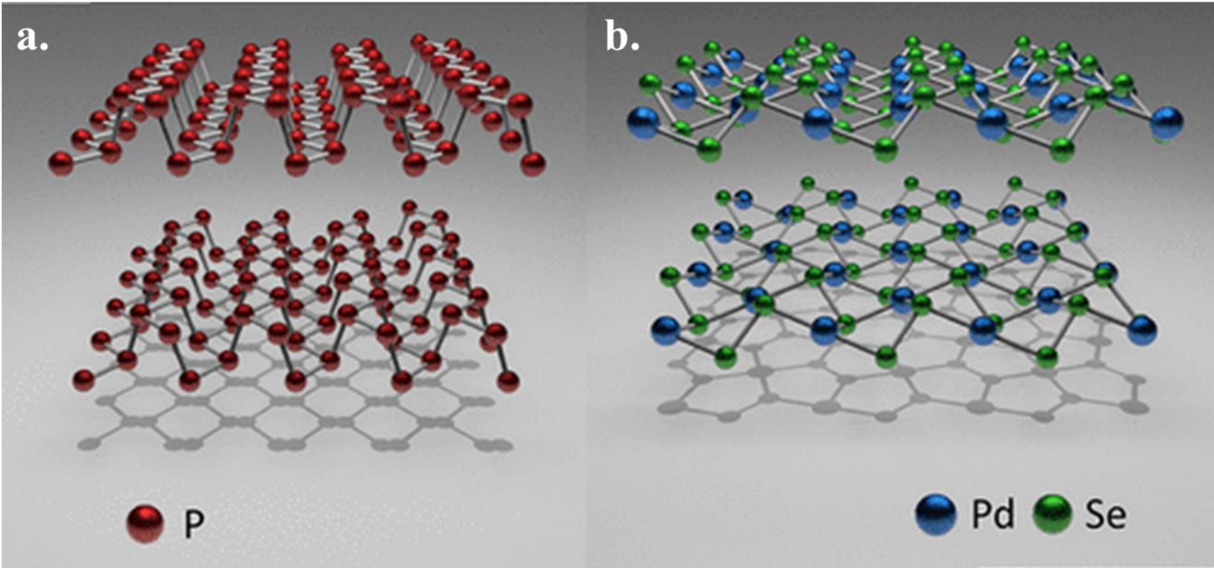

Figure 2.3 Comparison of Puckered strucutres in BP and $PdSe_2$. (a) Puckcered hexagonal structure of BP. (b) Puckered pentagonal structure of $PdSe_2$. (a) and (b) reproduced with permission from Ref. [43]. Copyright © 2017 American Chemical Society.

2.2.1 Results and Discussion

In this study, electrical transport and optoelectronic measurements are performed on few-layer $PdSe_2$ phototransistors via gate-, wavelength-, power-, and bias-dependent SPCM. The experimental results suggest that the strong photocurrent signals at metal-$PdSe_2$ junctions are mainly attributed to the PVE when $PdSe_2$ phototransistors turn off and partially related to the PTE when the devices are in the on-state. $PdSe_2$ devices are also demonstrated with a Seebeck coefficient as high as ~74 μV/K at room temperature, which is consistent with the theoretical predication.[44, 47] More importantly, thickness-dependent photoresponse resonance peaks are

observed in the NIR region. These likely results from indirect optical transitions in few-layer $PdSe_2$. Additionally, a fast response time is obtained (~156 μs), which is an improvement of more than two orders of magnitude over other group 10 noble TMDC based photodetectors. This work offers new insight into the optoelectronic properties of $PdSe_2$ and opens up new avenues for engineering future noble 2D TMDC based electronics and optoelectronics.

Devices to facilitate this study were provided by generous collaborators. The synthesis of high quality $PdSe_2$ crystals was performed by Dr. Amanda Haglund under the direction of Dr. David Mandrus and these crystals were exfoliated and fabricated into devices by Dr. Kraig Andrews, Dr. Upendra Rijal, and Dr. Arthur Bowman under the direction of Dr. Zhixian Zhou.

The high-quality few-layer $PdSe_2$ flakes were mechanically exfoliated from bulk crystals onto Si/SiO_2 substrates (degenerately-p-doped Si substrates with a 270 nm SiO_2 oxidation layer). Thin $PdSe_2$ flakes were then identified by using optical microscopy and characterized with a Park-Systems XE-70 non-contact AFM. Numerous devices and heights were examined ranging from 5 nm to 20 nm in height. To complete the device metal electrodes (10 nm Ti/45 nm Au) were deposited onto the flakes by using standard electron-beam lithography and deposition. The devices were then mounted in a chip carrier with carbon tape where contacts were wire bound and the gold backing of the chip carrier was also wire bound to facilitate a back gate voltage via the degenerately-doped Si substrate. A schematic of the device and an optical image of a typical device are shown in Figures 2.4a and 2.4b. The gold electrodes and few-layer $PdSe_2$ channel are outlined in gray and purple dashed lines, respectively.

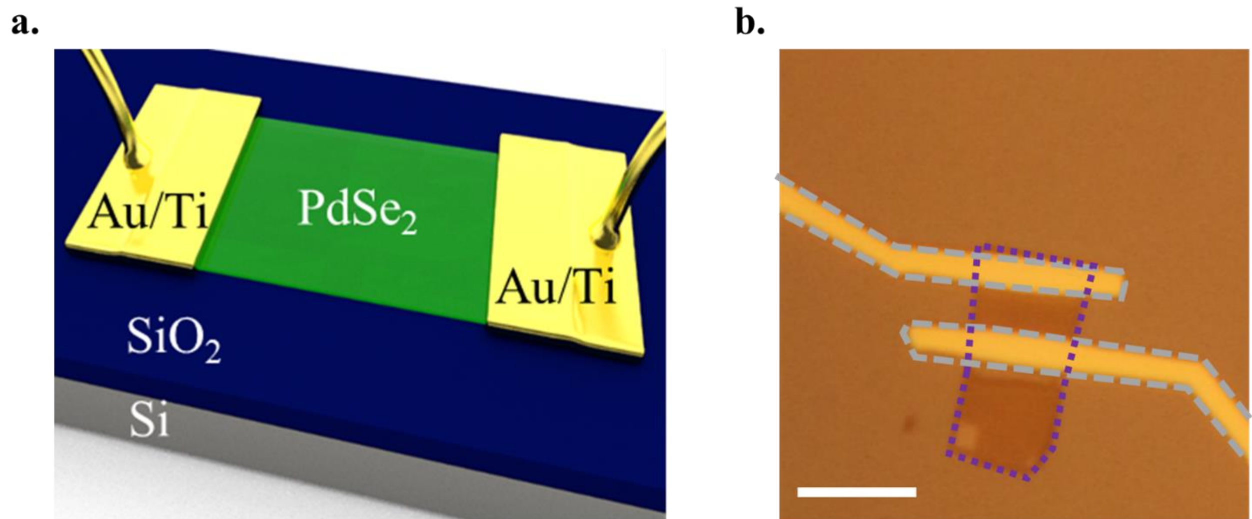

Figure 2.4 $PdSe_2$ Phototransistors. (a) A schematic of the $PdSe_2$ device. (b) An optical image of the as-fabricated $PdSe_2$ device. The $PdSe_2$ flake is outlined in a purple dashed lines and the electrodes are outlined in gray dashed lines. The scale bar is 5 μm.

The electrical properties of the devices were measured in a Janis ST-500 Microscopy Cryostat under high vacuum (~ 10^{-6} Torr). Figure 2.5a displays the electrical transfer characteristics of a 9 nm (~ 15 layer) thick $PdSe_2$ transistor at room temperature. The device exhibits a predominately n-type behavior with an on/off ratio greater than ~ 10^4, which is better than a previous report. [48] The linear output characteristic of the $PdSe_2$ device for gate voltages sweeping from -80 V to 80 V are shown in Figure 2.5b and can be attributed to thermally assisted tunneling through the Schottky barrier. [50]

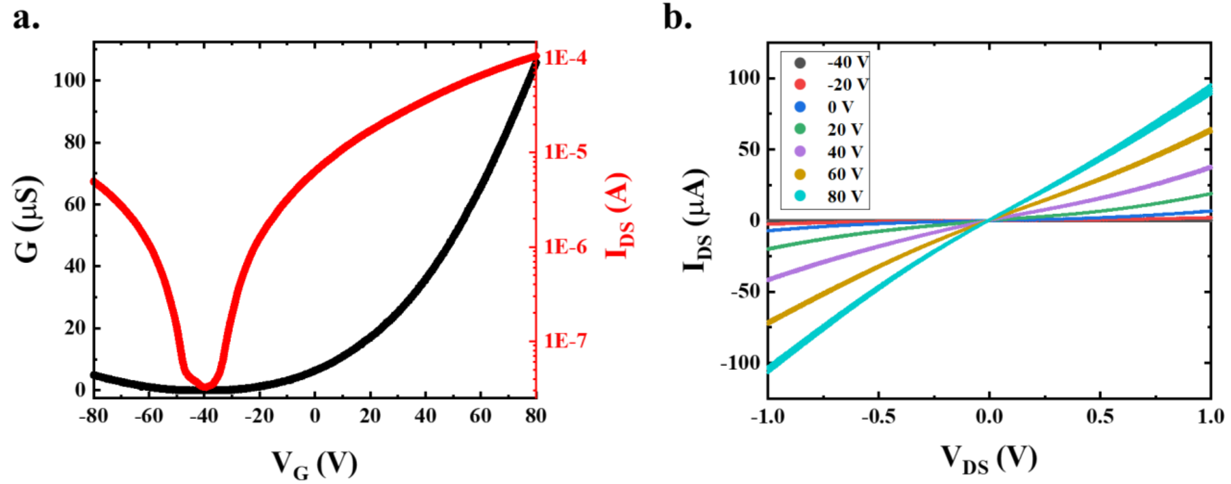

Figure 2.5 Electrical Transport of $PdSe_2$ Phototransistors. (a) Gate-dependent electrical transport of the PdSe2 phototransistor. On/off characteristics seen by the right log scaled y-axis in red. (b) The output characteristics of the device at various gate voltages.

The field-effect electron mobility of the device was calculated to be ~92 $cm^2V^{-1}S^{-1}$ at room temperature by using equation (6). Where C_G is the back gate capacitance of the SiO_2 layer, L and W are the length and width of the channel, respectively, G is the conductance, and V_G is the applied back gate voltage.

$$\mu_{FET} = \left(\frac{1}{C_G}\right)\left(\frac{L}{W}\right)\left(\frac{dG}{dV_G}\right) \qquad (6)$$

Although the field-effect mobility observed in this device and the other measured devices (ranging from ~60 $cm^2V^{-1}S^{-1}$ to ~290 $cm^2V^{-1}S^{-1}$) is significantly lower than the theoretical prediction, [46] it is comparable to or better than other experimental measurements. [43, 48] This variation of mobility is partly attributed to the anisotropic mobility predicted in $PdSe_2$, which varies by a factor of four in the x-axis vs y-axis direction. [46] Furthermore, the observed field-effect mobility of the $PdSe_2$ devices is also limited by the presence of a substantial Schottky barrier (one measuring ~180 meV) at the electrical contacts of these devices as shown in Figure 2.6b.

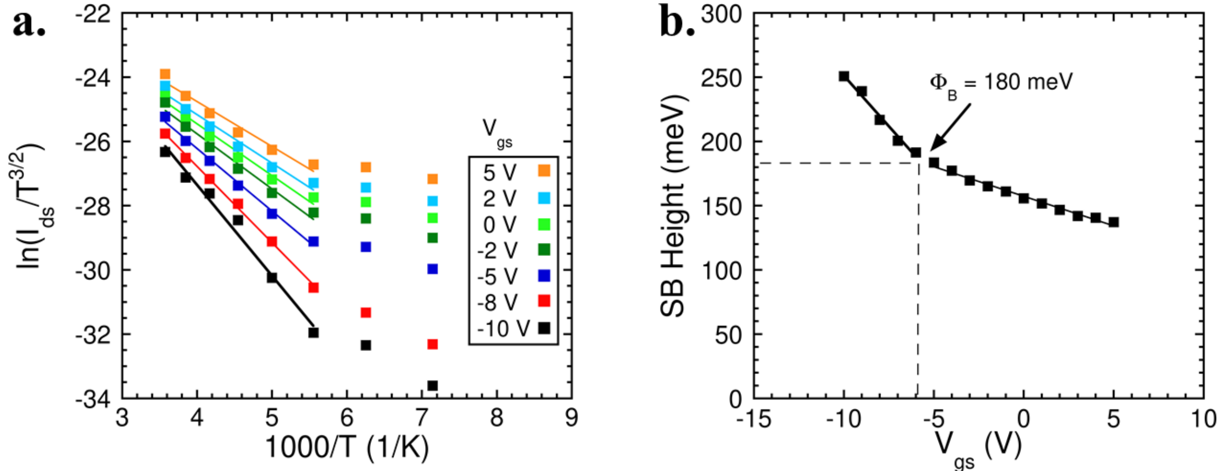

Figure 2.6 Schottky Barrier Height Extraction. (a) The Arrhenius plots for several back-gate bias voltages measured with drain voltage bias at 100 mV. The slope of each curve yields the effective Schottky barrier height at the corresponding gate bias. (b) The extracted effective Schottky barrier height at the various back-gate bias voltage, where the flatband electron Schottky barrier height is measured to be 180 meV.

The Schottky barrier height (SB Height here) can be found from the slopes of ln ($I_{DS}/T^{3/2}$) vs 1000/T at a constant positive drain-source bias as a function of temperatures and varying gate voltages as shown in Figure 2.6a and 2.6b. At the flat band gate voltage, the discontinuity in linearity seen in Figure 2.6b, the SBH is extracted. This is done by modeling the device as two Schottky diodes (one at the source and the other at the drain) connected by the $PdSe_2$ channel in the thermionic emission regime.[51] At low doping levels in TMDCs and below the flat band condition (downward shaped band bending in the n-type $PdSe_2$), charge injection is governed by this thermionic emission.[52] Above the flat band (upward shaped band bending in $PdSe_2$) condition thermionic field emission (tunneling) will also substantially contribute to the current which deviates from the thermionic emission regime and is responsible for the change in slope found above the flat band voltage. Under a positive drain-source bias the majority of the voltage is consumed at the source contact for n-type materials thus dominating the behavior of the transistor. The current density, J_{DS}, is given by the following equation (7). Where A^{*}_{2D} the 2D

Richardson constant, T is the temperature, q is the electron charge, Φ_B is the Shottky barrier height, k_b is the Boltzmann constant, and V_{DS} is the applied voltage at the junction.[53-56]

$$J_{DS} = A^*{}_{2D} T^{\frac{3}{2}} e^{\left(-\frac{q\Phi_B}{k_b T}\right)} \left[1 - e^{\left(-\frac{qV_{DS}}{k_b T}\right)}\right] \tag{7}$$

When $qV_{DS} >> k_bT$ (for these experiment with V_{DS} = 100mV, 100meV >>> 25meV, results in the bracketed term equaling ~0.98), the above equation (7) reduces to the following equation (8) and at low gate voltages (in the subthreshold regime) can be used to create Figure 2.6a and 2.6b.[15, 52, 57]

$$J_{DS} = A^*{}_{2D} T^{\frac{3}{2}} e^{\left(-\frac{q\Phi_B}{k_b T}\right)} \tag{8}$$

To investigate the photoresponse of the $PdSe_2$ devices, spatially resolved SPCM were performed. Figure 2.7b shows the scanning photocurrent image of the $PdSe_2$ device under 1060 nm illumination at a zero gate and zero drain-source bias, whose corresponding reflection image was recorded simultaneously and is shown in Figure 2.7a. The electrodes and $PdSe_2$ channel are outlined in gray and purple dashed lines, respectively. Strong photocurrent signals observed at the metal-$PdSe_2$ junctions are likely due to the creation of Schottky barriers from the Fermi level alignment at the junctions, which results in built-in electric fields that can efficiently separate photo-excited electron-hole pairs (EHPs) to generate photocurrent signals. [58] This is further suggested by the negligible photocurrent response at the center of the channel due to the relatively flat band structure at this location.

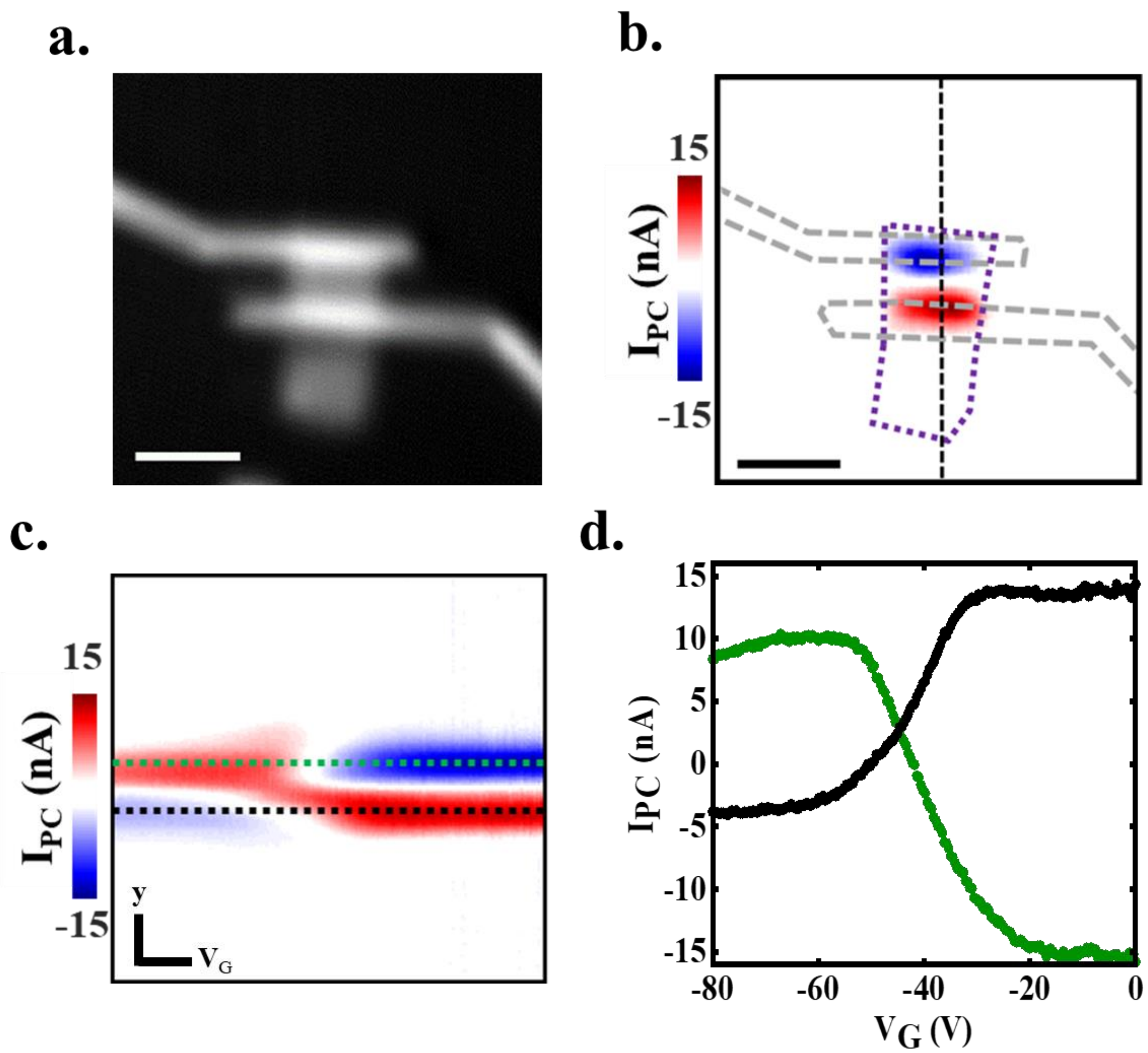

Figure 2.7 SPCM of $PdSe_2$ Phototransistors. (a) Reflection and (b) scanning photocurrent images of a typical $PdSe_2$ phototransistor under 1060 nm illumination as well as zero back gate and zero drain–source bias. Metal electrodes and few-layer $PdSe_2$ channel are outlined by gray and purple dashed lines, respectively. The horizontal scale bars in (a) and (b) are 5 microns. (c) Gate-dependent photocurrent signals along the vertical black dashed line in (b). In (c), the vertical direction is y position and the horizontal direction is back gate voltage. The corresponding scale bars are 2.5 microns and 10 V, respectively. (e) Green and black curves represent photocurrent responses along the green and black dotted lines in (c), respectively.

To further study the photocurrent generation mechanisms, gate-dependent scanning photocurrent measurements were performed by sweeping the gate voltage from -80 V to 0 V while recording the photocurrent along the $PdSe_2$ channel (Figure 2.7c) under zero drain-source bias. The photocurrent signal exhibits monotonic gate voltage dependence in the off-state (Figure 2.7d),

indicating that the PVE plays an important role in its photocurrent generation.[59, 60] Upon laser excitation, EHPs will be generated locally and driven in opposite directions by the built-in electric field due to the Fermi level alignment creating Schottky barriers at metal-$PdSe_2$ junctions. Since the electronic energies are higher near the metal contacts than those in the middle of the $PdSe_2$ channel when the device is electrostatically n-doped (Figure 2.8a), photo-excited electrons will be injected into the channel, leading to a negative (positive) current flow at the drain (source) electrode. When the back gate voltage decreases to -44 V, the flat band voltage, V_{FB}, is reached (Figure 2.8b). Here negligible photocurrent response is observed. Similarly, the polarity of photocurrent is reversed when the back gate voltage is below the flat band voltage due to the electrostatic p-doping. (Figure 2.8c).

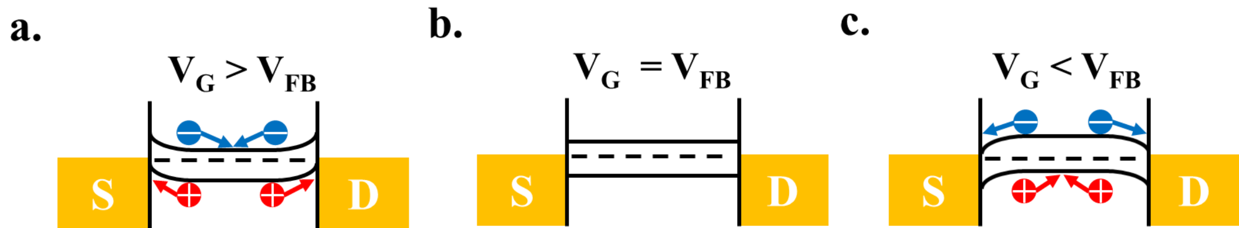

Figure 2.8 Band Bending Conditions of $PdSe_2$ Phototransistors. Schematic of the band bending in the $PdSe_2$ in response to a back gate voltage showing below the flat band voltage in (a) when the material is electrostatically n-doped, the flat band condition in (b), above the flat band voltage in (c) when the material is electrostatically p-doped.

Interestingly, the photocurrent signals start to saturate when V_G is larger than -20 V (Figure 2.7d), which can be attributed to reduced gate-tunability of the band bending in the depletion regions as the Fermi level approaches the conduction band edge. In addition to photovoltaic mechanisms, other photocurrent generation mechanisms may also contribute to the photocurrent. Under illumination, the laser beam can also locally heat $PdSe_2$ to produce photocurrent response via either the PBE or the PTE.

When a laser beam scans over the $PdSe_2$ channel, the temperature of the channel increases due to light-induced heating leading to the electrical conductance increase of the channel.[61, 62] The change in the conductance with a change in temperature is shown in Figure 2.9a. This change in conductance should contribute a photobolometric current that scales with the drain-source voltage.[61] Thus the expectation would be to see a photocurrent that scales linearly with drain-source bias. But as shown in Figure 2.9b the photocurrent response does not scale linearly with the drain–source bias, suggesting that the PTE may be a larger contributor to the photocurrent generation. To further examine these relative contributions and to establish the presence of the PTE, spatially-resolved scanning photocurrent images of the $PdSe_2$ device are examined. As shown in Figure 2.9c a strong photocurrent "tail" is observed in the metal–$PdSe_2$ junction region, indicating that the PTE also contributes to the photocurrent generation due to the differing Seebeck coefficients between the $PdSe_2$ channel and the gold electrodes.[14, 29]

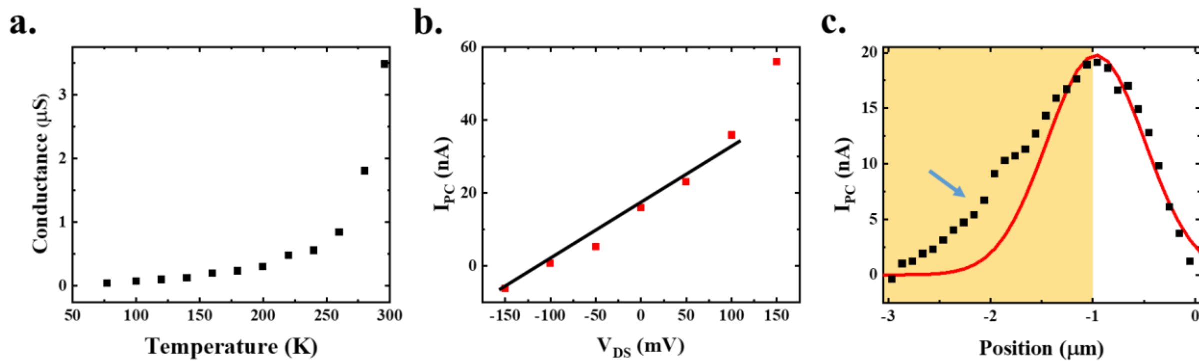

Figure 2.9 Thermal Photocurrent Generation Analysis in $PdSe_2$ Phototransistors. (a) Conductance of a $PdSe_2$ device as a function of temperature; (b) photocurrent response of the device as a function of drain-source bias (red dots represent experimental data and black line is a linear fitting); and (c) a line profile of the photocurrent response across the metal-PdSe2 junction is shown by the black dots. The red solid curve is the related Gaussian fitting. The green arrow denotes the photocurrent "tail" on the electrode. The yellow background indicates the position of the electrode.

Since the Seebeck coefficients of $PdSe_2$ and the gold electrodes are different, a photothermal voltage (V_{PTE}) across the metal-$PdSe_2$ junction exists. Using the Mott relation equation (3), and noting that G is due to constants and modulated by the back gate voltage the

chain rule can be applied to get a modified Mott relation in order to obtain the Seebeck coefficient as shown in equation (9). [28, 29, 63]

$$S = \left(\frac{\pi^2 k_b^2 T}{3e}\right)\left(\frac{1}{G}\frac{dG}{dV_G}\right)\left(\frac{dV_G}{dE}\bigg|_{E=E_F}\right) \tag{9}$$

Here, the last term can be estimated as follows. When the Fermi level moves from the valence band to the conduction band, the barrier height E_b changes linearly with V_G ($\delta E_b = e\alpha\delta V_G$), where α is a numerical constant that measures how effectively the gate voltage modulates the band energy.[58, 64] The measured shut-off gate voltages for p-type and n-type conductance are -60 V and -20 V, respectively (Figure 2.5a). The band gap for few-layer $PdSe_2$ is 1.17 eV; therefore, the calculated $\alpha \approx 0.029$ which can be used to infer the Seebeck coefficient. A maximum Seebeck coefficient of $PdSe_2$ (~ 74 μV/K at V_G = -10 V), consistent with the theoretically-predicted value is obtained.[47] Therefore, photocurrent signals of $PdSe_2$ in the on-state may partially result from the PTE.

Furthermore, wavelength-dependent scanning photocurrent measurements were taken to investigate additional photocurrent generation mechanisms in few-layer $PdSe_2$. Figure 2.10 shows photocurrent responses of the $PdSe_2$ devices with different thicknesses. The thickness of a monolayer flake of $PdSe_2$ is ~0.6 nm.[43] For thinner $PdSe_2$ phototransistors (e.g. 9 layer), a dominant resonance peak was observed at 1060 nm (1.17 eV), which is comparable with the indirect band gap of bi-layer $PdSe_2$ revealed by scanning tunneling spectroscopy (1.15 ± 0.07 eV).[65] Interestingly, when the thickness of $PdSe_2$ increases, more and more small peaks appear around this near-IR region, such as peaks located at 1030 nm (1.20 eV) and 1090 nm (1.14 eV), respectively. These distinct peaks are likely the result of different optical transitions between the local valence band maxima along the Γ-X line and the local conduction band minima located at the Γ-M line, [45] which are affected by the thickness due to the strong interlayer coupling in the

puckered pentagonal morphology of $PdSe_2$.[66] This may also explain the uncertainty of the few-layer $PdSe_2$ band gap characterization in previous optical absorption measurements (0.7 – 1.3 eV).[43]

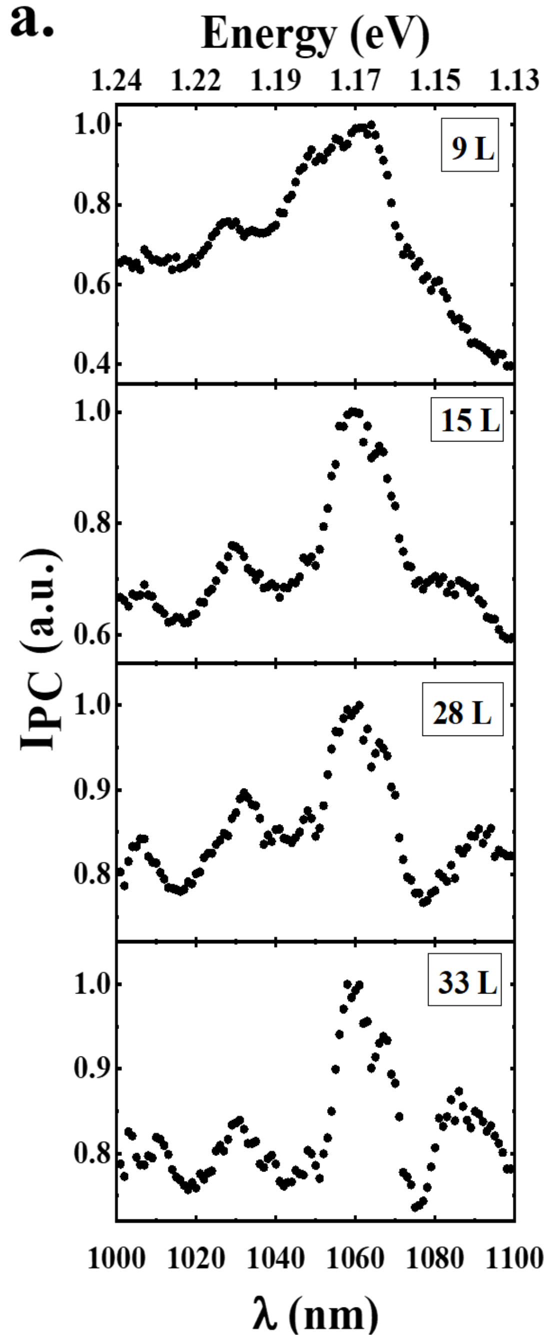

Figure 2.10 Wavelength Dependence of $PdSe_2$ Phototransistors. (a) Wavelength dependent photocurrent response for various devices thicknesses under zero back gate voltage and zero drain-source bias. Each layer of $PdSe_2$ is ~0.6 nm resulting in corresponding thicknesses of ~5.4nm (9L), ~9nm (15L), ~16.8 nm (28L) and ~19.8nm (33L).

Next, bias-dependent SPCM was performed on the $PdSe_2$ phototransistors at zero gate and different drain-source biases from -150 mV to 150 mV (Figure 2.11a). Here the electrodes and few-layer $PdSe_2$ channel are outlined in gray and purple dashed lines, respectively. Regardless of the applied bias, strong photocurrent signals are observed at the metal-$PdSe_2$ junctions while the photocurrent response in the middle of the $PdSe_2$ channel is negligible. For comparison, corresponding horizontal cut lines along the channel (black dashed lines in Figure 2.11a) are shown in Figure 2.11b. When a large positive bias is applied to the device, the positive photocurrent intensity at the source contact electrode increases. Similarly, the negative photocurrent signal in the drain contact electrode intensifies as the device is negatively biased. This increase in photoresponse under the application of a larger bias is primarily due to the enhancement of the electric field in the depletion region at the electrical contacts, which allows for the more efficient separation and collection of the photo-excited EHPs. Since the slope of the electrostatic potential (or the local electric field) with respect to position is proportional to the photocurrent intensity, the photocurrent curves were numerically integrated in Figure 2.11b to obtain the electrostatic potential (Figure 2.11c). The potential change in different regions at various biases can easily be identified. Large potential drops near the electrode contact regions and relatively flat band in the middle of the $PdSe_2$ channel are observed, indicating the presence of contact resistances due to the Schottky barriers between metal electrodes and the $PdSe_2$ channel. By selecting electrode metals with proper work functions and eliminating (or reducing) the Fermi level pinning, the Schottky barrier between electrode contacts and the $PdSe_2$ channel may be minimized.[35, 56, 67]

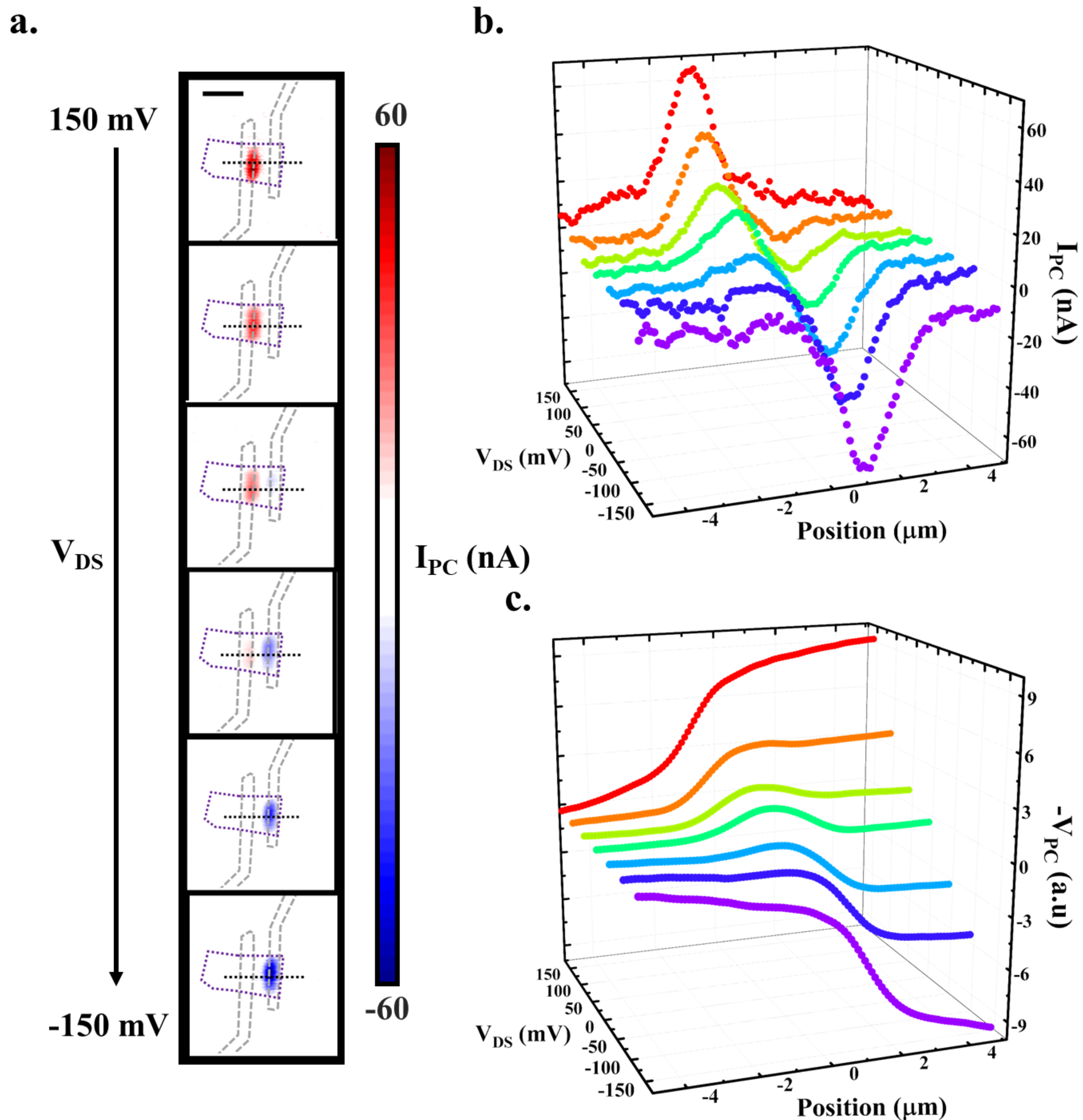

Figure 2.11 Analysis of Potential Distributions in $PdSe_2$ Phototransistors. (a) Scanning photocurrent images (20 μm by 20 μm) taken with drain–source biases from 150mV to -150 mV in increments of 50mV excluding the zero bias image and under zero back gate voltage. The scale bar is 5 microns. The electrodes of the device are outlined in gray. The $PdSe_2$ flake is outlined in purple dashed lines. (b) Corresponding photocurrent intensity along the black dashed lines in (a). (c) Electrostatic potential computed by numerically integrating the photocurrent intensity curves from (b).

The photoresponse dynamics of $PdSe_2$ phototransistors are also studied through time-resolved scanning photocurrent measurements. This was performed by applying ON/OFF light

modulation with an optical chopper while photocurrent signals were recorded as a function of time in order to measure the rise and decay time constants. The device performed similarly over thousands of cycles of ON/OFF light modulation signifying the stability of the temporal response of the device. Figure 2.12a shows three typical cycles. By applying a single exponential function to fit the rising and decaying regions of the curve, the obtained rise and decay time constants are ~ 156 μs and ~ 163 μs (Figure 2.12b), respectively, which are more than two orders of magnitude faster than those of other noble TMDCs based devices.[39, 40, 42, 68] These extremely fast response times are partly attributed to the high mobility of charge carriers in $PdSe_2$. Additionally, power dependence measurements are performed to examine the significance of trap states on the reported response time. The photocurrent signals have a nearly linear relationship with incident power ($I_{PC} \propto P^{0.85}$) as shown in Figure 2.12c. The slight deviation from the linear relationship may result from some defects and trap states in the $PdSe_2$ channel which may be responsible for the longer decay time relative to the response time.[17, 40, 46, 69, 70]

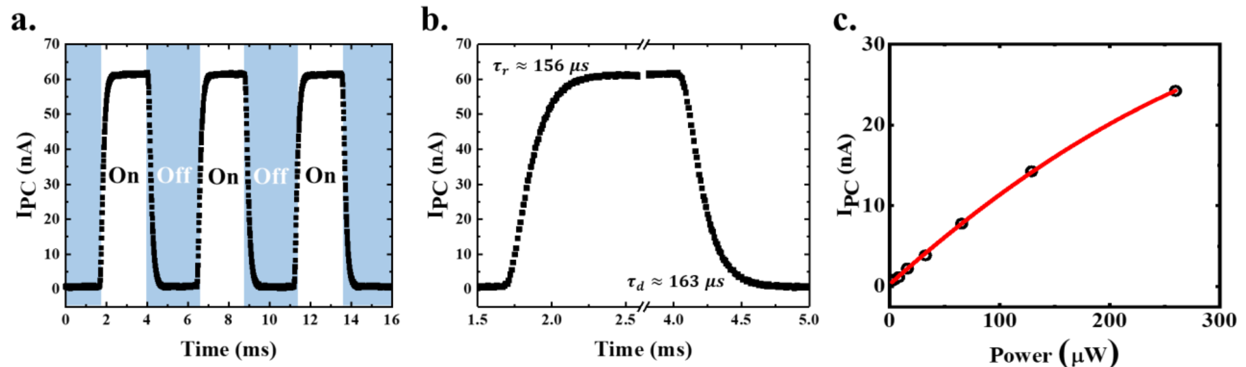

Figure 2.12 Photoresponse Dynamics and Power Dependence of $PdSe_2$ Phototransistors. (a) Photocurrent signals as a function of time under 1060 nm illumination. (b) Zoom-in of the rising and decaying regions of the photocurrent signals from (a) showing the rise and decay time constants of ~156 μs and ~163 μs, respectively. (c) Power-dependent photocurrent behavior of the device, where the red solid line shows the trend line of $I_{PC} \propto P^{0.85}$.

In this chapter, electrical transport and scanning photocurrent measurements are used to demonstrate that strong photocurrent responses in $PdSe_2$ phototransistors primarily result from the

PVE when the devices turn off and are partially related to the PTE when the devices are in the on-state. $PdSe_2$ devices with Seebeck coefficients as high as ~74 μV/K at room temperature, which is consistent with theoretical predications is also shown. Moreover, thickness-dependent photocurrent resonance peaks are observed in the NIR region, which are likely due to strong interlayer coupling-induced indirect optical transitions in few-layer $PdSe_2$. Additionally, a fast response time of ~ 156 μs has been achieved in $PdSe_2$ phototransistors, which is more than two orders of magnitude faster than other noble TMDC devices. This work not only presents new insight into the optical transitions and photocurrent generation mechanisms of $PdSe_2$, but adds insight into engineering future noble TMDCs based optoelectronic devices.

Chapter 3 NIR Detection Using Van-der Waals Heterojunctions

3.1 Introduction to Van-der Waals Heterojunctions

The explosion of research into 2D materials catalyzed by the isolation of graphene has not only propelled the search for other atomically thin materials possessing similar properties but also has led to considerations of combining low-dimensional materials in unique ways. The growth of the 2D material library to include metals, semiconductors, semimetals, and insulators as well as the discovery of superconductivity, charge-density wave states, and ferromagnetism in these materials enables the exploration of materials physics in a new dimension and offers the potential for devices with diverse and multifunctional properties. [4] The layered nature of 2D materials presents a way to combine materials not offered by their 3D counterparts. Strong in plane covalent bonds and weak out of plan van der Waals bonds have made the atomic-scale LEGO building a wildly successful endeavor.[71] A schematic of this idea is shown in Figure 3.1.

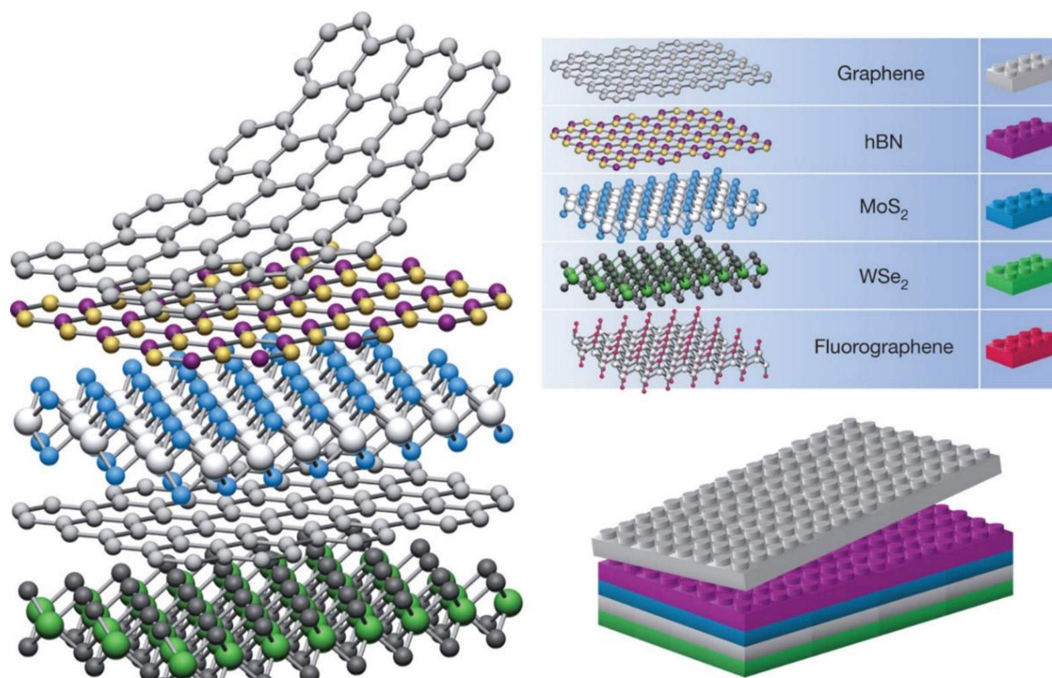

Figure 3.1 LEGO Building Approach to 2D Materials. Schematic illustrating the concept of 2D material Lego Building. Reprinted with permission from Ref [71]. Copyright © 2013 Macmillan Publishers Limited.

Furthermore, traditional constraints of lattice mismatch as well as the presence of dangling bonds in bulk materials are not a significant issue in 2D materials which results in atomically sharp interfaces.[71, 72] Stacking also presents another degree of freedom in the way layers are aligned relative to one another which has led to the discovery of new physical phenomenon such as the self-similar Hofstadter butterfly states in graphene/h-BN stacks or the discovery of a ‘magic’ angle in bilayer graphene stacks resulting in unconventional superconductivity.[73, 74] Despite the nearly infinite flexibility offered by stacking, it is a somewhat slow and intensive process. This has led to the exploration of large-area crystal growth techniques such as chemical vapor deposition or epitaxial growth. In addition to vertical heterostructures, 2D materials also offer the possibility to create lateral heterostuctures via in-plane stitching.[75] This offers the possibility of devices at the atomic limit, as with the demonstration of nanometer scale PN junctions.[76] A comparison of a vertical and lateral heterojunction is shown in Figure 3.2

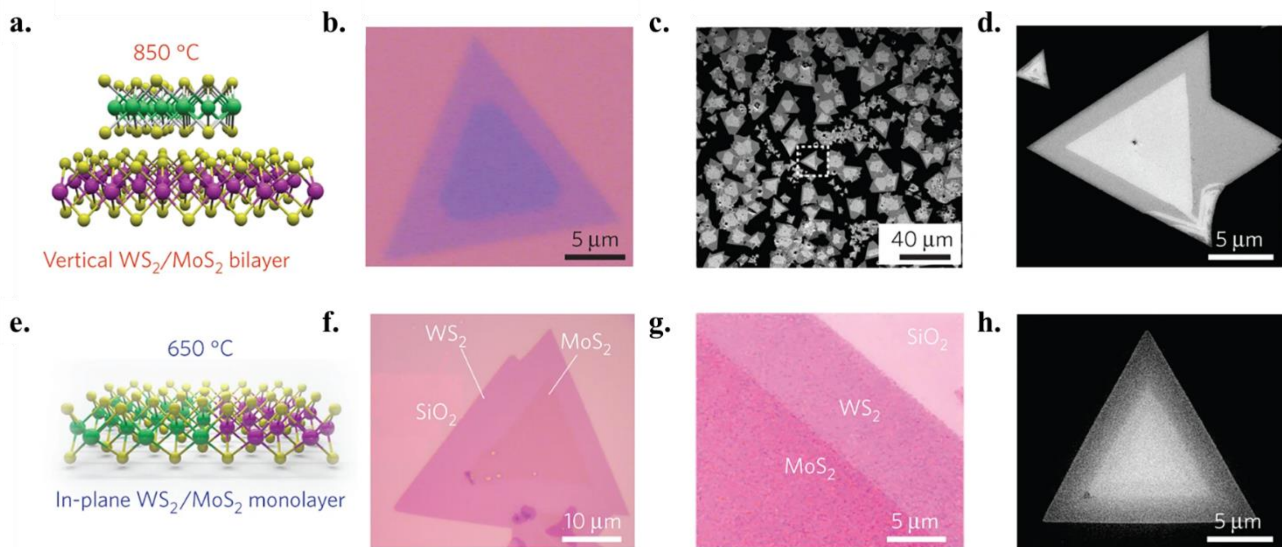

Figure 3.2 Comparison of Vertical and Lateral Heterojunctions. (a) – (d) Schematic and imaging of a vertical 2D TMDC heterostructure. (e) – (h) Schematic and imaging of a horizontal 2D TMDC heterostructure. Both hterostuctures are grown via chemical vapor deposition. Reprinted with permission from Ref [77]. Copyright © 2014 Macmillan Publishers Limited.

The realm of 2D material heterostructures can even be further expanded by examining the combination of materials with different dimensionalities.[78] The most common 0 D materials to be combined with 2D structures are quantum dots. The use of PbS quantum dots integrated with MoS_2 sheets has shown exceptional NIR spectral response via a facile liquid phase assembly procedure.[79] The combination of 1D and 2D materials has also been previously demonstrated in our group by the combination of carbon nanotubes and MoS_2 sheets which showed strong polarized NIR photoresponses.[80] Additionally, the layering of 2D materials upon bulk 3D materials can also show enhanced properties. The combination of a 2D SnS film on top of a 3D n-type Si substrate has also shown excellent NIR photodetection capabilities.[81] And perhaps unsurprisingly the combination of 3D metallic electrodes to 2D materials is ubiquitous in the metallization process that enables the investigation of 2D material properties. Schematics of the possibilities of 2D material heterojunctions are shown in Figure 3.3.

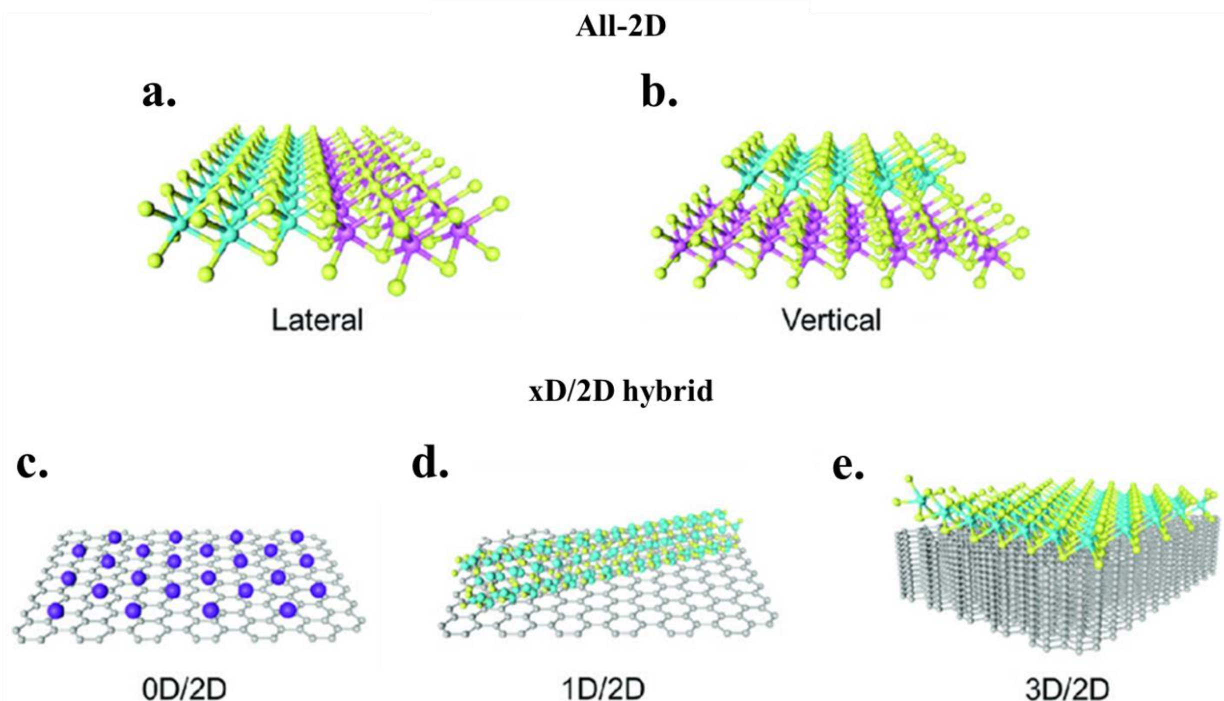

Figure 3.3 Summary of the numerous 2D HeteroStructures. Schematics of a lateral (a) vs vertical (b) heterojunction. Reprinted with permission from Ref [82]. Copyright © 2020 Wiley-VCH GmbH.

3.2 BP-MoS_2 Heterojunctions

In the fabrication of 2D material heterojunctions, BP and MoS_2 have attracted significant attention. Both vertical and lateral BP-MoS_2 heterojunctions have shown excellent properties in a variety of electrical devices. FETs have been created showing on-off ratios up to nearly 10^8 and subthreshold swings as low as 65 mV/dec at 300K. [83-85] Ultra high gain tunable binary and ternary logic inverters as well as diodes have been demonstrated. [86, 87] Beyond electrical devices, optoelectronic, and photonic devices have also received attention such as LEDs, photodetectors, photovoltaic solar cells, and optical modulators.[88-91] Theses devices also possess potential for NIR applications due to their sensitivity to photons in the desired energy/wavelength range (from ~0.8 eV to ~1.6 eV). Though the band gap of MoS_2 ranges from a direct band gap of ~1.9 eV in its monolayer form to an indirect gap of ~1.3eV in bulk, [92] the band gap of BP is direct and ranges from ~ 0.3 eV in bulk to 2 eV in monolayer. [93, 94]. For example, a vertical heterojunction formed by stacking BP and MoS_2 flakes together displays a high photoresponsivity up to 22.3 A/W under 532 nm illumination and 153.4 mA/W under 1550 nm illumination, [95, 96] Beyond photoresponsivity, response time is a critical parameter for photodetectors. Noticeably among BP, MoS_2, and BP-MoS_2 devices, a great variety of photoresponse times have been reported under various conditions which are summarized in Table 3.1.

Table 3.1 Summary of BP, MoS_2, and BP-MoS_2 Heterojunction Response Times.

Device Material	V_{DS}	V_G	τ_{rise}	λ	Ref.
Few Layer BP	200 mV	0 V	1 ms	940 nm	[94]
	100 mV	0 V	40 μs	780 nm	[97]
	100 mV	0 V	4.8 ms	1550 nm	[98]
	-50mV	-10 V	5 ms	900 nm	[99]
1L MoS_2	8 V	-70 V	600 ms	561 nm	[100]
	1 V	50 V	50 ms	532 nm	[18]
	1 V	-2 V	~1 s	633 nm	[101]
BP-MoS_2	0 V	3 V	15 μs	1550 nm	[102]
	0 V	0 V	~1 s	582 nm	[103]
	-2 V	0 V	150 μs	457 nm	[104]

It is well-known that the response time of photodetectors is limited by the carrier transit time, [105] which depends on electrical transport properties of individual channels and junctions. Previous reports indicate that gate voltages can modify the Schottky barriers between TMDCs and metal electrodes and then influence the electrical transport properties of devices. [86, 106] But no work to date has examined the tuning of photo response speed with the systematic study of gate voltages and laser wavelength illuminations. Previous works have observed the changing of photoresponse speed with different channel lengths for devices [99] or by altering the applied gate voltage [107], but do not offer a comprehensive explanation and in particular have not studied variable wavelengths. The response of devices across a broad range of operating conditions is essential in understanding 2D heterostructure device engineering.

3.2.1 Results and Discussion

Here the photoresponse dynamics in BP-MoS_2 heterojunctions are systematically investigated through gate- and wavelength-dependent scanning photocurrent measurements. It is found that the Schottky barrier at the MoS_2-metal interface is likely to play a significant role in the rise and decay times of the heterojunction. When the MoS_2 channel is in the on-state, photo-excited carriers can tunnel through the narrow depletion region at the MoS_2-metal interface, leading to a short carrier transit time. For both the rising and decaying region a response time constant of 13 μs has been achieved, irrespective of the incident laser wavelength. The reported response time constants are comparable or better than those of other BP-MoS_2 heterojunctions as well as BP and MoS_2 based phototransistors. In contrast, when the MoS_2 channel is in the off-state, the sizeable Schottky barrier and depletion width make it difficult for photo-excited carriers to overcome the barrier, which significantly delays the carrier transit time and thus the photoresponse speed. Under this condition since photo-excited carriers induced by short wavelength photons possess higher

energy, they have a higher probability to overcome the Schottky barrier at the MoS_2-metal interface resulting in a relatively fast response in comparison with that of carriers excited by the incident light with a long wavelength. Consequently, the rise and decay time constants of the heterojunction increase with increasing incident laser wavelength. These fundamental studies not only provide an in-depth understanding of the photoresponse dynamics in BP-MoS_2 heterojunctions, but also offer a new way to reduce the response time of 2D heterojunctions by engineering 2D material-metal interfaces.

Devices to facilitate this study were provided by generous collaborators: Dr. Bhim Chamlagain, and Dr. Upendra Rijal under the direction of Dr. Zhixian Zhou. Multilayer MoS_2 flakes were produced by mechanical exfoliation of MoS_2 crystals and subsequently transferred to Si/SiO_2 substrates (degenerately-p-doped Si substrates with a 290 nm SiO_2 oxidation layer). Thin flakes of BP that had been mechanically exfoliated were selected and then placed on the target MoS_2 flake on the substrate to form a BP–MoS_2 heterojunction in the overlap region. To complete the device metal electrodes (5 nm Ti/40 nm Au) were defined by standard electron beam lithography and deposition processes. Optical microscopy and a Park-Systems XE-70 noncontact mode atomic microscopy were used to identify and characterize thin MoS_2 (~3 nm) and BP flakes (~14 nm). The devices were then mounted in a chip carrier with carbon tape where contacts were wire bound and the gold backing of the chip carrier was also wire bound to facilitate a back gate voltage via the degenerately-doped Si substrate. A schematic and an optical image of the BP-MoS_2 heterojunction is presented in Figure 3.4a and 3.4b, respectively. The BP and MoS_2 flakes are outlined by purple and blue dashed lines, respectively, and the electrodes are outlined in gray dashed lines.

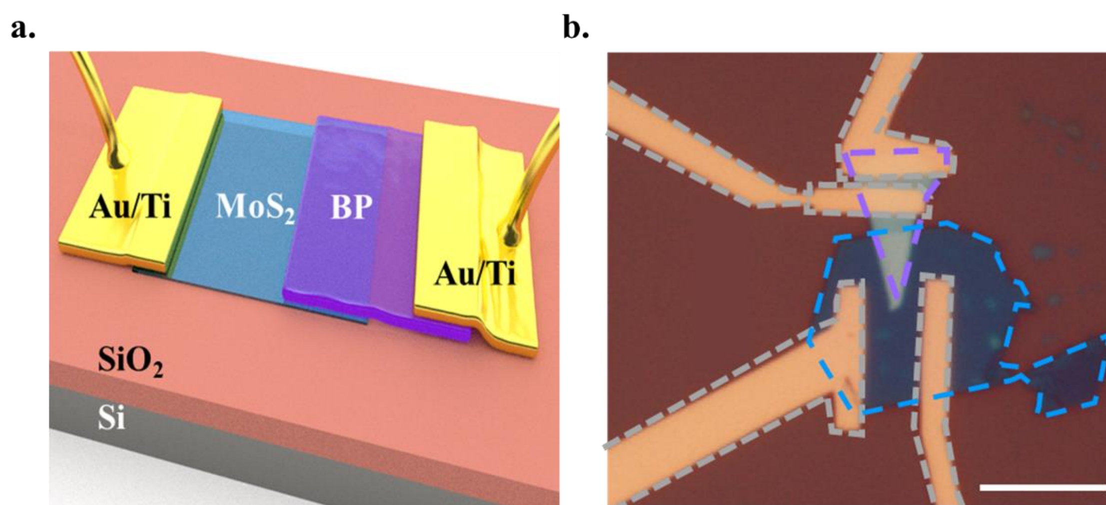

Figure 3.4 BP-MoS_2 Heterojunctions. (a) A schematic of the BP-MoS_2 heterojunction device. (b) An optical image of the as-fabricated device. BP and MoS_2 are outlined in purple and blue dashed lines, respectively. The electrodes are outlined in gray dashed lines. The scale bar is 10 μm.

To assess the electrical properties of these BP-MoS_2 heterojunction devices electrical transport measurements were taken in a Janis ST-500 microscopy cryostat at room temperature under high vacuum (~10^{-6} torr). The four electrode configuration of the device permits the examination of the electrical characteristics of both the individual BP and MoS_2 flakes where the gate voltages were applied to the Si substrate to adjust the carrier concentration in each material. Figure 3.5a presents the gate-dependent transport characteristics of the two individual flakes, in which the BP and MoS_2 flakes show typical p-type and n-type behavior at a zero gate voltage, respectively. [108, 109] From this gate dependent behavior the field-effect mobility values, μ_{FET}, of the BP and MoS_2 can be obtained from equation (6). This yields mobility values of ~53 $cm^2\ V^{-1}\ s^{-1}$ for the MoS_2 channel and ~40 $cm^2\ V^{-1}\ s^{-1}$ for the BP channel.

Though BP is theoretically predicted to have a high mobility upwards of ~27,000 $cm^2\ V^{-1}\ s^{-1}$, its extreme sensitivity to ambient conditions, despite fabrication and storage in an appropriate environment, will lead to unavoidable degradation within as little as an hour after without

passivation. [110, 111] Unfortunately, passivation processes are known to significantly alter the optical properties of BP such as the introduction of photo-doping when passivated with hexagonal boron nitride. [112] This produces a challenge when attempting to maximize the electrical as well as the optoelectronic properties of devices involving BP.

The *I-V* characteristics of the BP–MoS_2 junction were also explored at various gate voltages as seen in Figure 3.5b. Consistent with gate-tunable transport properties, strong rectification of the drain current can be seen at a zero gate voltage where unintentional doping occurs. As the gate voltage is modified, a decrease in these rectification properties is observed due to the modulation of carrier concentrations. These rectification properties are similar to traditional p-n junctions except the electrical tunability in vertical van Der Waals heterojunctions between two atomically-thin materials is likely attributed to tunneling-assisted interlayer recombination given the absence of a vertical depletion region.[113]

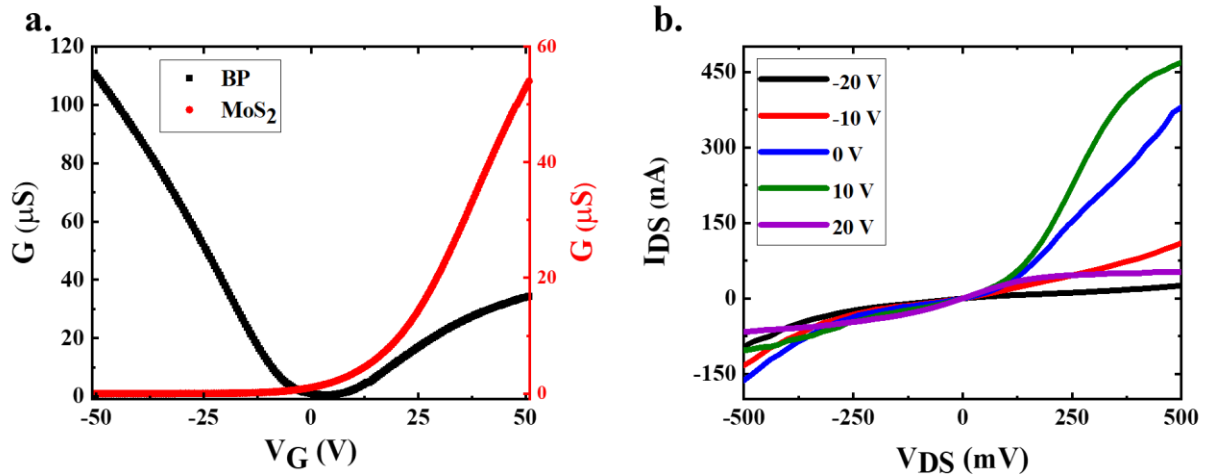

Figure 3.5 Electrical Transport Properties in BP-MoS_2 Heterojunctions. (a) Gate-dependent transport characteristics of the BP (black) and MoS_2 (red) channels of the device, respectively. (b) The electrical transport properties of the heterojunction under various gate voltages.

To begin the investigation of the optoelectronic properties of these heterojunctions spatially-resolved photocurrent mappings were generated using SPCM. Under 650 nm illumination, the reflection and photocurrent images of a BP-MoS_2 heterojunction were collected

simultaneously to locate the position of photocurrent signals. As shown in Figure 3.6a and 3.6b, a strong photocurrent response was observed in the overlap region between BP and MoS_2 flakes, where the built-in electric field can efficiently separate the photo-excited electron-hole pairs to generate photocurrent signals similar to a PN-junction. Due to this, the PVE is attributed as the primary photocurrent generation mechanism. To further investigate the optoelectronic properties of the device power dependent photocurrent measurements are extracted from the maximum response of the device under exponentially increasing powers. The photocurrent (red) as a function of incident laser power shows a sublinear dependence resulting in a monotonous decrease in photoresponsivity ($R = I_{PC}/P$, black) as shown in Figure 3.6c. This behavior can be explained by the presence of trap states in the BP or MoS_2 or at their interfaces. [17, 114] As the illumination power increases most trap states are filled and further increases in power cannot continue to increase the photoresponse. [115, 116] Furthermore, a peak responsivity of ~50 mA W^{-1} was observed, which is comparable to previous BP-MoS_2 junctions and greater than previously reported for BP phototransistors. [89, 94, 117]

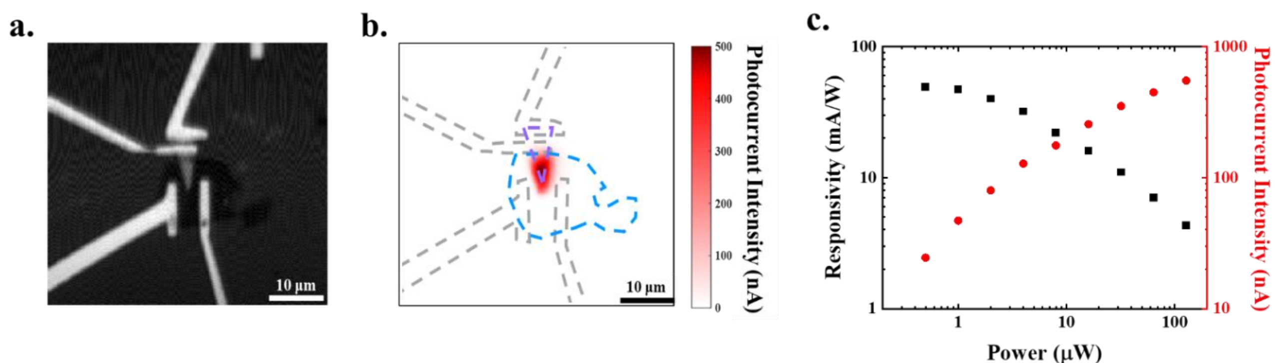

Figure 3.6 SPCM and Power Dependence of BP–MoS_2 Heterojunctions. (a) The reflection and f) scanning photocurrent images of the BP–MoS_2 heterojunction under a zero drain-source bias and zero gate voltage. The gray dashed lines show the outline of the electrodes. The purple and blue dashed lines represent BP and MoS_2 flakes, respectively.

To examine the output characteristics of BP-MoS_2 heterojunctions under both visible and near infrared illumination the heterojunctions were exposed to laser illumination with wavelengths of 650 nm and 1000 nm. Under 650 nm illumination (1.9 eV), sufficient photon energy is provided to efficiently excite electrons in MoS_2 as well as the BP to contribute to the photocurrent signals. Under 1000 nm (1.2 eV) illumination photocurrent responses are mainly attributed to the direct bandgap optical transition of few-layer BP. This is diagrammed in Figure 3.7a and 3.7b. The gate dependent output characteristics under zero drain-source bias and constant power reveal this effect as a stronger response is found under 650nm than 1000nm illumination as shown in Figure 3.7c. The asymmetry in the photocurrent response between negative and positive gate voltages is attributed to the ambipolar characteristic of the BP and its contribution to the photocurrent for both examined wavelengths. Additionally, the drain-source bias dependent output characteristics of the heterojunction under a gate voltage of 0 V with and without laser illumination show clear PVE. The open-circuit voltage and short-circuit current are 0.08 V and 0.06 μA for 1000 nm excitation and 0.13 V and 0.2 μA for 650 nm excitation, respectively, and can be seen in Figure 3.7d. In the middle of the yellow region, photo-excited electron-hole pairs become separated due to the built-in electric field at the heterojunction. When the forward bias is equal to the open-circuit voltage, the bias-driven flow is opposite to and cancel the flow induced by photo-excited EHPs, leading to a zero net current.

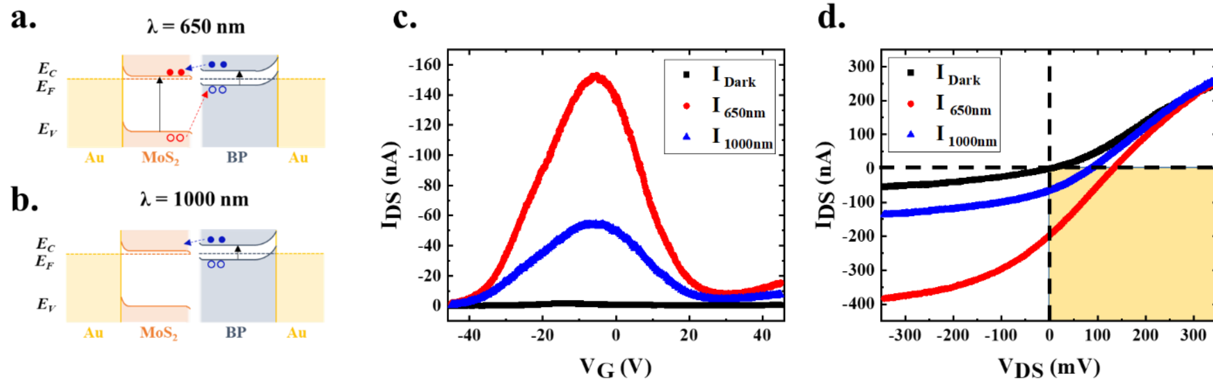

Figure 3.7 Photocurrent Generation in BP–MoS_2 Heterojunctions. Band diagram for the BP-MoS_2 heterojunction under (a) 650nm and (b) 1000 nm wavelength illumination. (c) Gate-dependent output characteristics under no illumination (black), 650nm illumination (red) and 1000nm illumination (blue). (d) Drain-Source bias dependent measurement under no illumination (black), 650nm illumination (red) and 1000nm illumination (blue). The yellow region highlights the PVE.

Critical to this study that aims to look at the variety of reported response times in BP and MoS_2 based devices is the examination of the temporal photocurrent response of the BP-MoS_2 heterojunction under varying gate voltages and incident wavelengths. An optical chopper was utilized to mechanically apply ON/OFF light modulation to the laser beam while photocurrent signals were collected as a function of time. The photoresponse of the heterojunction with an applied back-gate voltage of -20V recorded as a function of time while 650nm light is modulated is shown in Figure 3.8a. When the wavelength of this illumination is increased from 650nm (black squares) to 1000nm (maroon circles) a lengthening of the response can be observed in both the rise and decay of the photo response as shown in Figure 3.8b and 3.8c, respectively.

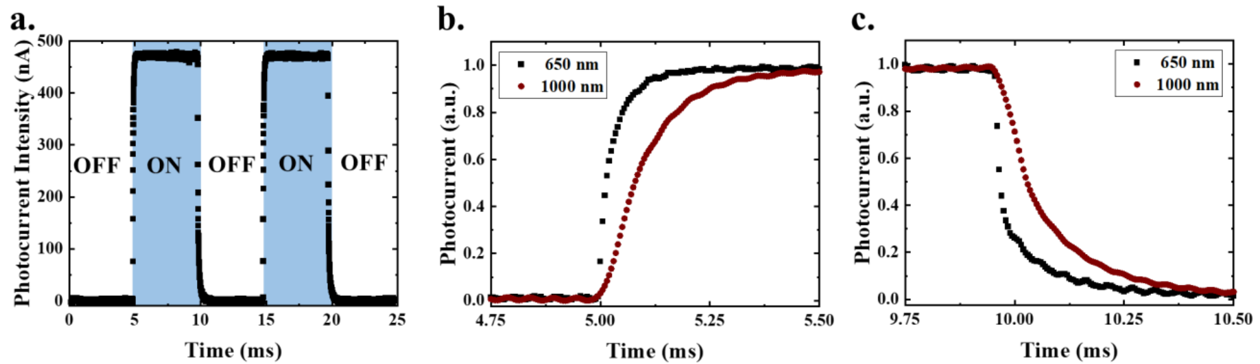

Figure 3.8 Photoresponse Dynamics in BP–MoS_2 Heterojunctions. (a) Photocurrent response as function of time under 650nm wavelength illumination while light is modulated on and off by an optical chopper at 200 Hz. The heterojunction is under -20V back-gate voltage. A zoom in of the rising (b) and decaying (c) of the photocurrent response at 650nm (black squares) and 1000nm (maroon circles). The same optical chopper frequency of 200 Hz is used and the device is under -20V back-gate voltage.

To systematically investigate this change the heterojunction was measured under three different gate voltages (-20V, 0V, and 20V) each at 100nm wavelength increments. To characterize the photo response speed the rise time (τ_r) and decay time (τ_d) constants where found by fitting the respective rising and decaying portions of the photoresponse curves with a single exponential fit function. As shown in Figure 3.9a, the rise time constant of the junction gradually increases from 35 μs to 90 μs when the illumination wavelength increases from 650 nm to 1000 nm while remaining under a -20 V back-gate voltage. But when the back gate voltage is maintained at 0V or 20V the rise time constant remains the same at ~22 μs and ~13 μs, respectively, under increased wavelength. Additionally, the rise time constant increases with decreasing gate voltage regardless of the wavelength. The same phenomenon is observed for the decay times as well. As shown in Figure 3.9b, the decay time constant gradually increases with wavelength from 47 μs to 119 μs and is under -20V back-gate voltage. And then when the back gate voltage is maintained at 0V or 20V the decay time constant remains the same at ~25 μs and ~17 μs, respectively, under increased wavelength.

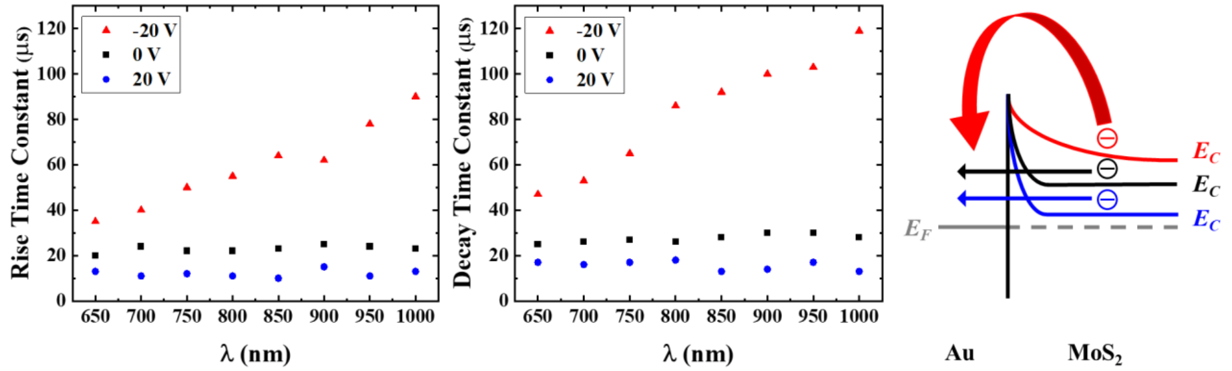

Figure 3.9 Tunable Photoresponse Speed in BP–MoS_2 Heterojunctions.(a) Rise and (b) decay constants as a function of wavelength and gate voltage. (c) Simplified energy band diagram of the MoS_2-Au contact. Red, black, and blue curvature correspond to the behavior of back-gate voltages of -20V, 0V, and 20V, respectively.

The observed behavior of the heterojunction can primarily be explained by a simplified energy band diagram (full band diagram given in Figure 3.10) of the MoS_2 contact as shown in Figure 3.9c. When the MoS_2 channel is in the off-state (-20 V, the red band curvature in Figure 3.9c), there exists a sizeable Schottky barrier and depletion region located at the MoS_2-metal interface, which make it difficult for carriers to overcome the barrier and to be collected by the metal electrode, leading to a long carrier transit time. When the Fermi level of MoS_2 moves close to its conduction band, the band offset ($\phi_0 = E_c - E_F$) changes linearly with the back-gate voltage via $\delta\phi_0 = e\alpha V_G$: where E_c is the minimum of the MoS_2 conduction band, E_F is its Fermi energy, e is the electron charge, and α is a numerical constant that measures how effectively the gate voltage modulates the band energy. [118, 119] The shut-off gate voltage observed in the transfer characteristic of the MoS_2 channel is about -10 V, indicating that the Fermi level is close to the minimum of the MoS_2 conduction band under this gate voltage. [58, 120] On the other hand, when the Fermi level is very close to the conduction band of MoS_2 (0 V, the black band curvature in Figure 3.9c or 20 V, the blue band curvature in Figure 3.9c), the depletion width will become very narrow. As a result, the carriers can easily flow from MoS_2 to the metal electrode due to tunneling

through a narrow depletion region, leading to an ohmic-like contact. [67, 121]

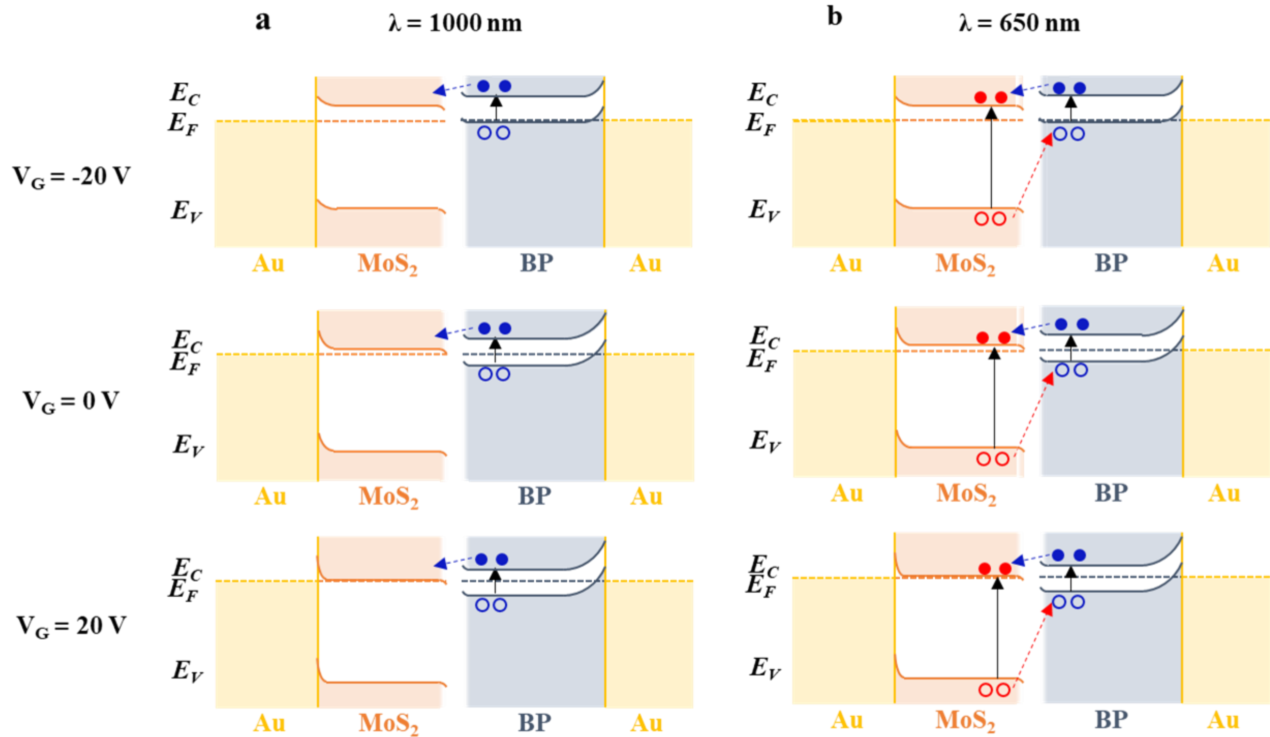

Figure 3.10 Band diagram of BP–MoS_2 Heterojunction . Band diagram for the BP-MoS_2 heterojunction under (a) 1000 nm and (b) 650 nm wavelength illumination. The band gap of BP is ~0.3 eV and the respective E_F - E_V is 0.1 eV. The band gap of the MoS_2 is ~1.9 eV and the respective $E_C – E_F$ is 0.2 eV. [83, 122]

Through further examining the complete band diagram under various gate voltage conditions, as diagrammed in Figure 3.10, the photocurrent generation and the wavelength dependence of the response time can more fully be understood. Under 1000 nm illumination, Figure 3.10a, the photocurrent signals are mainly attributed to the direct band gap transition in BP since the incident photons cannot provide sufficient energy to excite electrons in the MoS_2 from its valence band to its conduction band. Based on the polarity of photocurrent responses, it can be identified that photo-excited electrons in BP flow from BP to MoS_2 due to the conduction band offset at the BP-MoS_2 interface. [117] These photo-excited electrons will then pass through the MoS_2 channel to the metal electrode. When the MoS_2 channel changes from the on-state (20 V) to the off-state (-20 V) the depletion width at the MoS_2–metal interface increases and the Fermi level

moves away from the conduction band, making it more difficult for photo-excited electrons to overcome the interface barrier as well as defect/impurity-induced trapping states along the channel and thus leading to a long carrier transit time. Therefore, the photoresponse time increases when the MoS_2 channel is in the off-state since the carrier transit time is the key factor that limits the photoresponse time. [105] Similar results have been reported in MoS_2 phototransistors, where a large decrease in the photoresponse time was observed when the MoS_2 channel was turned on. [100, 107] Moreover, photons with a shorter wavelength and thus higher energy can transfer more energy to EHPs, leading to high energy photo-excited electrons with a higher probability to overcome the Schottky barrier at the MoS_2-metal interface and trapping states along the channel when the MoS_2 channel is in the off-state. [18] The subsequent flow of higher energy photo-excited electrons to the external circuit to generate the photocurrent has a shorter transit time and thus faster photoresponse time. However, when the MoS_2 channel is turned on photo-excited electrons can tunnel through the narrow depletion region; thus the photoresponse time does not depend on the energy of these photo-excited electrons (or the wavelength of the incident light).

Under 650 nm illumination, Figure 3.10b, the electrons in both BP and MoS_2 are able to be excited from their valence to conduction bands. Due to the Fermi level alignment of BP and MoS_2, the valence band maximum of BP is much higher than that of MoS_2; therefore, photo-excited holes in the valence band of MoS_2 can inject into the BP and then pass through the BP channel to the electrode resulting in strong photocurrent signals with the same polarity as those induced by the photo-excited electrons in BP. For photo-excited holes, the barrier at the BP-metal interface is expected to be negligible in comparison with that at the MoS_2-metal interface due to a much smaller band gap of BP, having a limited effect on the carrier transit time.

The relative lengthening of decay process of the BP-MoS_2 heterojunction is also considered.

As shown in Figure 3.9b, the decay time follows a similar gate- and wavelength-dependence as the rise time, but is slightly longer than the corresponding rise time when the MoS_2 channel is turned off. Here, the longer decay time is likely related to the defect/impurity trapping present at the MoS_2-metal interface and possibly along the MoS_2 and BP channels.[123] When the light is on, photo-excited carriers get trapped in these states. Once the light turns off, the photoresponse cannot fully vanish until the trapped carriers are released leading to a longer decay time. However, when the MoS_2 channel is in the on-state, the width of the Schottky barrier is significantly reduced and the trapping states in the channel are also filled by gate induced electrons. Consequently, the photo-excited electrons can tunnel through the narrow depletion region without filling the trapping states. Thus, there is no delay for the decay time under this circumstance. In this experiment, a decay time of 13 μs regardless of the incident laser wavelength has been achieved with a gate voltage of 20 V, which is several times faster than that of other BP-MoS_2 heterjunctions[96] as well as BP and MoS_2 based phototransistors.[18, 107, 124, 125] Here the rise and decay times are mainly limited by the sizable Schottky barriers at the MoS_2-metal interface. Carefully engineering the MoS_2-metal contact by adding heavily-doped TMDCs to generate extremely narrow depletion regions[21, 67] or using gated-graphene contact to achieve negligible Schottky barriers[126] may further improve the photoresponse time of BP-MoS_2 heterojunctions.

In this work, SPCM has been utilized to study the photoresponse time of BP-MoS_2 heterojunctions excited by incident light of wavelengths ranging from 650 nm to 1000 nm. It is found that the Schottky barrier at the MoS_2-metal interface is likely to play an important role in the rise and decay time of the heterojunction. A longer carrier transit time and thus a slow photoresponse speed is observed when the MoS_2 channel is turned off due to the sizeable Schottky barrier and depletion width that make it difficult for photo-excited carriers to overcome the barrier

at the MoS_2-metal interface. Moreover, these results have shown that the rise and decay time of the heterojunction increase with increasing incident laser wavelength under this condition. Here, photo-excited carriers induced by short wavelength photons possess higher energy, resulting in a higher probability to overcome the Schottky barrier at the MoS_2-metal and thus a relatively fast response time. While at longer wavelengths the lower energy incident photons are unable to overcome the barrier and thus have an even longer response time. On the other hand, when the MoS_2 channel is in the on-state, photo-excited carriers can tunnel through the narrow depletion region at the MoS_2-metal interface, leading to a short carrier transit time independent of the wavelength of the incident photon. A response time constant of 13 μs has been achieved in both rising and decaying regions regardless of the incident laser wavelength, which is comparable or better than those of other BP-MoS_2 heterojunctions as well as BP and MoS_2 based phototransistors. This work expands the understanding of photoresponse dynamics in 2D material heterojunctions and provides new insight into the engineering of the interfaces between 2D materials and metal electrodes to reduce their photoresponse times, opening a door for future high-speed electronic and optoelectronic applications.

3.3 $MoSe_2$ Based Heterojunctions

In addition to devices constructed out of two materials, the facile fabrication offered by heterojunctions extend far beyond this. Here collaborative work done with Christian D. Ornelas on an undoped $MoSe_2$ channel device with asymmetric heavily p-doped WSe_2 and MoS_2 contacts is briefly discussed. Due to the variability found in 2D device fabrication, this architecture offers the unique opportunity for direct comparison of different 2D material interfaces. Furthermore, a response speed of ~16 to ~18μs is observed representing a three order of magnitude improvement previous $MoSe_2$ channel devices. These devices were fabricated by Dr. Arthur Bowman and Dr. Kraig Andrews under the direction of Dr. Zhixian Zhou.

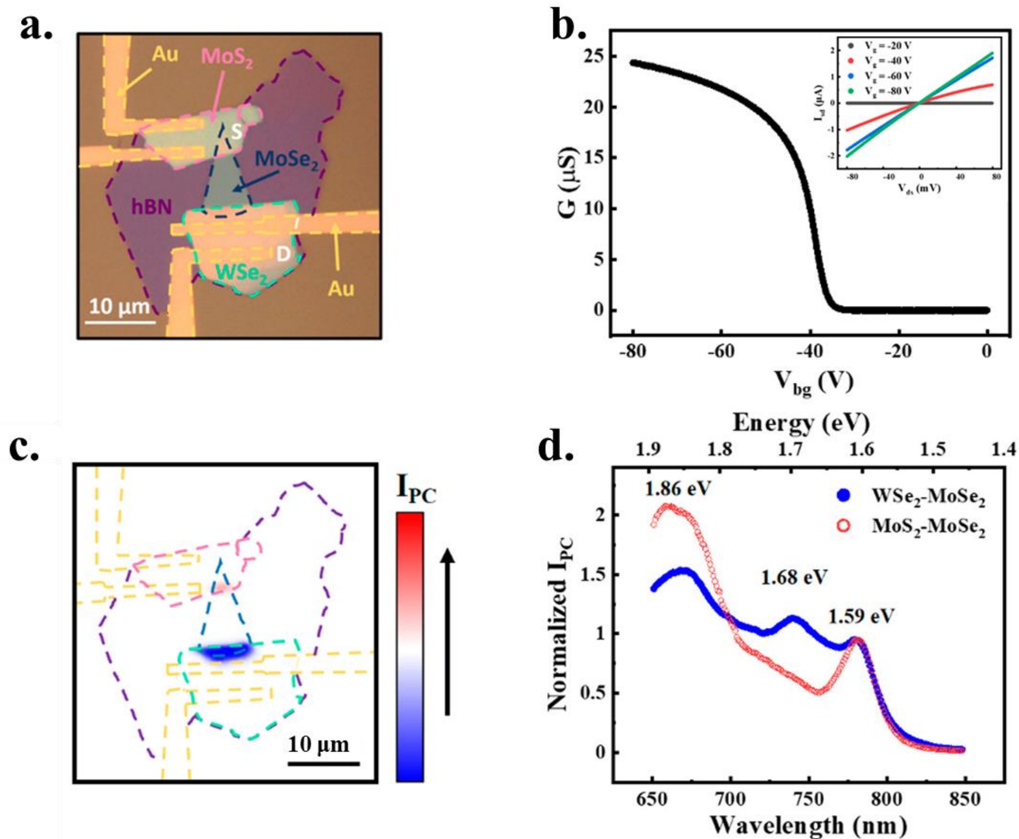

Figure 3.11 $MoSe_2$-Based Heterojunction (a) Optical micrograph outlining the constituent 2D materials. (b) Electrical transport properties of the device. Inset shows the linear ohmic nature of the device at different gate voltages (c) Representative photocurrent mapping of the device under -30mV bias and at 780nm wavelength illumination. (d) Wavelength dependence of the photocurrent response at their respective junctions.

An optical micrograph of a typical device is shown in Figure 3.11a. The thickness, obtained from AFM, of the hBN (dark purple), MoS2 (pink), $MoSe_2$ (dark blue), and WSe2 (cyan) are ~15 nm, ~23 nm, ~7 nm, and ~16 nm, respectively. A high field-effect mobility of ~260 $cm^2V^{-1}s^{-1}$ extracted using equation (6) from the linear portion of Figure 3.11b is found at 80K which is higher than previous reports.[127, 128] Electrical transport properties also reveal linear and symmetric behavior indicating ohmic behavior (Inset of Figure 3.11b). The modulation of lateral band alignment from the PVE is demonstrated through SPCM in Figure 3.11c shown by a representative scanning photocurrent image of the device under -30mV of drain-source bias. This is further shown in the tuning of the photocurrent response at the respective junctions shown in Figure 3.12a and 3.12b by modulating the drain-source voltage with power dependence. Additionally, the ability for heterostructures to demonstrate properties of their constituent materials is shown through wavelength dependent measurements shown normalized for comparison in Figure 3.11d. The shared peak at ~1.59 eV and ~1.86 eV is attributed to the A and B exciton of $MoSe_2$, respectively, while the distinct peak at ~1.68 eV is attributed to the A WSe_2.[129-131] Additionally, the relative strength of the MoS_2 side between 1.8 eV and 1.9 eV is likely a result of the corresponding A exciton in MoS_2 producing a meaningful contribution to the photocurrent response.[92] Finally, temporally resolved SPCM is shown in Figure 3.12c and 3.12d. Given the pronounced effect to activate and eliminate the photocurrent response at the different junctions as shown in Figure 3.12a and 3.12b, the temporal response is measured at 0 mV for the MoS_2-$MoSe_2$ junction and the WSe_2-$MoSe_2$. The improved electrical and optoelectronic activity in this device is attributed to the negligible contact resistance enabled at the 2D material interfaces via use of heavily doped 2D and a clean substrate in hBN material contact resulting in improved mobility and shortened photocurrent response speeds.

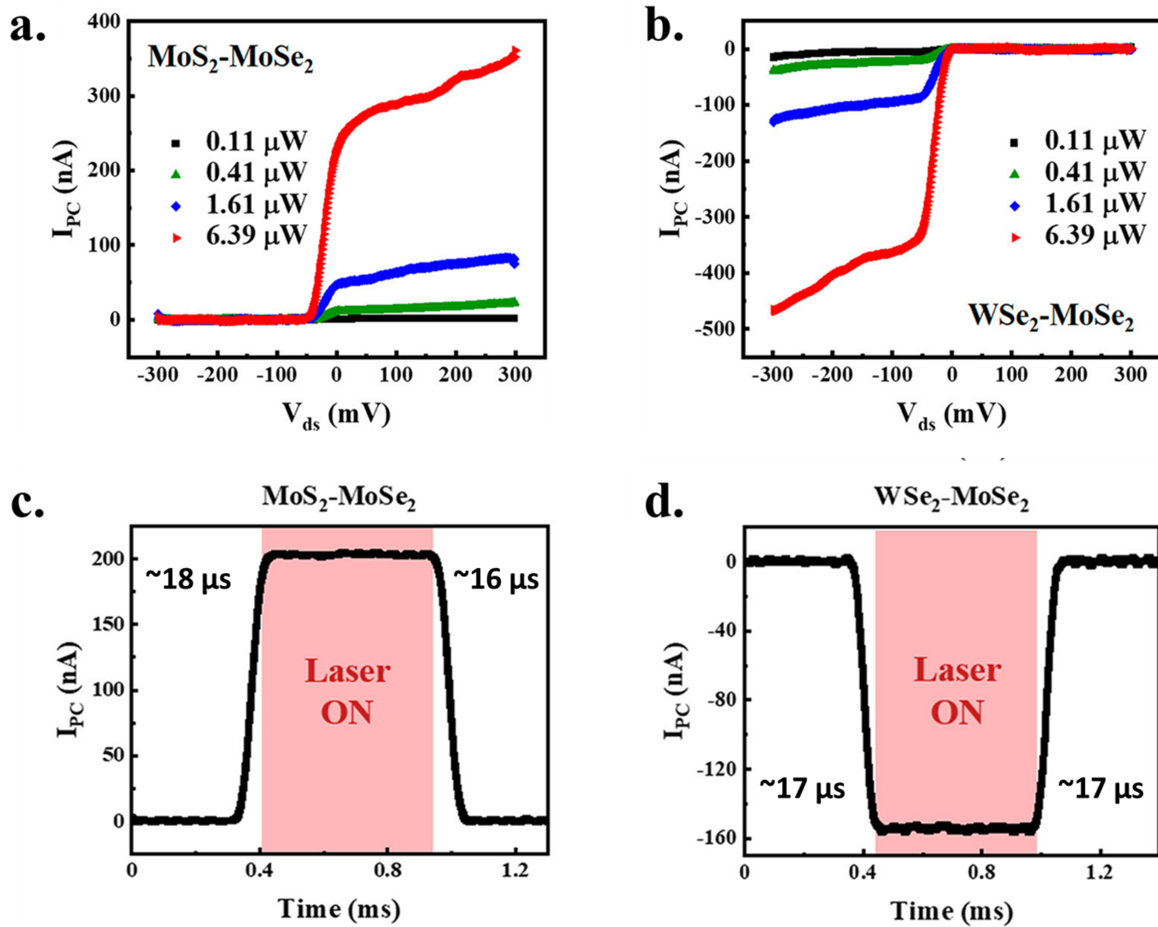

Figure 3.12 Bias and Time Dependent Photocurrent Response in $MoSe_2$ based Heterojunctions. Bias and power depdenet photocurrent itensity under 650nm wavelength illumination for the (a) MoS_2 and the (b) WSe_2 side of the $MoSe_2$ heterojunctions. Temporally resolved photocurrent measurements under 650nm wavelength illumination showing fast response times for both the (c) MoS_2, under 0 mV drain-source bias, and the (d) WSe_2, under -30 mV drain-source bias, side of the $MoSe_2$ heterojunctions.

Chapter 4 Charge Density Wave Materials for NIR Detection

4.1 Introduction to Charge Density Wave States and $TiSe_2$

Not only do the initial atomic composition and arrangement of a material profoundly impact their electrical and optoelectronic properties, the changing of phase will often times result in significantly different electrical behavior. Beyond the typical understanding of phases as states of matter, materials can also be classified in phases by their properties such as being metallic, insulating, or semiconducting or also by exotic phases such as being superconducting or permitting charge density wave (CDW) formation. A notable example of this in some group 6 2D TMDCs a transition from semiconducting in a 2H arrangement to metallic in a 1T arrangement occurs due to a change in the relative orientation of the X chalcogen layers in characteristic the X-M-X structure.[132] As evidenced by this, these changes primarily relate to the distribution and movement of charge such as in the formation of charge density waves. Charge density waves are the result of the electron charge density ground state becoming spatially modulated accompanied by a periodic distortion in the atomic lattice. This can easily be conceptualized in the 1D case as shown in figure 4.1. In the normal phase (Figure 4.1a) uniform atomic spacing with constant electron density is observed but in the CDW phase (Figure 4.1b) a more energetically favorable distorted lattice with a modulated electron density is present which alters the band structure. [133] CDW phases are also of interest since they often arise on the cooling down to superconducting phases. Additionally, CDW materials have been proposed for optoelectronic memory devices such as in $K_{0.3}MoO_3$ where the CDW phase can be manipulated with an external electric field and then destroyed with a laser or in 1T-TaS_2 where data can be encoded by a femtosecond laser in the amplitudes of CDW excitations.[134, 135] Furthermore, FETs with a conductance increase of 2 orders of magnitude are found in the CDW phase over the normal phase in $NbSe_3$ and TaS_3.[136]

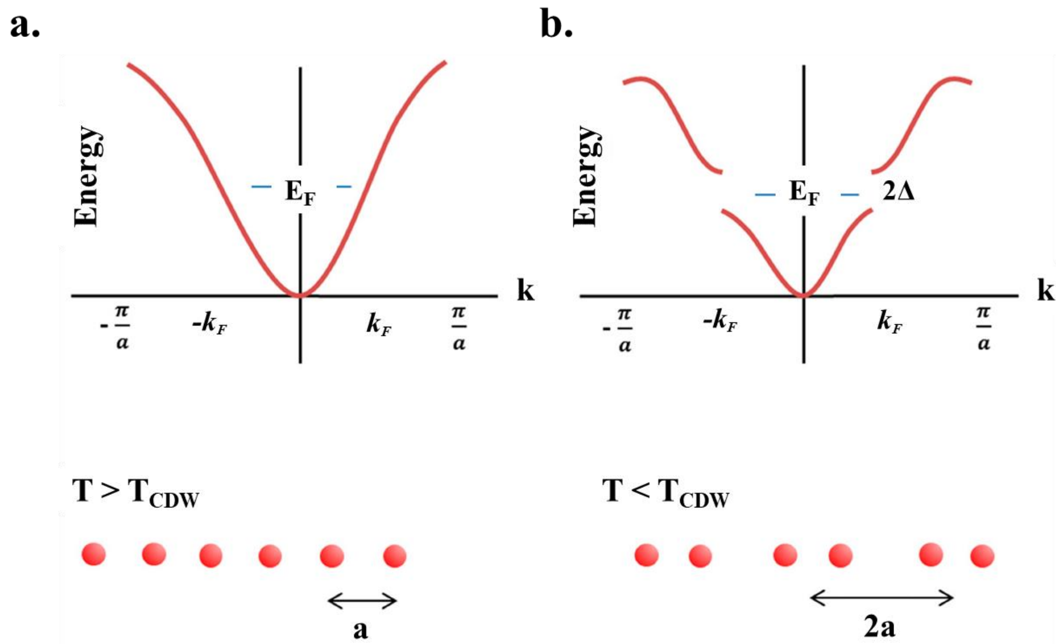

Figure 4.1 Energy Bands and Atomic Spacing for Normal and CDW State for a 1D crystal. Illustration for normal state (a) and CDW State (b) energy bands and atomic spacing for a 1D crystal (temperature above the transition temperature). Reproduced under (CC BY 4.0) from Ref [133].

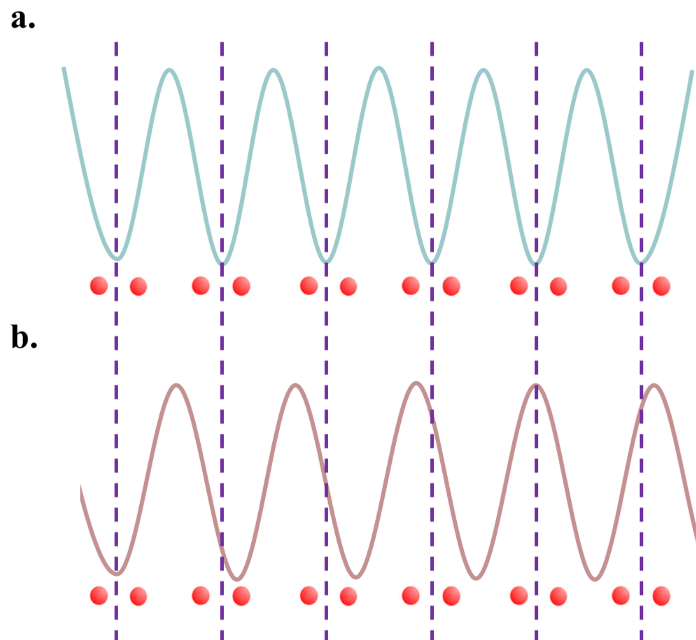

Figure 4.2 Illustration of commensurate and Incommensurate CDW. (a) Commensurate and (b) Incommensurate CDW states depeicted in 1D. Purple dashed lines indicate the increased atomic spacing arising from Figure 4.1b.

A variety of 2D TMDC materials have shown to possess superconducting as well as different CDW phases all occurring at a wide range transitions temperatures. Some of these CDW phases are commensurate (CCDW) meaning that they possess an integer multiple between the periodic distortion of the lattice and electron density. Others are incommensurate (ICDW) which clearly lack this trait. There are also some that nearly possess this trait and are referred to as nearly commensurate CDW phases (NCDW). The difference in theses transitions is illustrated in Figure 4.2. The nature of these transitions and their associated mechanisms is still subject to debate but it is clear that in 2D TMDCs the CDW and superconducting phases are interrelated.[133] A summary of these variations with their respective transition temperatures are summarized in Table 4.1.

Table 4.1 Summary of 2D TMDC CDW and Superconducting Phase Transitions.

Material	$T_{Superconductor}$	T_{CDW} (Type)	Ref.
2H-NbS_2	6 K	Likely None	[137]
2H-$NbSe_2$	7.2 K	35 K (CCDW)	[138]
1T-TaS_2	~50 K	~180 K (CCDW)	[139]
		350 K (NCDW)	
		550 K (ICDW)	
2H-$TaSe_2$	0.15 K	~120 K (NCDW)	[140-142]
1T-$TiSe_2$	< 3 K	190 – 240 K (CCDW)	[143, 144]
		~3 – 5 K (ICDW)	

From this table a chief advantage of the focus of this work, $TiSe_2$, is readily apparent: the CCDW transition temperature, T_{CDW}, is relatively near room temperature (with thickness dependence resulting in the observed range). This range is easily obtainable through practical liquid nitrogen cooling and increases the viability of it in device architectures. Though the transition temperature is clearly seen, the nature and mechanisms of the transition has been hotly debated since the first observation of the CDW phase in bulk 1T-$TiSe_2$ in the late 1970s.[145] Recently with the use of time-dependent density functional theory simulations the question has largely been resolved. As is evident in the ambiguity of the definition presented for the CDW state, it is not always clear whether the lattice distortions form the CDW (in accordance with the electron phonon coupling theory) or are merely a consequence of the CDW formation (in accordance with the dominance of excitonic pairing). These simulations resolved this question by probing an excited state thus decoupling the lattice distortions from the ground state and enabling the real time visualization of the transition. These results indicate that both mechanisms contribute with the CDW phase being initiated by excitonic binding and enhanced by electron phono coupling.[146] Additionally, the ICDW phase is believed to be a precursor and plays a prominent role in the observation of superconductivity in 1T-$TiSe_2$. A representative phase diagram drawn from a top-gated $TiSe_2$ FET device is shown in Figure 4.3.[143]

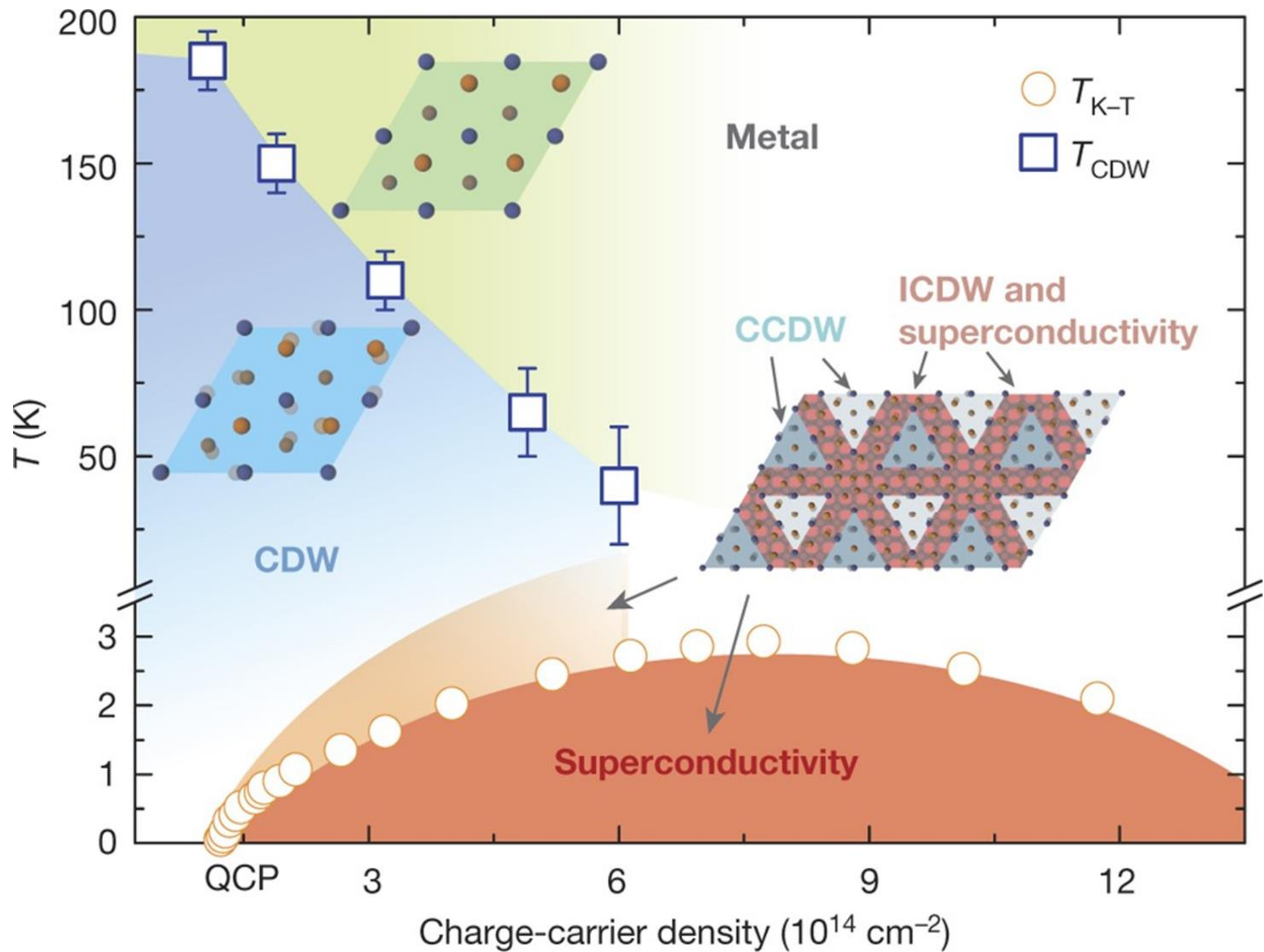

Figure 4.3 Phase Diagram for 1T-TiSe$_2$. The phase diagram created from measurements on hBN encapsulated thin (< 10nm) ion gel top gated TiSe$_2$ FETS. Reproduced with permission from Ref [143]. Copyright © 2016 Macmillan Publishers Limited.

4.2 TiSe$_2$-Metal Junctions

In continuing the search for an appropriate material for NIR photodetection from the library of 2D TMDCs one finds charge-density-wave (CDW) phases in TaSe$_2$ and TaS$_2$ which have recently been examined for their optoelectronic properties and demonstrated extremely fast, ultra-broadband, and ultra-high responses.[142, 147] Looking nearby from these group 5 TDMCs into the nearby group 4 TMDCs (M= Ti, Zr, Hf and X= S, Se, Te) one notices they have received relatively little attention in their single- or few-layer form even though they possess unique optical, electrical, optoelectronic, and thermoelectric properties.[148] Strong light absorption properties in

the visible to the infrared region as well as enhanced thermoelectric performance with high power factors have been show in TiS_2.[149, 150] An exceptionally high charge carrier mobility of ~2,000 $cm^2V^{-1}s^{-1}$ as well as a sheet current density up to 8000 μA μm^{-1} have been predicted for $ZrSe_2$.[151, 152] And the semiconducting $HfSe_2$ has a high predicted mobility of ~3,579 $cm^2V^{-1}s^-1$.[152] Furthermore, phototransistors fabricated out of $HfSe_2$ have shown strong responsivity in the visible to ultraviolet regimes in the range of hundreds of amperes per watts but with a slow response time on the order of milliseconds and only achieved under large gate voltages.[153] All these fundamental studies hold promise for the further exploration of the optoelectronic properties of group 4 materials, such as $TiSe_2$. Many investigations have examined the optical and electrical properties of few-layer $TiSe_2$, showing a relatively high CDW phase transition temperature, T_{CDW}, of ~200 K as well as the ability to precisely control this transition temperature using an electric field.[143, 145, 154-156] But, previous work on optoelectronic properties of $TiSe_2$ have been focused on either angle-resolved photoemission spectroscopy measurements that reveal detailed understandings of the CDW phase transition and associated band structure[157-160] or other work that explores the observation of spontaneous gyrotropic electronic order.[161] This encourages but leaves open the exploration of few-layer $TiSe_2$ optoelectronic devices.

4.2.1 Device Fabrication

Traditional semiconductor device fabrication procedures almost universally include metal deposition either in the form of thermal or electron beam deposition. To do this also the spinning and patterning of a photoresist is required. This process of creating metal connections to material samples is known as metallization and is commonly used in the study of 2D devices. And though the maturity of this process offers a facile way to metalize 2D materials and is unparalleled for mass production of semiconductor devices, it comes with several downsides. The metal deposition

process often induces chemical disorder, defects due to atom bombardment, and penetration into the semiconductor on the order of nanometers due to the decaying wave function of the metal; all damaging the crystal lattice of the 2D material, a schematic along with transmission electron microscopy (TEM) imaging showing the impact of this is displayed in Figure 4.4e through 4.4g.[162-164] The TEM imaging clearly reveals defects and damage to a MoS_2 flake as a result of the deposition process. The glassy layer is the result of the strong bonding between the outer sulfur layer and gold.[35] Furthermore, any residue left during the photoresist spinning and development procedures or heating during the baking of the photoresist can result in imperfections that limit the ability to achieve theoretically predicted results.[35]

A secondary concern in the fabrication of semimetal devices, such as graphene[165] and likely $TiSe_2$ as well, but the motivating factor for the work of Liu et al. in developing a gold transfer procedure is that it has been shown to nearly eliminate the Fermi Level pinning effect that plagues 2D TMDC as well as III-IV bulk semiconductors.[35, 166-169] The pristine nature of 2D material flakes with their dangling bond free surfaces that make them ideal for stacking are also likely able to remove Shockley-Tamm states, which contribute to Fermi Level pinning, states that arise at the surface of bulk semiconductors.[170, 171] Additionally, the transfer method offers a much gentler metallization that doesn't require photolithography or deposition processes directly on the 2D material eliminating the defects, diffusion, and disorder introduced during traditional metallization. A schematic of this is offered in in Figure 4.4a and 4.4b. This results in atomically clean and distinct interfaces, as shown via TEM imaging in Figure 4.4c. The direct physical contact without adulterating the 2D material sample is also believed to greatly alleviate the gap states responsible for Fermi Level pinning.[35, 172-174] The ultimate summary of the difference in the bonding between the gold and 2D material flake is can be seen when comparing the results from

when the gold is mechanically peeled[175] off as shown in Figure 4.4d (transferred gold) and 4.4h (deposited gold). This difference highlights the van-der Waals bonding that takes place for the transferred gold.[35]

Additionally, this technique is ideally suited for multi-layer 2D material device fabrication as the metallization process provides the stamp that is required to transfer and stack different 2D materials.[171] This has been demonstrated in our lab recently through the stacking of nanowires.[176] The incorporation of metallization into the assembly procedure for heterostructures could also expedite device fabrication by eliminating a time intensive EBL or photolithography step in the fabrication process.

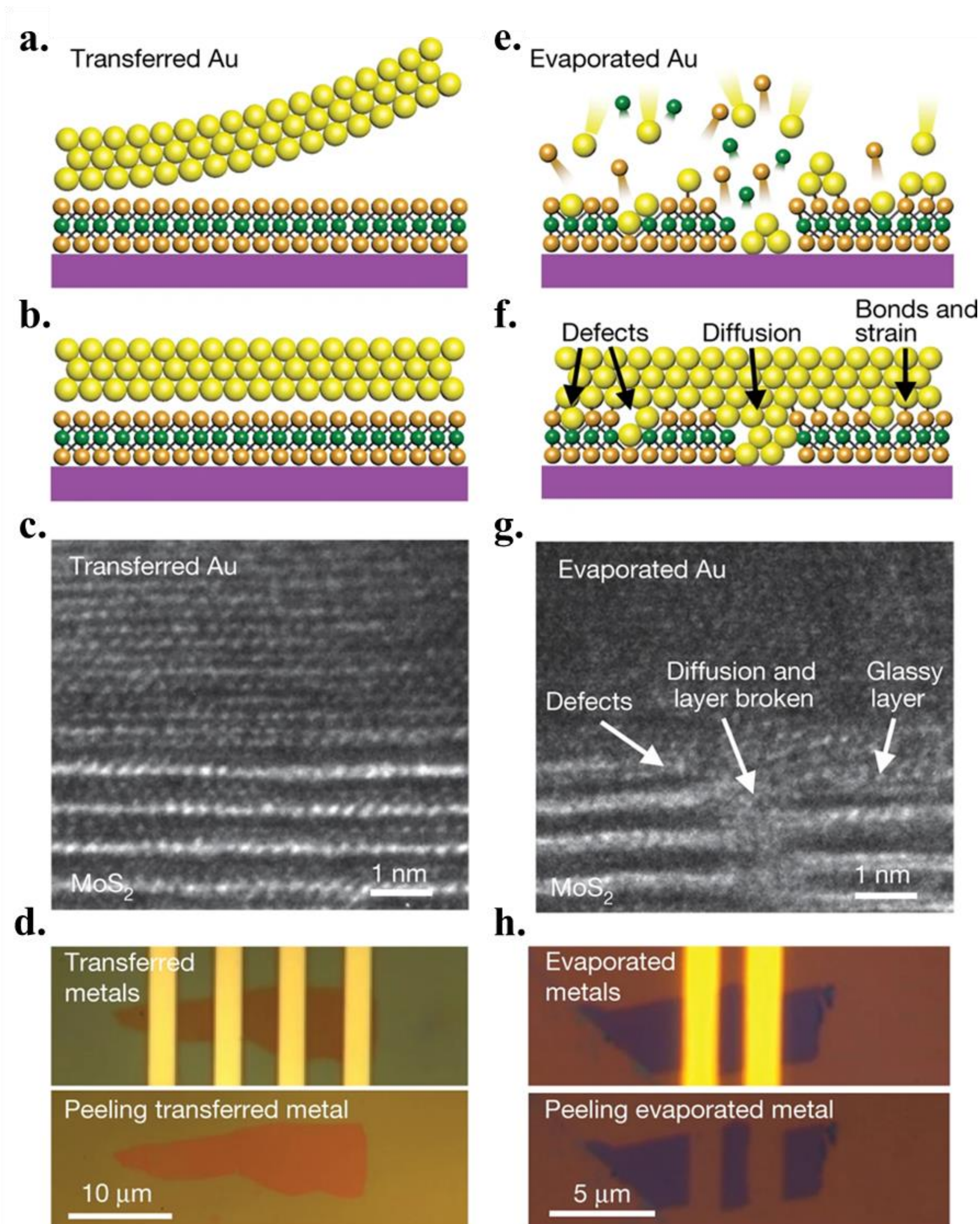

Figure 4.4 Comparison of Transferred and Deposited Gold on 2D Materials. (a) – (c) Cross-sectional schematics and TEM images of transferred Au electrodes on top of MoS_2. (d) Optical image of the MoS_2 device with transferred electrodes (upper) and with the transferred electrodes mechanically released (lower). (e) – (g), Cross-sectional schematics and TEM images of conventional electron-beam-deposited Au electrodes on top of MoS_2. (h), Optical image of a MoS_2 flake with deposited electrodes (upper) and with the deposited electrodes mechanical released (lower). Image (a), (b), (c), (d), (e), (f), (g), and (h) reprinted with permission from Ref [35]. Copyright © 2018, Macmillan Publishers Ltd., part of Springer Nature.

In this work a similar gold transfer procedure is implemented as diagrammed in Figure 4.5. Gold electrodes were prepared on a silicon wafer using a standard photolithography and thermal gold deposition procedure and diced into transfer sized pieces. (Figure 4.5a) They were then treated with hexamethyldisilazane (HMDS) to functionalize the silicon wafer to enable weak adhesion with the subsequently coated PMMA layer. (Figure 4.5b) Without the HMDS treatment the gold electrodes/PMMA cannot be easily nor wholly removed with a polydimethylsiloxane (PMDS) stamp. This electrode preparation procedure is described in detail in appendix A.2. High quality $TiSe_2$ flakes (purchased from 2D semiconductors) were mechanically exfoliated onto degenerately doped doped SiO_2/Si (285nm thermally grown oxide layer) substrates using the standard scotch tape method (Figure 4.5d).[3] To ensure a clean substrate for the high quality $TiSe_2$ flakes, substrates were nanostrip cleaned via the procedure described in appendix A.3. The gold electrodes/PMMA are peeled off the sacrificial silicon substrate (Figure 4.5c) with a PDMS stamp, aligned with the $TiSe_2$ flake using a custom stage, and then the stage is gently heated and the PDMS stamp is slowly removed. (Figure 4.5e) Finally, electron beam lithography is performed to open gold contact pads for wire bonding.

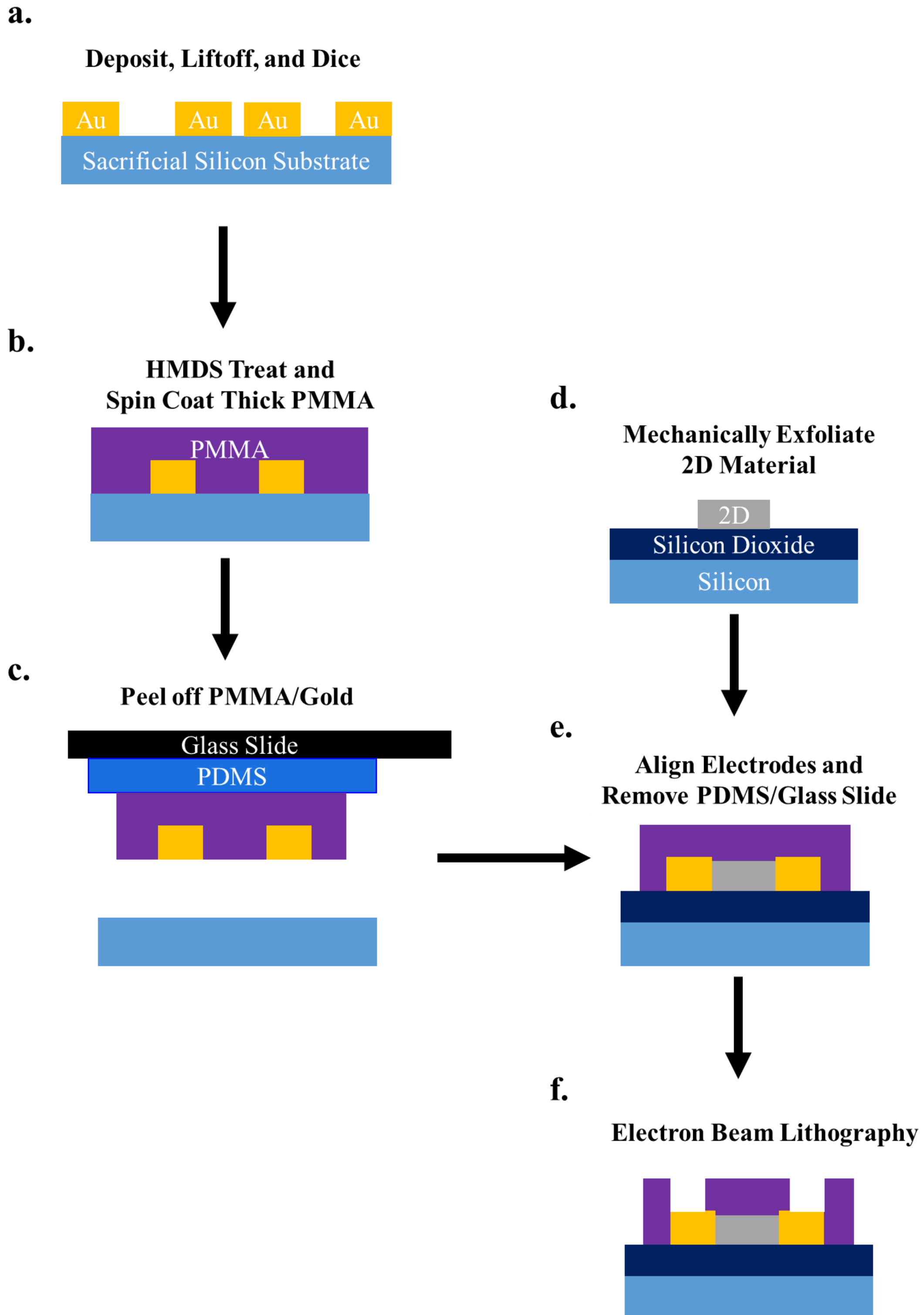

Figure 4.5 Schematic of the Gold Transfer Procedure The preparation of the electrodes is shown in (a) and (b). (d) and (c) are the two steps that culmniate in the device fabrication shown in (e). The final step that is required to enable wire bonding to the device is shown in (f).

To demonstrate the ability to execute this procedure, graphene devices were fabricated and basic electrical and optoelectronic characterizations were carried out. Few layer graphene flakes were mechanically exfoliated from highly oriented pyrolytic graphite (HOPG) onto degenerately p-doped SiO_2/Si substrates (285nm oxide layer) via the scotch tape method.[3] The transfer metallization procedure was completed and the as fabricated graphene device is shown in figure 4.6a. The scale bar is 5 μm. Electrical transport properties of the device were assessed by performing gate and drain-source bias dependent measurements. The characteristic [177, 178] V-shaped conductance curve of graphene indicating ambipolar charge transport with a charge neutrality point of ~32 V is shown in figure 4.6b. Calculated mobility for the hole (< ~32V) and electron (> ~32V) transport regions are 310 $cm^2V^{-1}s^{-1}$and 131, $cm^2V^{-1}s^{-}1$, respectively. Strong linear current response is observed when sweeping the drain-source bias of the device from -10 mV to 10 mV indicating ohmic contacts shown in the inset of figure 4.6b. Scanning photocurrent imaging under 1064nm wavelength illumination and power of 545μW is shown in figure 4.6c. The scale bar is 5 μm. Reflection imaging (not shown) taken simultaneously is used to determine the location of the few-layer graphene that has strong photocurrent signal as well as the electrodes, outlined in purple and gray, respectively. The x location of the laser was fixed at the dashed black line from figure 4.6c and the gate is swept from 0V to 60V to produce the position and gate dependent photocurrent image shown in figure 4.6d. The y axis indicates the position and the x axis is the gate voltage. The scale bar is 5 μm in the y direction and 5V in the x direction. Band bending as a result of the application of gate voltage is responsible for the change in polarity of the photocurrent response similar to what is seen in the above work regarding $PdSe_2$ phototransistors.[179]

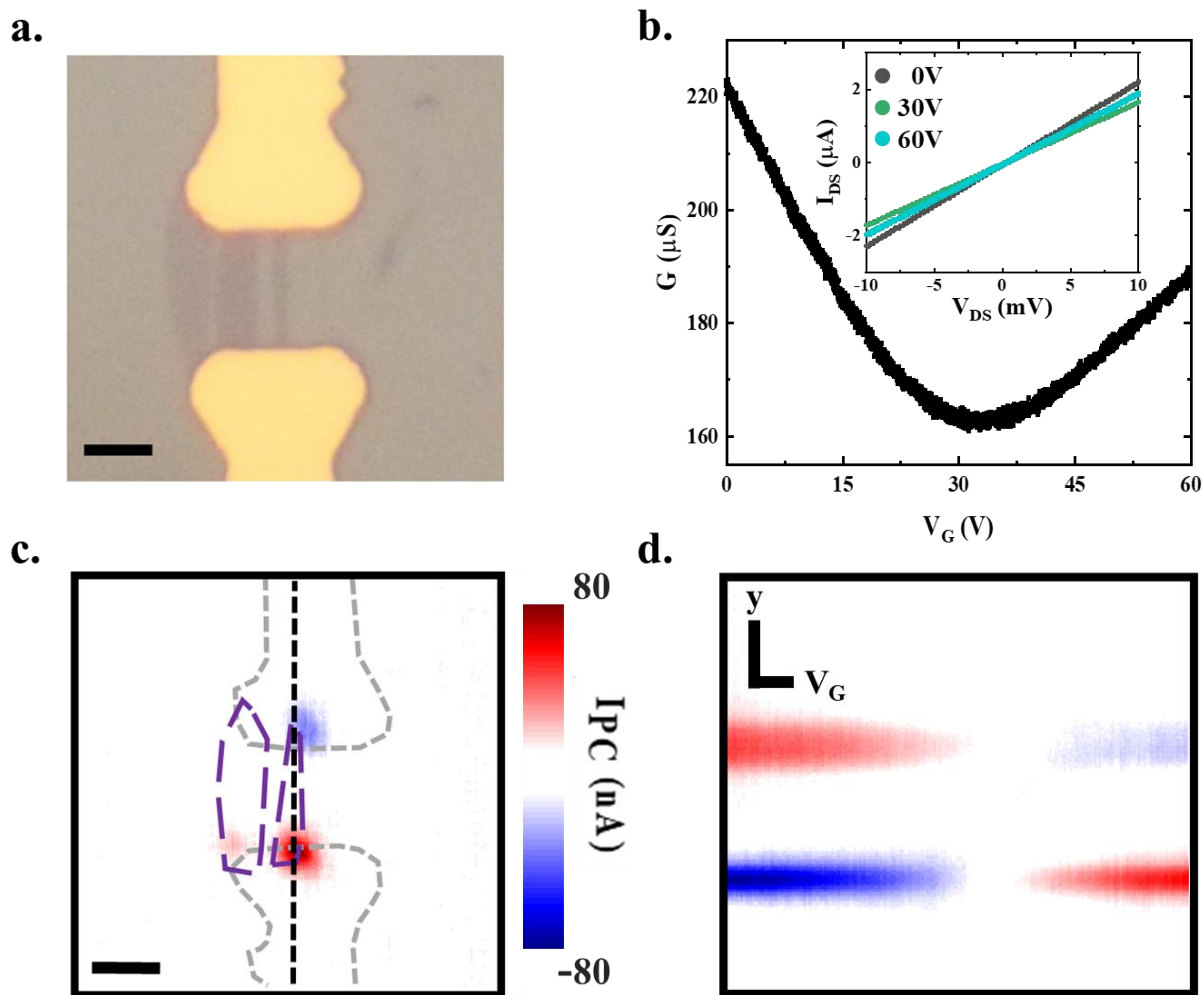

Figure 4.6 Basic Electrical and Optolectroinc Characterization of Gold Transferred Graphene FETs. Fabrication of graphene FET using the gold transfer procedure. (a) Optical image of the finished device. Scale bar is 5 μm. (b) Gate and (inset of b) drain-source bias electrical transport behavior of the device. Scanning photocurent imaging of the device with the electrodes outlined in gray and the few-layer graphene outlined in purple. Scale bar is 5 μm. (d) Gate depdent scanning photocurrent image taken with x fixed, shown as the dashed line in (c), showing the change in polarity of the photocurrent response as the bands are modulated by the back gate voltage. Y-axis is postion and x-axis is back gate voltage with scale bars of 5 μm and 5V, respectively.

4.2.2 Results and Discussion

Here few-layer $TiSe_2$-metal junctions are fabricated using the previously described gold transfer technique and their electrical and optoelectronic properties are subsequently explored via

scanning photocurrent microscopy. Strong photocurrent responses have been observed at the $TiSe_2$-metal junctions under 650 nm and 1064 nm illumination, respectively. Further studies have revealed that both the photovoltaic effect (PVE) and the photothermoelectric effect (PTE) contribute to the photocurrent generation. At 145 K, the photoresponsivities are 4.8 mA/W and 1.4 mA/W for 650 nm and 1064 nm illumination, respectively. Moreover, temporally resolved scanning photocurrent measurements demonstrate that rise and decay time constants are 31 μs and 32 μs, respectively, which are two orders of magnitude better than $HfSe_2$ based devices.[153] More importantly, it is found that the response times are two times slower when the temperature increases to 225 K. Additionally, there is up to an order of magnitude of reduction for the photocurrent responsivity at room temperature. The significant temperature-induced changes are likely attributed to dramatic reduction in carrier scattering that occurs when $TiSe_2$ is changed from the normal to CDW phases at T_{CDW} (~ 206 K). These results signify the depth and breadth of knowledge gained from continually exploring and assessing 2D materials for optoelectronic devices and advance the understanding of group 4 TMDCs. Furthermore, this work sheds light on the critical aspects of 2D material-metal junctions for engineering future temperature-dependent fast optoelectronic devices.

A schematic of a typical $TiSe_2$ device used in the experiments is presented in Figure 4.7a. These devices were prepared via mechanically exfoliating $TiSe_2$ from a bulk crystal onto degenerately doped SiO_2/Si substrates using the standard scotch tape method.[3] Sample thicknesses were characterized using a Bruker Dimension Icon Atomic Force Microscope and a standard optical contrast comparison imaging procedure, ranging from ~20 nm to ~49 nm.[180, 181] Finished devices were mounted in a chip carrier and wire bound. The inset of Figure 4.7b shows a $TiSe_2$ device with a thickness of ~31 nm. Temperature-dependent electrical resistance

measurements were further performed to characterize and assess device performance. A broad resistance peak centered at ~180 K is observed (black in Figure 4.7b), consistent with previous electrical transport investigations of $TiSe_2$.[143, 145, 182, 183] This anomalous resistivity peak is attributed to a crossover between a low temperature regime where electron-like carriers dominate the conductivity to a high temperature regime where thermally activated hole-like carriers dominate.[184] Additionally, a ratio for R_{max}/R_{300} of ~1.3 is observed that is comparable to molecular-beam epitaxy grown $TiSe_2$ thin films,[183] indicating the high quality of the mechanically exfoliated $TiSe_2$ flakes. To determine the CDW phase transition temperature (T_{CDW}) in $TiSe_2$, the derivative with respect to temperature of the resistance-temperature graph is calculated (red in Figure 4.7b) and the local minimum is found as ~206 K (T_{CDW}), which is consistent with previous reports.[143, 145, 182, 183]

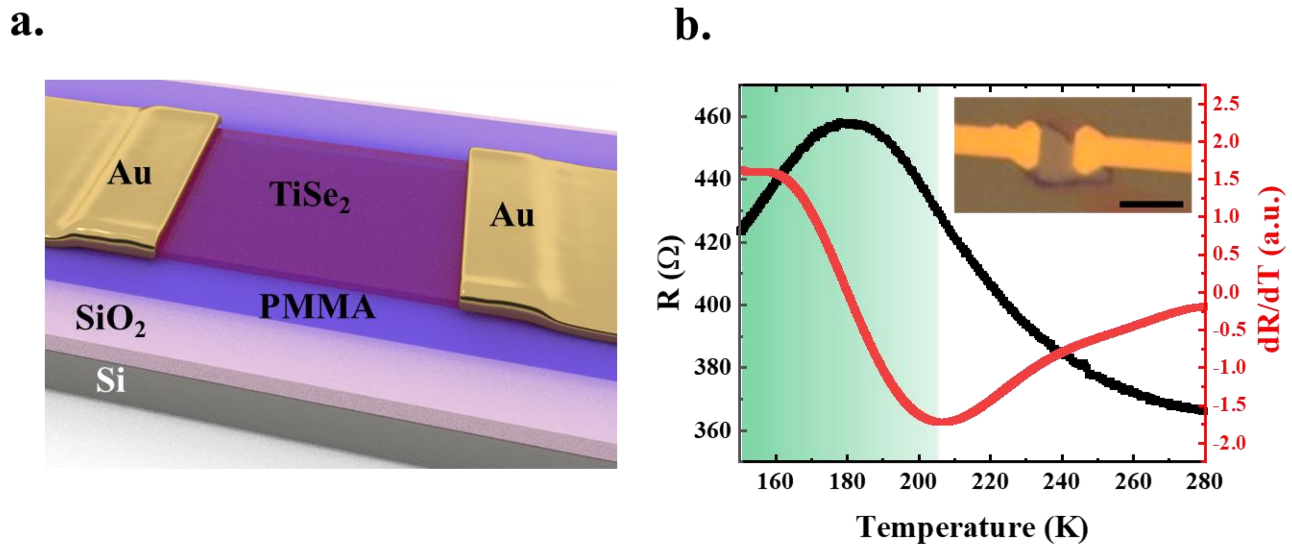

Figure 4.7 Electrical Transport in few-layer 1T-$TiSe_2$. (a) A schematic illustrating the layout of a $TiSe_2$ device. (b) Temperature-dependent resistance measurements show the characteristic resistivity peak (black). A broad maximum is noted at ~180K. A ratio for R_{max}/R_{300} of ~1.3 is observed, indicating the high quality of the mechanically exfoliated $TiSe_2$. The first derivative of the temperature-dependent resistance with respect to temperature is shown in red. The minimum of this curve, ~206 K, corresponds to the CDW phase transition temperature. The green background represents the CDW phase. Inset in (c) is an optical micrograph of a $TiSe_2$ device. The scale bar is 10 μm.

Raman spectroscopy was also used to identify the quality of $TiSe_2$ flakes. Raman measurements were carried out in the VINSE analytical core using the Thermo Scientific DXR Raman 532nm microscope. As shown in Figure 4.8a two dominant peaks are located at ~134 cm^{-1} and ~197 cm^{-1}, respectively, corresponding to the in plane (E_g) and out of plane (A_{1g}) vibrational modes of the Se atoms in $TiSe_2$, respectively.[154-156] These vibrational modes are depicted in Figure 4.8b with the Ti atoms in teal and the Se atoms in gold. [156] No significant difference was noted in these peaks based on the sample thicknesses used. A weak peak is also seen at ~305 cm^{-1}, likely resulting from acoustic phonons in the underlying silicon substrate and potentially the combination of the two different dominant modes.[154, 185, 186] Moreover, the absence of additional peaks indicates the pristine nature of the sample as it is common for peaks to arise during the oxidation process associated with trigonal (~253 cm^{-1}) and amorphous (~233 cm^{-1}) selenium that replace the dominance of the aforementioned active Raman modes.[182, 187, 188]

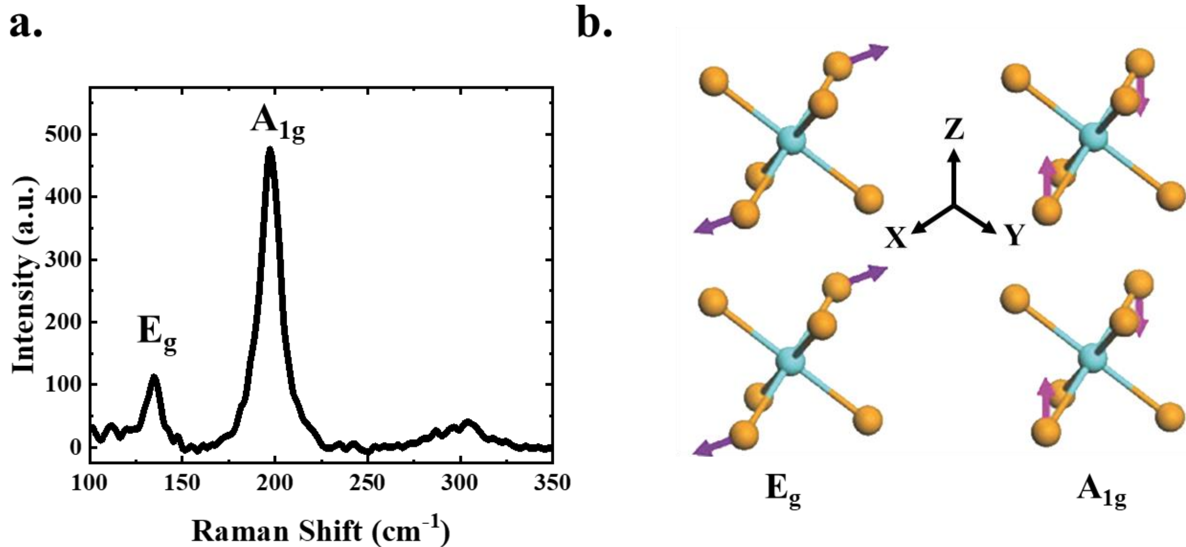

Figure 4.8 Raman Spectroscopy of few-layer 1T-$TiSe_2$. (a) Raman spectrum of a typical few-layer $TiSe_2$ flake at room temperature. Two strong peaks are seen at ~134 cm^{-1} and ~197 cm^{-1}, respectively, which match well with predicted E_g and A_{1g} optical phonon modes. A weak peak is observed at ~305 cm^{-1}, which may result from the overlap of the two phonon processes or as a remnant of the silicon substrate. (b) Illustration of the E_g and A_{1g} crystal lattice vibrations in $TiSe_2$. Reprinted with permission from Ref [156]. Copyright © 2018 John Wiley and Sons.

To explore optoelectronic properties of $TiSe_2$ SPCM was employed.[189] As shown in

Figures 4.9a and 4.10a, remarkable photocurrent responses were observed under 1064 nm and 650 nm illumination, respectively. The corresponding reflection images (Figures 4.9b and 4.10b) that were recorded simultaneously could be used to locate the positions of photocurrent signals. The electrodes are outlined in gray dashed lines, with D and S representing the drain and source contacts, respectively. The $TiSe_2$ flakes are outlined in purple. Strong photocurrent signals, I_{PC}, are observed at the $TiSe_2$-metal junctions. This is likely due to the Fermi level alignment at the junctions which leads to built-in electric fields that can efficiently separate photo-excited electron-hole pairs (EHPs) to generate photocurrent signals as show in the inset of Figure 4.9a. This suggests that the PVE plays an important role in the photocurrent generation at $TiSe_2$-metal junctions.[27] When the laser scans across the drain (source) contact, photo-excited EHPs are separated, generating a negative (positive) photocurrent due to the larger work function of the $TiSe_2$ flake relative to gold contacts that produces downward band bending.[173] To further clarify the photocurrent generation mechanisms present in the $TiSe_2$-metal junction, line profiles of photocurrent intensity under 1064 nm illumination are extracted across the junctions at 145 K and 280 K (Figures 4.9c and 4.9d), respectively, where the photocurrent intensities were normalized for clarity. By comparing the photocurrent profiles with the Gaussian fittings (solid red curves), a strong photocurrent "tail" in the gold electrode region is noticed for the environmental temperature below the T_{CDW} as indicated by the blue arrows, suggesting that the PTE also contributes to the photocurrent generation at the junction for $TiSe_2$ in CDW phase.[14, 29] This is consistent with previous reports that $TiSe_2$ possesses a high thermoelectric power below T_{CDW},[190-192] inducing heat gradients at the $TiSe_2$-metal junction and thus giving rise to a thermoelectric current.[193] This was also done for 650nm illumination (Figures 4.10c and 4.10d), where similar results were found.

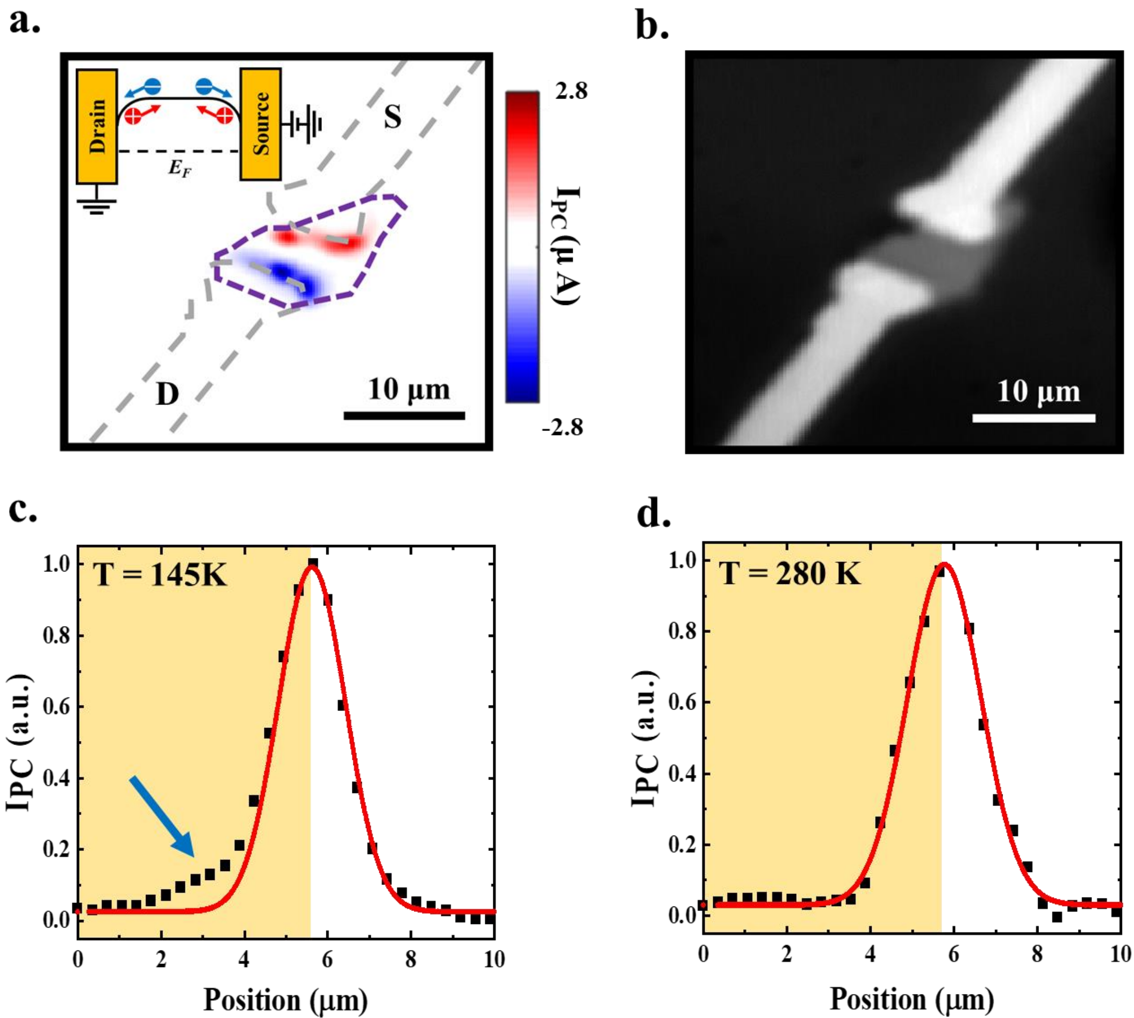

Figure 4.9 SPCM of $TiSe_2$ Metal Junctions under 1064 nm illumination. (a) Spatially resolved photocurrent and (b) reflection images of the device at 145 K show strong photocurrent responses under 1064nm wavelength excitation of ~1.86 mW at $TiSe_2$-metal junctions. The power of the 1064 nm laser is ~1.86 mW. The inset of (a) shows a circuit diagram of the $TiSe_2$ device depicting the current direction for the respective laser scanning locations. The laser scan across the drain (source) contact, resulting in the observed negative (positive) photocurrent signals. Photocurrent responses across the $TiSe_2$-metal junctions at (c) 145 K and (d) 280 K, respectively. The black dots and red solid curves are experimental data and the related Gaussian fittings, respectively. The photocurrent "tail" on the electrode is highlighted by the blue arrow. The yellow backgrounds represent the positions of the electrodes.

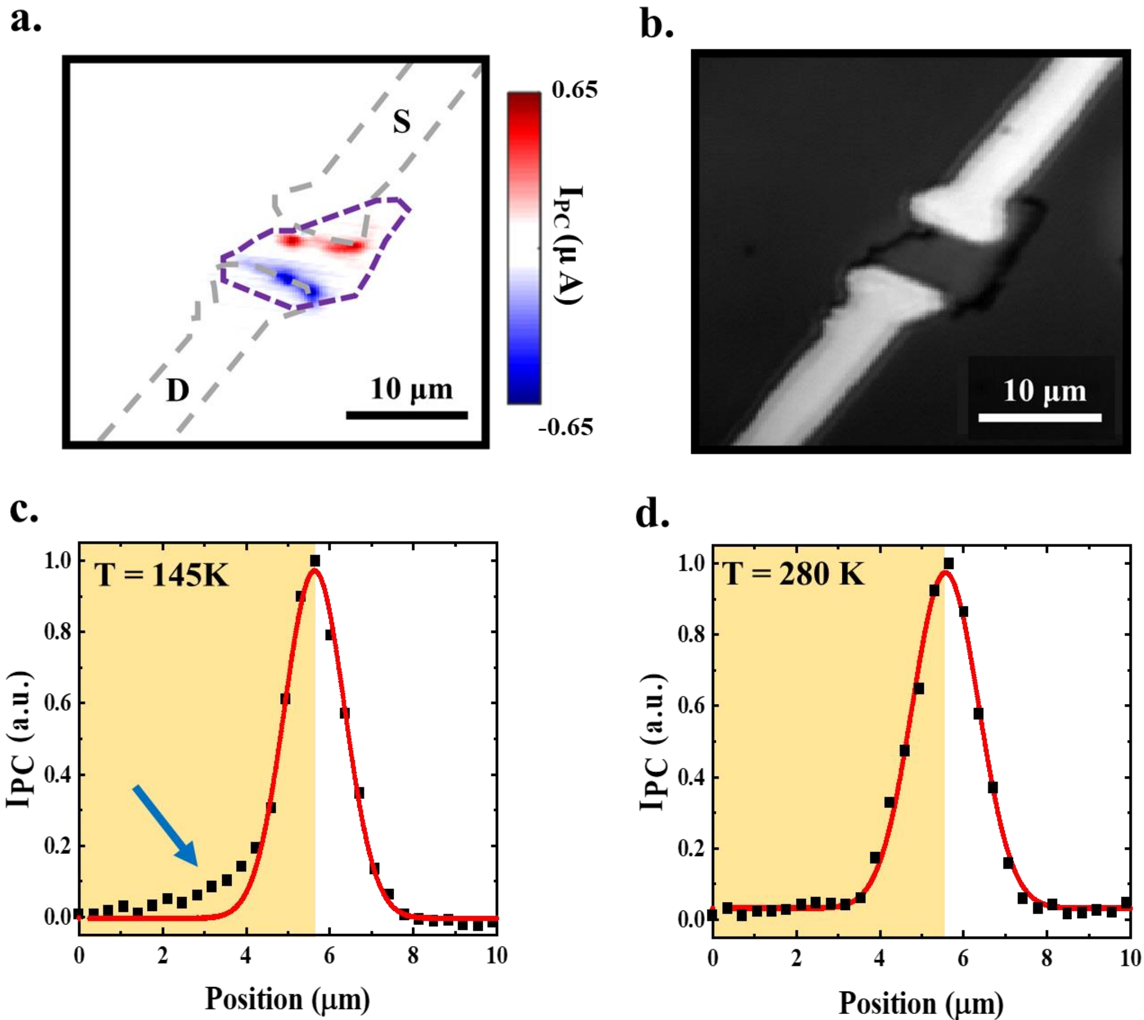

Figure 4.10 SPCM of $TiSe_2$ Metal Junctions under 650 nm illumination. (a) Spatially resolved photocurrent and (b) reflection images of the device at 145 K show strong photocurrent responses at $TiSe_2$-metal junctions. The power of the 650 nm laser is ~0.14 mW. The inset of (a) shows a circuit diagram of the $TiSe_2$ device depicting the current direction for the respective laser scanning locations. The laser scan across the drain (source) contact, resulting in the observed negative (positive) photocurrent signals. Photocurrent responses across the $TiSe_2$-metal junctions at (c) 145 K and (d) 280 K, respectively. The black dots and red solid curves are experimental data and the related Gaussian fittings, respectively. The photocurrent "tail" on the electrode is highlighted by the blue arrow. The yellow backgrounds represent the positions of the electrodes.

Power dependent measurements were also carried out for both 650nm and 1065nm wavelength illumination. A linear relationship was observed for both at 145K, as shown in Figure 4.11a. This linear trend is expected as the increased number of incident photons from a higher power results in an increased generation of EHPs. Furthermore, high power excitations were further carried out for 1064nm continuing to show this linear trend on a log-log scale ($I_{PC} \propto P^{1.01}$), as shown in Figure 4.11b. This high power characterization results in almost a perfectly linear relationship. This is notable as this is absent among common TMDCs such as MoS_2 and WSe_2 [194, 195] as well as in graphene devices. [196, 197] The absence of saturation at these large powers as it likely indicates the absence of trap states and the potential to be explored as a high power photodetector. [115, 116]

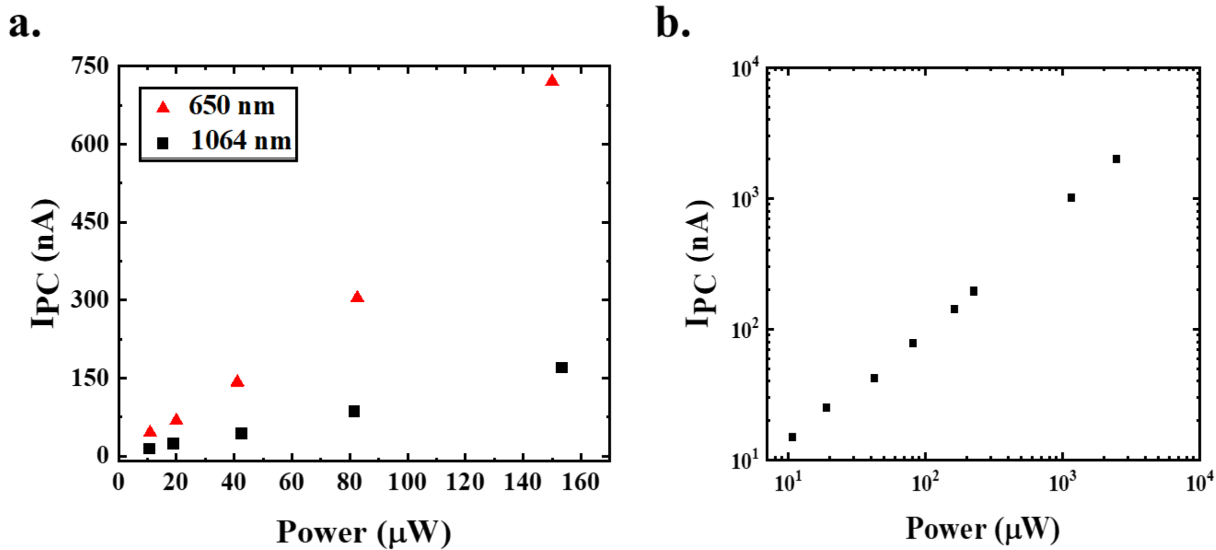

Figure 4.11 Power Dependence of $TiSe_2$-Metal Junctions (a) Power dependent measurements for 650nm (red triangles) and 1064nm (black squares) laser illumination. (b) High power 1064nm laser illumination.

The photoresponse dynamics were also examined through temporally resolved scanning photocurrent measurements for both above and below T_{CDW}. In these experiments, the addition of an optical chopper to the light path allowed for the application of ON/OFF light modulation while

photocurrent signals were recorded as a function of time. Two cycles of a typical temporal response under 1064 nm illumination at 145 K for the $TiSe_2$ device is shown in Figure 4.12a. The device maintained consistency in its optoelectronic performance over thousands of cycles demonstrating its reliability. Using a single exponential function to fit the rise and decay portions of the time response curve, rise and decay time constants are found for both above and below the CDW phase transition temperatures. The photoresponse times are significantly reduced upon cooling to T_{CDW}. To further examine this difference snapshots of the rise and decay curves are shown in Figure 4.12b and 4.12c, respectively.

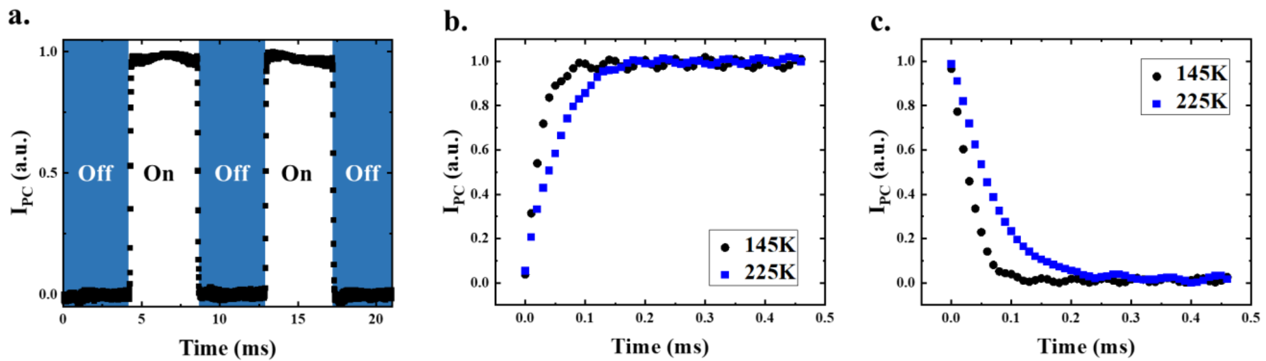

Figure 4.12 Improved Photoresponse Dynamics in the CDW phase of 1T-$TiSe_2$ (a) Representative sample of the temporal photocurrent response under 1064nm illumination and below the T_{CDW} at 145K. Snapshots of the rising (b) and decaying (c) portions of the temporal photocurrent response below the T_{CDW} at 145K (in black circles) and above the T_{CDW} at 225k (in blue squares).

At 225 K (above T_{CDW}), rise and decay time constants are 60 μs and 66 μs, respectively. Moreover, rise and decay time constants of 31 μs and 32 μs are achieved at 145 K (below T_{CDW}), which are as twice fast as those above T_{CDW}, two orders of magnitude better than $HfSe_2$ based devices.[153] Further temperature dependent characterizations were performed, as shown in Figure 4.8a, from 145K up to 240K, showing roughly a stepwise change in the photocurrent rise and decay times. The greatly improved response times below the CDW phase transition temperature is likely attributed to dramatic reduction in carrier scattering that occurs as a result of

the switching between the normal and CDW phases of $TiSe_2$.[198] It is well-known that two important factors that limit the response time of a device are RC time constant and carrier transit time.[70] For $TiSe_2$ in CDW phase, the reduction in carrier scattering results in short carrier transit time, leading to fast photocurrent response. To determine the exact nature of these interactions further focus on the photodynamic response of $TiSe_2$ is warranted.

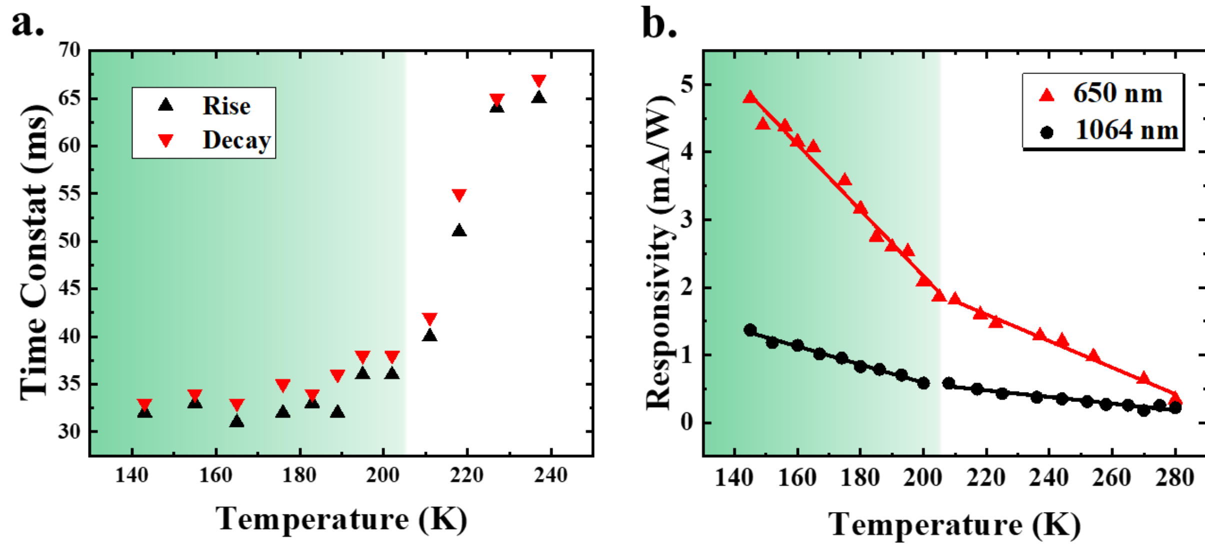

Figure 4.13 Improved responsivity and response time in the CDW phase of 1T-$TiSe_2$. (a) Temperature dependent response time constants showing the step-wise increase in response time above the T_{CDW}. Rise and decay time constants are indicated by black and red triangles, respectively. (b) Temperature dependent responsivity measurements under 650nm (red triangles) and 1064nm illumination showing the doubling of the rate of change in responsivity with respect to temperature below the T_{CDW}. The green background in (a) and (b) indicates the CDW phase.

Next how the CDW phase transition influences the responsivity of $TiSe_2$-metal junctions under laser illumination is explored (Figure 4.13b). Here, the laser beam with a diffraction limit about 1 μm has been locally focused at the $TiSe_2$-metal interfaces, which is different from some studies that the beam sizes are larger than the devices.[142, 199, 200] Positive and negative photocurrent signals are found at source and drain regions, respectively, in which the positive response has been used to analyze the responsivity in Figure 4.13b. Experimental results reveal a

significant enhancement in the responsivity of the devices under cooling and a doubling of the rate of photocurrent increase below T_{CDW}. Maximum responsivities at 145 K have been achieved to be 4.8 mA/W under 650 nm illumination and 1.4 mA/W under 1064 nm illumination, respectively, up to an order of magnitude higher than those obtained at room temperature. The relatively small responsivity of $TiSe_2$ under 1064 nm illumination is likely attributed to the lower optical absorption for 1064 nm excitation than that for 650 nm excitation.[201] This further suggests that in the CDW phase, the carrier scattering reduction leads to short carrier transit time,[198, 202] improving the collection of photoexcited EHPs and thus enhancing the photocurrent generation efficiency.

In this chapter, systematic investigation of the electrical and optoelectronic properties of few-layer $TiSe_2$-metal junctions is conducted. Remarkable photocurrent responses have been detected at the $TiSe_2$-metal junctions, likely resulting from both the PVE and the PTE. A fast response time approaching to 31 μs has been achieved, which are two orders of magnitude better than $HfSe_2$ based devices. More importantly, it is found that the photocurrent responsivity and speed increase significantly upon the temperature cooling to T_{CDW}, which is likely attributed to dramatic reduction in carrier scattering that occurs as a result of the switching from the normal to CDW phases in $TiSe_2$. Not only do these results further the understanding of group 4 TMDC materials but also offer promise for future investigations into these enticing class of materials, opening new phase considerations for future 2D optoelectronic engineering.

Chapter 5 Retina Electrophysiology

5.1 Introduction to Retina Electrophysiology

The human central nervous system (CNS) is a masterful work of nature. It is composed of billions of neurons and trillions of dendrites and synapses. Electrical signals pulse between and through these in large neuronal networks. The exploration of this electrical activity is imperative to understand how these units achieve higher function such as sight and cognition. These signals are the result of ionic movement across cell membranes, which is characterized by an action potential or more commonly referred to as a spike. These can occur spontaneously or as result of a stimulus. The characteristic intracellular action potential is shown in Figure 5.1.

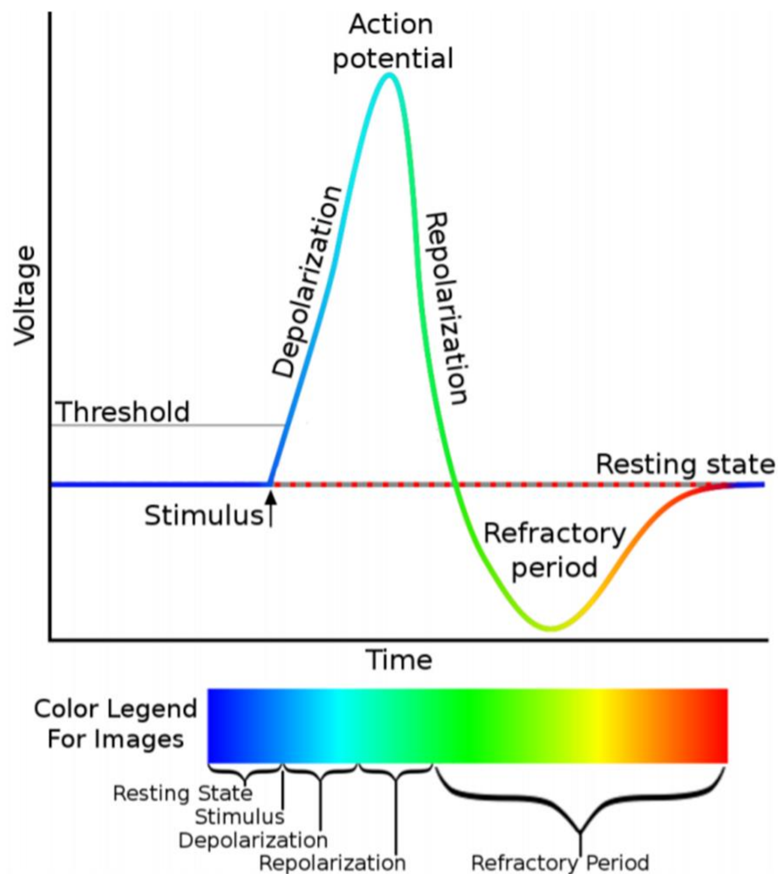

Figure 5.1 Characteristic Intracellular Action Potential. The voltage characteristic resulting ion movement due to a stimulus inducing the opening and closing of sodium and K^+ channels. Reproduced from Ref. [203] under (CC BY 4.0).

The inside of a cell is negatively charged due to protein molecules that cannot cross the cell membrane. As a result of a stimulus, sodium channels on the membrane open and the positively charged sodium ions rush inside making the neuron more positive and thus depolarized. At this peak the sodium channels close and the slower responding K^+ channels open and the positive K^+ ions now rush out of the cell and repolarize the cell. Due to the slower response, the K^+ channels stay open a little too long to return immediately to the resting state which results in a refractory period. A noteworthy consideration is that for sensing inside the cell this results in the polarity shown in Figure 5.1 but the polarity is reversed when sensing the same spike extracellularly.[203]

Various techniques have been developed to examine these signals. Each of these represents the pinnacle of scientific collaboration as many diverse disciplines must come together to enable technological advancement for an increased understanding of the CNS. These techniques are primarily characterized by their resolution (i.e. sensitivity and fidelity to the cellular activity) and their throughput (i.e. the number of cells measured). One common technique is patch-clamping, which examines the electrical activity of individual cells via a micro-pipette tip that is clamped on or near the cell (the ion source). This results in high resolution but is significantly limited in throughput. Ultra-high resolution has been demonstrated at the nanometer scale as shown in Figure 5.2a. In an attempt to remedy the throughput issue, numerous voltage sensitive dyes have been developed. Unfortunately, these are still far away from the resolution obtainable by patch-clamping as shown in Figure 5.2b. A more recently developed technique is to create an array of electrical contacts that are placed in close proximity to cells. These are either for implantation in tissue as shown in Figure 5.2c or tissue is placed on them as shown in Figure 5.5c. These are collectively known as micro-electrode arrays (MEAs). This technique offers a significant

advantage over the other techniques in terms of throughput and resolution.

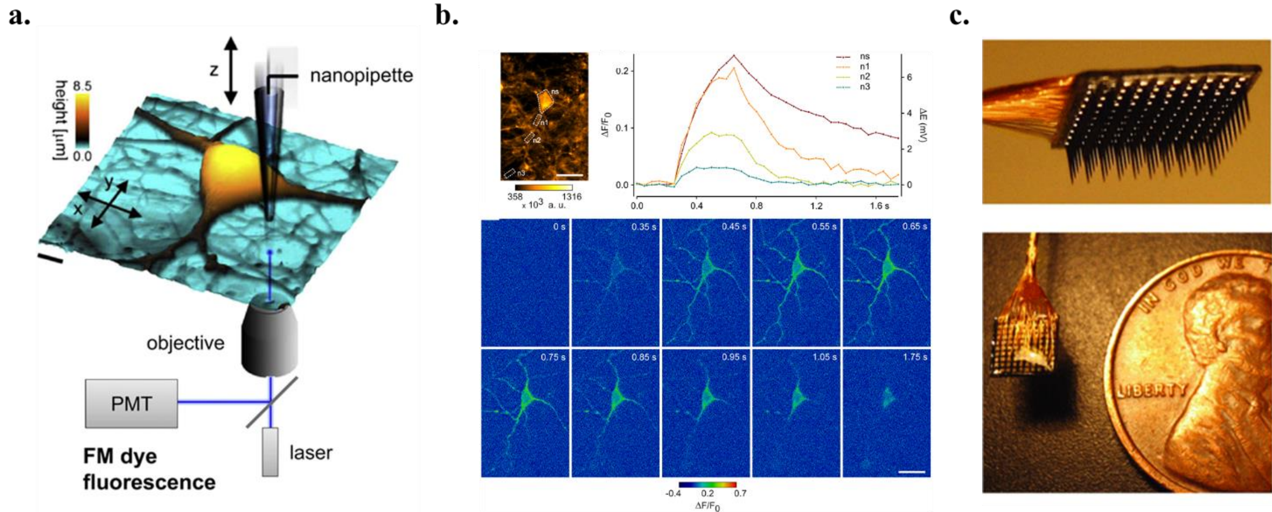

Figure 5.2 Comparsion of Common Electrophysiological Techniques. (a) A reconstructed image of a nanopipette patch-clamping scheme. (b) Summary of a voltage sensitive dye experiment showing the modulation in fluorescence nitensity with time to elucidate the action potential. (c) An optical image of an implantable MEA with a penny shown for scale. Images were reprinted from Ref [204] for (a) under (CC BY 3.0), [205] for (b) under (CC BY 3.0), [206] for (c) © 2007 Society for Neuroscience.

Additionally, the configuration of MEAs lend themselves to the incorporation of 2D materials to increase their throughput and resolution. The increased sensitivity of 2D materials to local potential changes, due to their large surface area to volume ratio, make SPCM a strong pathway to high resolution. The local potentials that results from the action potentials can alter the local band bending in the 2D material thus producing areas in which excited EHP can be efficiently separated to generate spatial photocurrent signals. This has been shown in retina previously at the optical nerve head on a graphene substrate but not yet at an individual cell level in tissue.[207] Since mice have two peak light sensitives, one to green (~505nm) and another to UV (~350nm), a NIR laser source and material with associated sensitivity to that wavelength region must be used for SPCM.[208] Furthermore, the use of mature semiconductor processes and graphene transfer techniques enables the creation of devices with large throughput. Though this has been

demonstrated previously in our group through in vitro experiments with graphene for primary hippocampal (brain) neurons,[209] the exploration of retina tissue and its associated light response for individual cell activity has yet to be fully realized. To achieve this the development of a perforated MEA configuration and the incorporation of individual graphene FETs is being investigated. The gain offered by graphene FETs are also able to achieve strong signal resolution as the current recorded during the experiment is able to effectively extract the action potential since it acts a local gate, which has been shown in *cerebrum in-vivo* experiments.[210] Furthermore, replacing the electrical contact pads that are typically gold or titanium nitride with graphene on custom MEAs can also increase sensitivity and enable other functional retina studies. [211] These incorporations are also able to fully take advantage of the transparency of graphene and potentially other 2D TMDCs to enable simultaneous functional and imaging study at the electrical source often obscured by the opaque electrodes in traditional MEAs.

Given the great disparity in attention paid to intracellular over extracellular measurements (particularly in mouse models), the primary aim of this chapter is to detail the expected activity for these devices based on results obtained from a custom adapted commercial perforated MEA (pMEA). A pMEA is chosen for this study since it has been shown to improve retina health and activity by providing a constant nutrient supply that is able to reach the surface of the MEA by perfusing through the retina, a feature not offered by traditional MEAs.[212] This is critical to establish a point of comparison and understanding for the results from a graphene based pMEA or other 2D TMDC devices for retinal electrophysiology. Additionally, a discussion of work regarding the inclusion of pressure in these custom devices is also offered.

The primary area for electrical activity measurements for MEAs in retina is found on the retinal ganglion cell (RGC) layer where action potentials are observed. The structure of the retina

is shown in Figure 5.3. The vitreous is a clear gel layer that fills the space between the lens and the retina insulating the RGC layer. The amacrine, bipolar, and horizontal cells all play a role in communicating and modulating the signal from light stimulation. Light passes through all these layers to the light sensitive rods and cones. The Müller glia cells span nearly the entire retina and primarily provides structural and functional support. The retinal pigment epithelium (RPE) and choroid provide nutrients and supports the retina as well as provide a dark background to prevent internal reflection. These cells are classified into the ganglion cell layer (GCL), inter plexiform layer (IPL), inner nuclear layer (INL), outer plexiform layer (OPL), and outer nuclear layer (ONL).

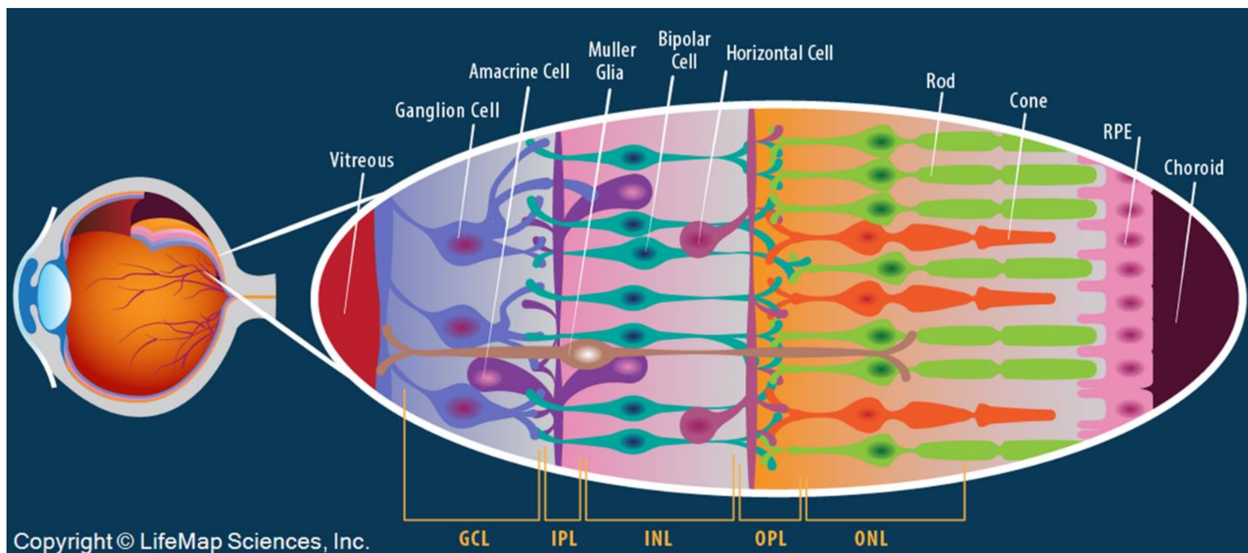

Figure 5.3 Structure of the Retina. The retinal structure showing the layers that light must travel through to stimulate the retina as well as propagate back through to produce action potentials at the RGC layer.

In addition to the structure of the retina, the structure of RGCs (shown in Figure 5.4) and the location of electrical sources of activity are necessary to consider. The primary source of electrical activity is due to the ion channels located in the membrane of the cell body but signals can also be detected at synapses (where dendrites of different cells meet) or along axons up to a certain point.[213] Retinal axons run from the individual RGCs and bundle together at the back

of the brain to form the optical nerve head continuing into the brain. To enable the integrity of electrical signals along their lengthy but quick journey (~millisecond), axons are covered in segments of a fatty substance known as myelin near the optic nerve head but not in the retinal layers.[214] To have appreciable electrical signals (signal-to-noise ratio >5), the electrode must be in close contact with these electrical sources (<30 microns).[215, 216] Beyond the general structure of RGCs there are over 30 different confirmed types of RGCs with varying morphologies ranging from 10 μm to 30 μm in diameter.[217] Additionally, there are over 30 different K^+ ion channels.[218] Both of these variables also modifies the spontaneous activity of RGCs.

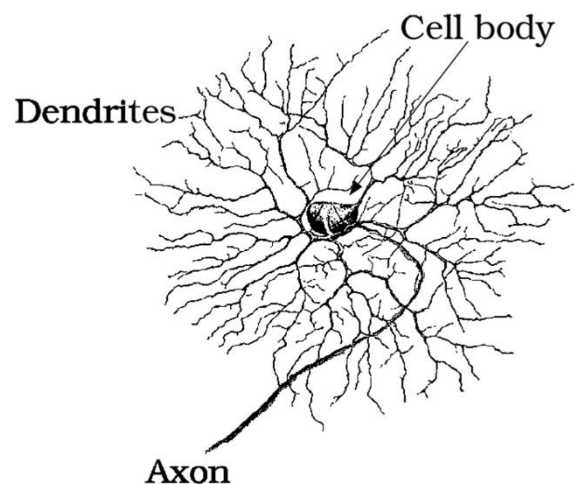

Figure 5.4 Structure of RGCs. Dendrites branch out from the cell body. An axon runs from individual RGCs and are bundled together at the back of the eye to form the optical nerve head. Reproduced with permission from Ref [219]. Copyright © 1992 Cambridge University Press.

5.2 Results and Discussion

Here a custom pMEA setup is used (described in further detail in appendix A.6) on an Olympus IX-81 inverted microscope to perform electrophysiology measurements on mouse retinal tissue using commercially available pMEAs (60pMEA200/30iR-Ti, Multichannel systems). The

primary elements of this setup are a heated perfusion inlet, a suction source, and an overflow cannula as diagramed by red, blue and purple arrows, respectively, in Figure 5.5a. The setup is diagrammed in Figure A.2. The custom designed and built holder (with assistance from John Fellenstein from the Vanderbilt University Physics machine shop) is shown in Figure 5.5b. From this top view of the MEA the large reference electrode on the left is shown. The electrical potential of the cells is measured relative to this electrode. This implementation represents roughly a 4 fold increase in channels (from ~13 to 43) available for recording over the configuration initially used in previous brain experiments and early retina experiments performed as part of this project. The mice used in these experiments were obtained from in-house colonies housed in Vanderbilt University Medical Center animal facilities. These colonies were established from mice acquired from Jackson Laboratories (Bar Harbor, ME). Three key elements are noteworthy for preparation of retina tissue to ensure high yield experiments. First, the removal of the eye cup (the anterior portion of the eye containing the retina) into oxygenated medium quickly after sacrificing the mouse is crucial to ensure that the RGC layer doesn't become hypoxic. Second, the use of an enzyme digestion is needed to remove the inner limiting membrane through immersion in a mixture of collagenase (241 units, Sigma-Aldrich Corporation) and hyaluronidase (5,685.5 units, Worthington Biochemical Corporation) for ten minutes to access the RGC layer. And third, the subsequent removal of vitreous tissue after the digestion is necessary to ensure good contact between the RGCs and pMEA. Retinal preparation was carried out by Dr. Edward Levine and/or Dr. Hannah Lee. The tissue (with the filter paper support) placed on the pMEA is shown in Figure 5.5c. The opaque areas are the electrodes. Each electrode consist of a 30 μm diameter exposed tip and are separated by 200 μm. The electrode material is composed of titanium nitride.

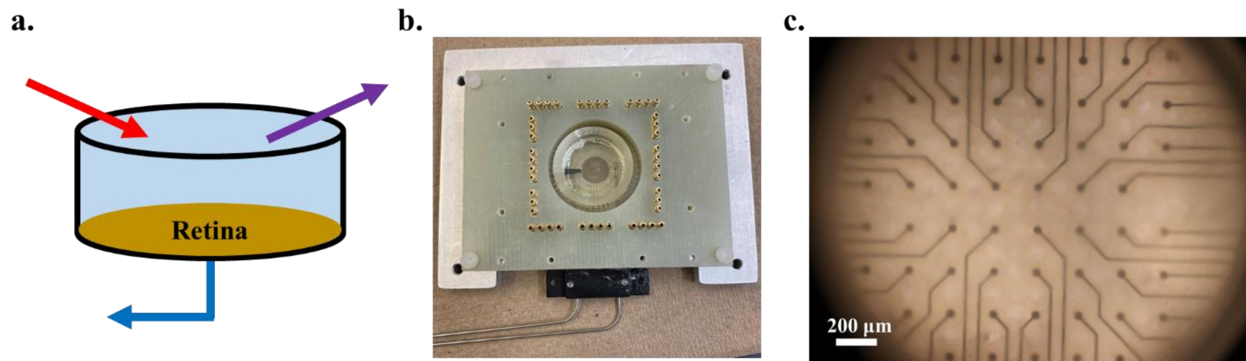

Figure 5.5 Simplified Diagram of Electrophysiology Setup. (a) Schematic of pMEA setup with heated cannula, overflow cannula, and suction channel shown in red, purple, and blue, respectively. (b) Custom designed MEA holder with the large reference electrode visible on the left. (c) Transmission imaging of a retina (with the filter paper support) placed on top of the MEA. Each dark area corresponds to a sensing electrode.

Two methods to stimulate the retina are performed in these experiments (detailed in appendix A.7.2). First, the introduction of a high K^+ concentration is used over the baseline Ames' medium to induce firing as RGCs attempt to obtain homeostasis. And second, light stimulation that primarily triggers the rods and cone to send that information to the RGC layer (detailed in appendix A.7.3). The results for one channel of the pMEA likely contacting a cell body during a standard K^+ stimulation experiment is shown in Figure 5.6. The experiment consists of three trials which typically show similar behavior from trial to trial for each respective channel. Additionally, a third to half of the channels will show similar signals of varying intensities and shapes in a successful experiment. During the experiment, voltage is recorded at a sampling rate of 20 kHz relative to a reference electrode in the well for each channel. This enables the shape of the action potential to be plotted as a function of time displaying a waveform for the electrical source (primarily cell bodies or axons) in contact with that electrode. Occasionally, a single electrode may touch more than electrical source producing different waveforms that typically can be extracted using sorting procedures. The sorting procedures used in this work were conducted in the Plexon

Offline V4 sorter. It is worth noting that massive amount of data generated in these experiments have necessitated the development of different algorithms and spike sorting methods. This process is still imperfect and remains an open research question.[220] The median of the spikes recorded during one cycle of stimulation is shown in Figure 5.6a. The inset of the Figure 5.6a shows all the spikes from that channel recorded during that portion of the experiment from which the median is calculated. To further analyze the frequency of the response, the spikes are then discretized with a time stamp indicating a firing of the action potential. These are counted and plotted as a histogram in Figure 5.6b. Each firing is often designated by a single tick and plotted as raster (rug) plot shown on the bottom of Figure 5.6b. This allows the visualization of the number of times the cell fires per second: the firing rate. The high K^+ is introduced at 2 minutes and stopped at 4:30 minutes. It takes ~1:30 minutes (depending on the set flow rate) to perfuse through the system and begin to reach the retina. Strong response is observed when the stimulus hits the retina followed by a depletion period where the retina is physically unable to fire due to a lack of necessary ion concentrations. The retina resumes spontaneous activity around the 8 minute mark. The statistical significance of the stimulus can be shown by plotting the spontaneous and stimulated firing rate on a box-and-whisker plot as shown in Figure 5.6c.

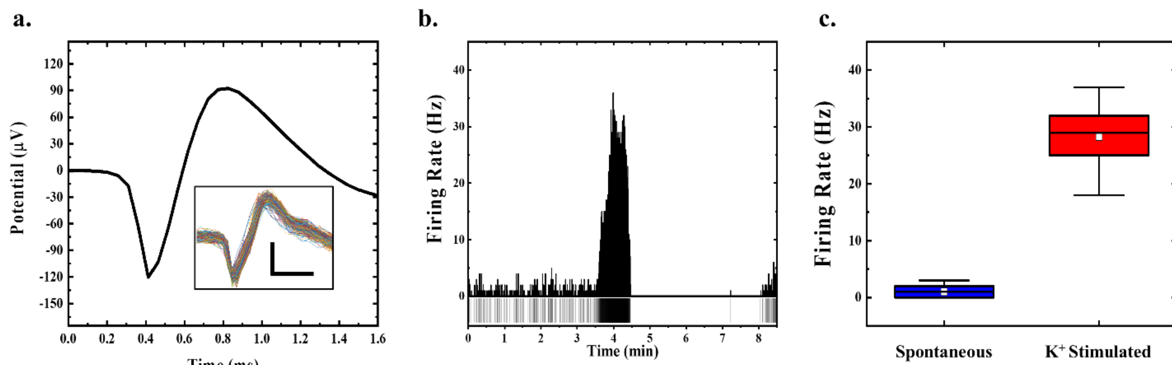

Figure 5.6 Standard K^+ Retina Experiment. (a) A median waveform extracted from all the spikes (shown in the inset, y-scale bar 50 µV and x-scale bar 500 µs) a trial of an experiment. (b) Histogram and raster (rug) plot of action potential firing rate as a function of time. (c) Box-and-whisker plot indicating the significance of the K^+ stimulation.

With the numerous electrodes available each sense similar but distinct behavior due to factors such as varying cell morphologies, dendritic connections, distribution of different K^+ channels, and distance to the electrode.[216] Figure 5.7 shows a sampling of medians from different electrodes during an experiment showing distinct waveform shapes and intensities. These are grouped into electrodes likely contacting cell bodies (Figure 5.7a - c) and those likely contacting axons (Figure 5.7d - f). The distinguishing factor between these two groups is whether they possess a biphasic (two primary concavities) or triphasic (three primary concavities) waveform. The nuances and subtleties in the differences of these waveforms within their groups demonstrates the complexity of signal propagation and the need for high resolution sensing methods to discern signal transduction. The basis for this is the volume conductor theory.[221, 222] According to this theory a soma or axon is isolated and surrounded by an extracellular medium of uniform resistance and no current is flowing at rest. As signals propagate as a result of ion channel activity the location near the sensing electrode for a soma becomes depolarized (Figure 5.9a) relative to the distant reference electrode and then repolarize (Figure 5.9b). And for an axon, as an ion channel fires the location in contact becomes a source of ions for the nearby depolarized signal thus producing a positive current (Figure 5.9c), then when the action potential is at the contact the negative depolarized voltage is sensed (Figure 5.9d) and finally the contact area is repolarized and becomes an ion source again. This suggest that the observed biphasic and triphasic activity are for soma and axons, respectively. Indeed, this has been confirmed to be quite accurate for axons [223] but the model breaks down when encountering the complexities arising at soma such as differing cell morphology or variations in dendritic connections, this can potentially explain the odd deviation from theory seen waveforms such as is observed in Figure 5.7a.[224]

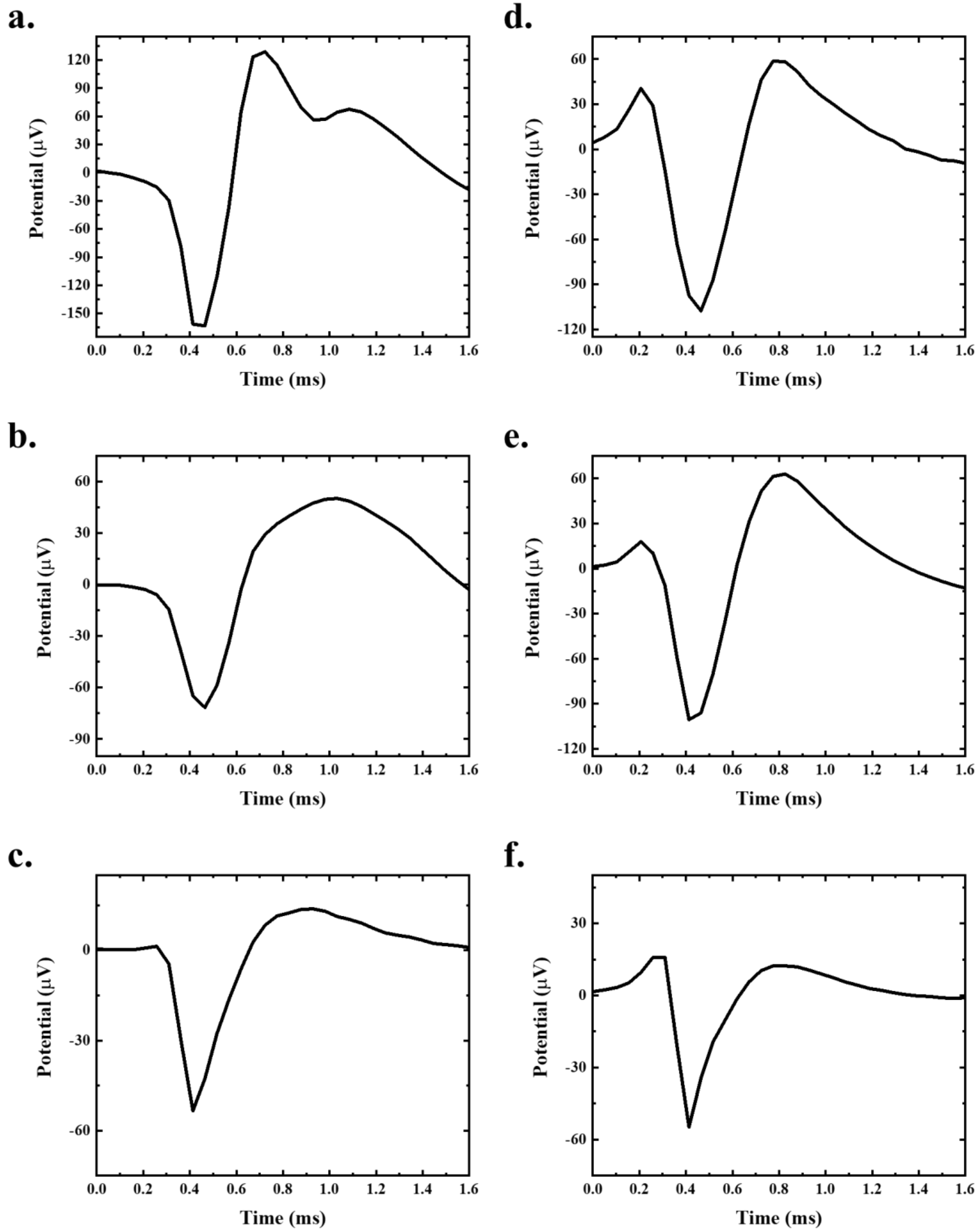

Figure 5.7 Observed Biphasic and Triphasic Extracellular Action Potentionals. (a) – (c) show characteristic biphasic action potentials of varying waveforms. (e) – (f) show characteristic triphasic action potentials of varying waveforms.

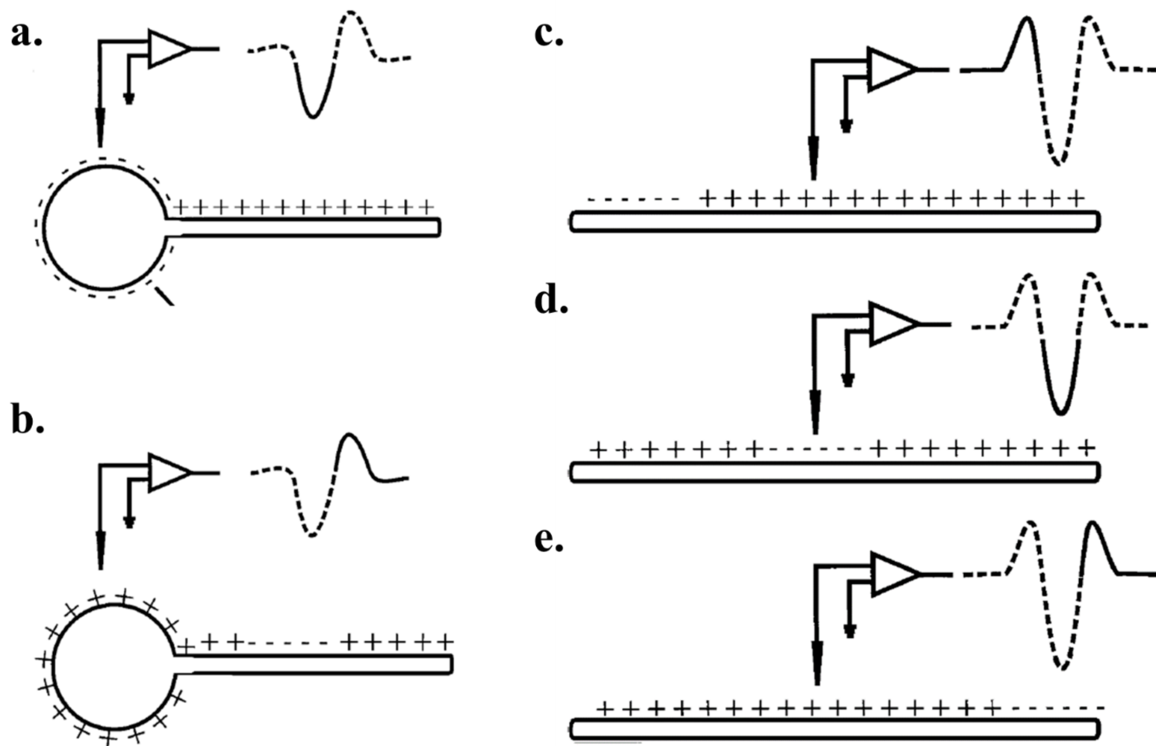

Figure 5.8 Volume Conductor Theory of Biphasic and Triphasic Extracellular Spikes. (a) and (b) show the conceptual frame for the polarity and biphasic nature of a spike at a soma according to volume conductor theory. In (a), the firing of an action potential results in a depolarization (negative) potential relative to a distant reference electrode that then results in (b) positive potential as the cell repolarizes. (c) – (e) show the conceptual frame for the polarity and triphasic nature of a spike along an axon according to volume conductor theory. As an action potential fires, the sensing region near the electrode becomes a potential source for a nearby depolarized membrane (c), as the action potential propagates the contact region becomes depolarized (d), and finally as the action potential continues the contact region becomes repolarized (e). Reprinted with permission from Ref [224]. Copyright © 2014 Thieme.

In addition to chemical stimulation via differential K^+ concentrations, retinal tissue is unique among neurons due to their ability to respond to light. The rods and cones in the retina act as photoreceptors (as well as some intrinsically photosensitive RGCs) and through various processes transduce signal through the horizontal, bipolar, and amacrine cell levels, to the RGC level where MEAs can sense the resulting electrical activity. There are a litany of different types of RGCs which respond to different types of light stimulation. The varied patterns of firing (cells turning ON) and ceasing firing (cells turning OFF) with combinations in between as well as

differing directionally sensitive RGCs can warrant complex light stimulation patterns to discern individual types.[217] But for demonstrating the ability to achieve high resolution and throughput for 2D incorporated MEAs, full field light stimulation can reliably result in ON and OFF cells that display transient or sustained responses. A sampling of observed ON and OFF transient responses are shown in Figure 5.9a and Figure 5.9b, respectively.

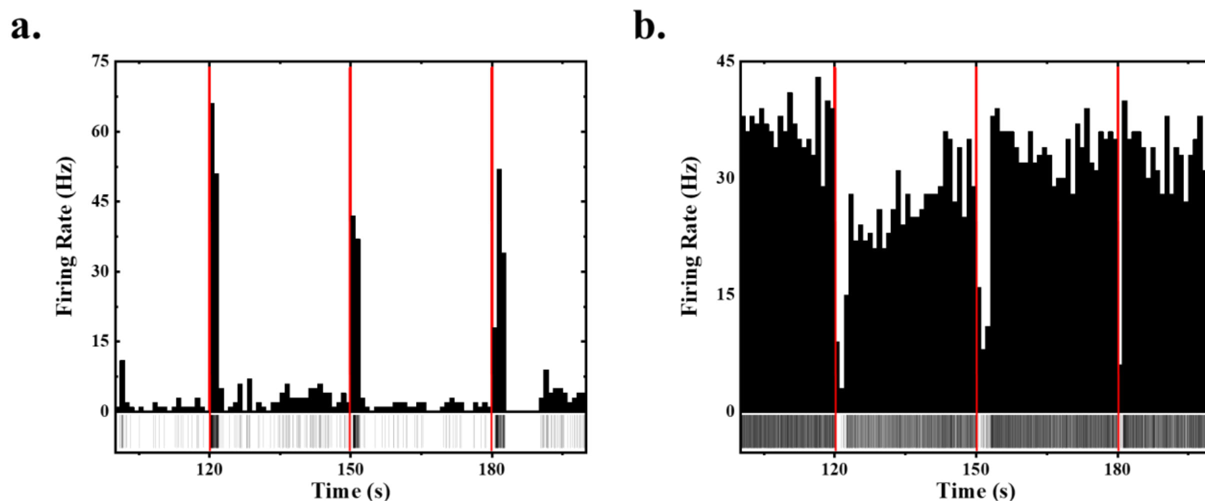

Figure 5.9 Observed ON and OFF Transiet RGC Response. (a) ON and (b) OFF transient light responses. Light stimulation (one second pulse) is indicated by red lines.

To explore light stimulation, different colors as well varying intensities and lengths were tested. Green (508.5 nm) and blue (475nm) as well as cool and warm white light was tested with no significant differences observed. This is likely due each of these light sources capturing the peak sensitivity in mice photoreceptors.[208] Additionally, provided sufficient intensity strong light response (change in firing rate) was typically observed. This is consistent with the "all or nothing" nature of action potentials. A sufficient stimulus must alter the potential to trigger a spike, otherwise the spike fails to initiate. Differing lengths of light stimulation were used (3, 5, and 10 seconds) and observed to produce significant variation in sustained ON and OFF RGC responses as shown in Figure 5.10. Longer light stimulations tend to produce clearer ON and OFF light stimulation response. Light stimulations of 3, 5, and 10 seconds for likely ON (OFF) cells are

shown in Figure 5.10a (5.10d), 5.10b (5.10e), and 5.10c (5.10f), respectively.

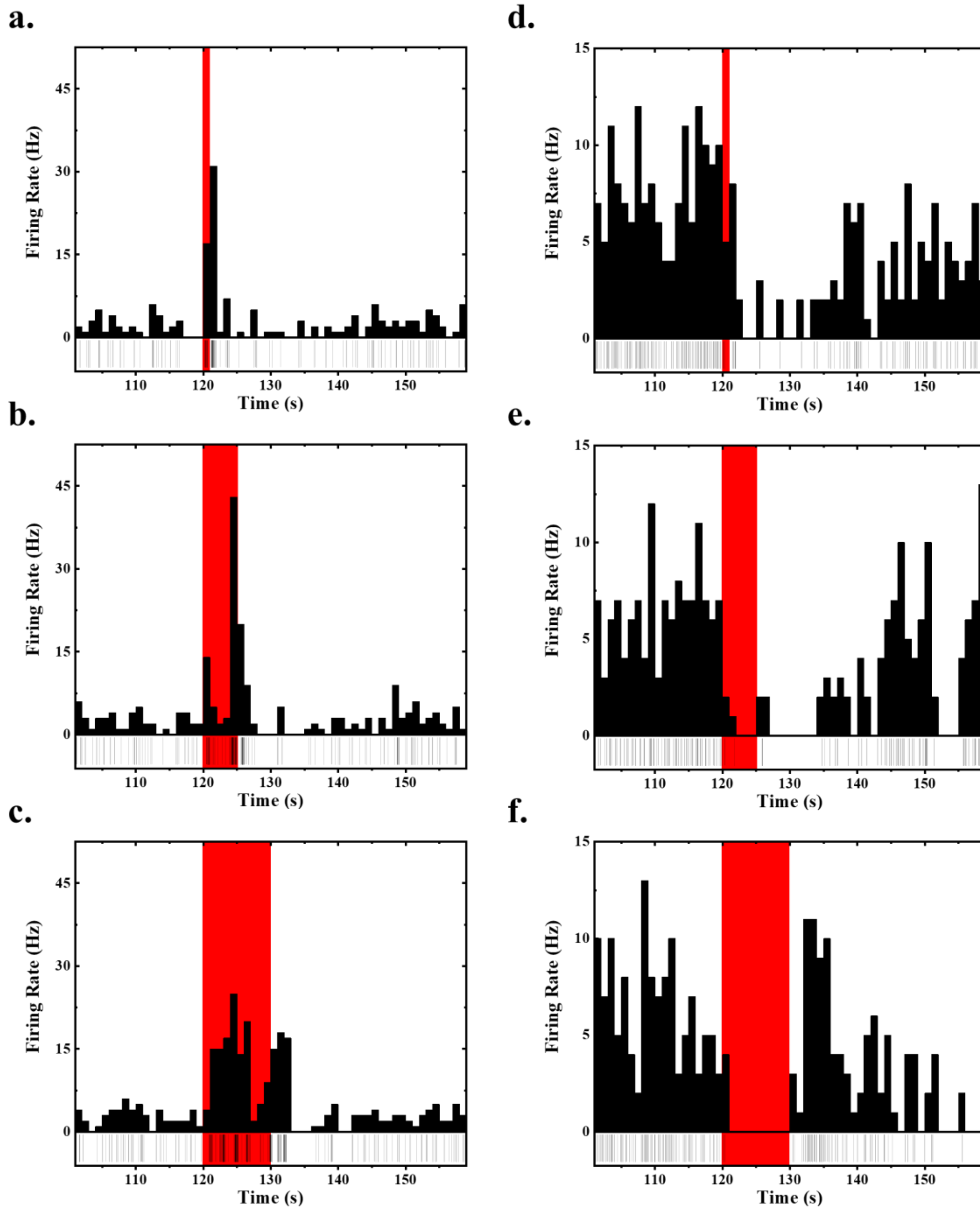

Figure 5.10 Variable Length Light Responses Showing Sustained ON and OFF RGCs. Sustained ON RGC light responses of 3 (a), 5 (b) and 10 (c) seconds. Sustained OFF RGC light responses of 3 (d), 5 (e) and 10 (f) seconds. Red background indicates the period of light stimulation.

5.3 Pressure Devices

In addition to the advancement in the sensing functionality enabled by 2D material incorporation into custom MEAs, the further exploration of novel microfluidic devices offers the possibility to more accurately study pathological phenomena in the retina such as glaucoma. Glaucoma is a group of eye conditions that is characterized by an increase in inter ocular pressure in the vitreous cavity which damages the optic nerve and likely has consequences for other portions of the retina. According to the Center for Disease Control (CDC) it is the second leading cause of blindness worldwide and currently has no cure. This underscores the importance of understanding the morphological and physiological changes that underlie the condition. In this section, the as demonstrated ability for graphene to maintain photocurrent integrity under pressurization as well as an *ex-vivo* retina in a pressurized chamber is briefly examined.

To study the ability for photocurrent signals to remain unchanged after being subjected to pressure, graphene photodetector devices were fabricated on top of coverslips. Electrodes (40nm of Au/5nm of Ti) were prepared on 170 μm coverslips via standard photolithography and deposition processes. Graphene was then grown on copper foil via a standard chemical vapor deposition technique (at 1000℃ under the flow of 20 sccm of CH_4 and 80 sccm of hydrogen for 30 minutes). [179] Graphene was then transferred from the copper foil to the coverslips using a bubbling transfer method.[225] The presence and quality of graphene was verified using Raman spectroscopy. The devices were then given to Matthew Fitzgerald to fabricate a microfluidic chamber that serves as a pressurizable *in-vitro* culture platform. One of the channel areas of the device are shown before and after pressurization in Figure 5.11a and 5.11b, respectively. Scanning photocurrent images under 785nm laser illumination show nearly identical behavior before (Figure 5.11c) and after (5.11d) being pressurized. The strong photocurrent signals observed at the metal-

graphene contacts are likely due to the formation of Schottky like barriers which create electric fields efficiently separating photo-excited EHPs.[207]

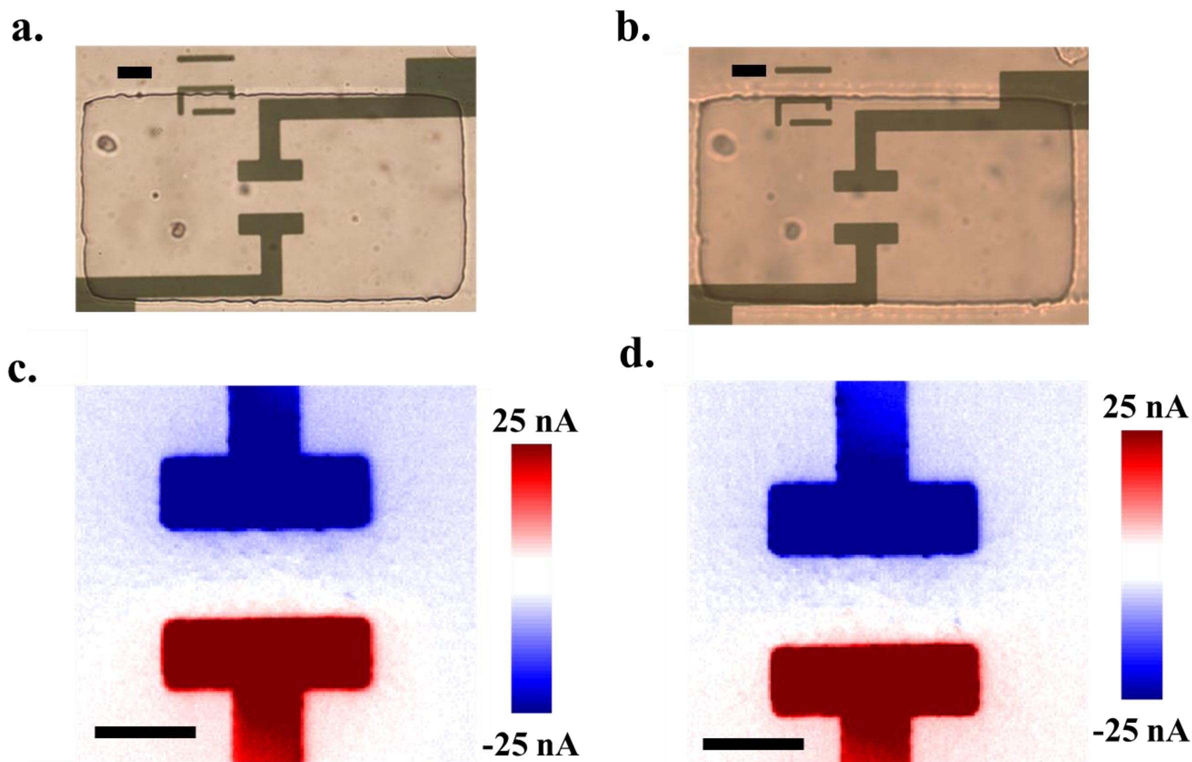

Figure 5.11 Photocurrent Integrity in Pressurizable Graphene Microfluidic Culture Chamber. Optical images two electrodes in a channel area that is covered with graphene (a) before and (b) after being pressurized. Corresponding photocurrent imaging is shown in (c) and (d). All scale bars are 20 μm.

An example cultured neuroblastoma cells (prepared by Dr. Lauren Wareham) on similar graphene devices is shown in Figure 5.12. Differential interference contrast (DIC) imaging is shown in Figure 5.12a with corresponding green Cholera Toxin Subunit B (CTB) fluorescence imaging shown in Figure 5.12b. DIC imaging is a beautiful optical technique in which the polarization of light is manipulated to produce images that appear to be three dimensional.

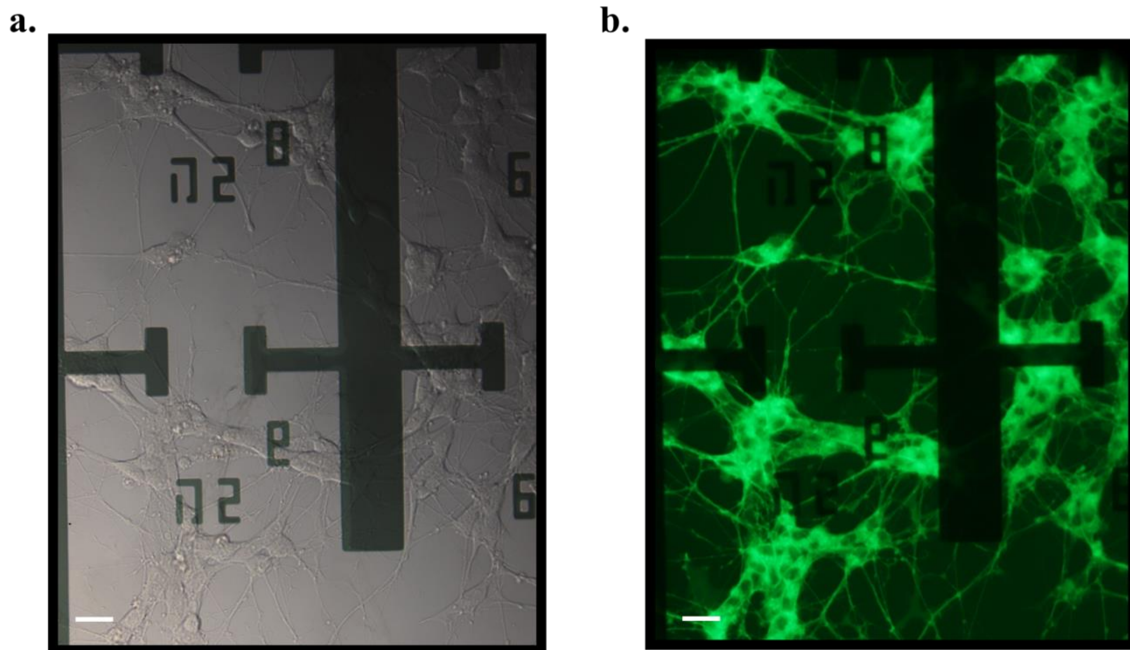

Figure 5.12 DIC and Fluoresce Images of Neuroblastoma. (a) DIC and (b) corresponding green CTB fluorescence images of neuroblastoma cells on graphene coverslip devices. All scale bars are 20 μm.

And finally, turning attention back to full tissue retinal electrophysiology, pressure chambers for continuous *ex-vivo* examinations have sparsely been explored. Studies have tended to focus on imaging or measurements after a period of time but not during pressure induced changes.[226] Microfluidic platforms and further incorporation of transparent graphene electrodes could offer a solution for revealing pressure effects on retina by combined imaging and functional studies. Green CTB fluorescence imaging of the full retina with the optical nerve head and axons clearly is shown in Figure 5.13. This work is done in collaboration with Alberto Esteban Linares and Dr. Lauren Wareham.

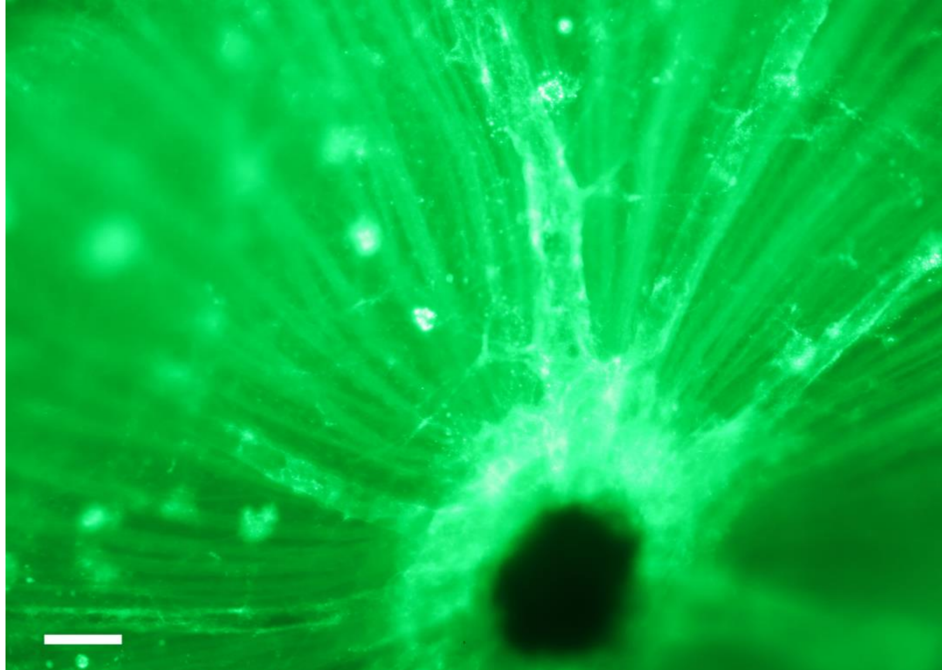

Figure 5.13 Green CTB Retinal imaging. Axons radiating from the optical nerve head (opaque portion near the bottom of the image) can clearly be observed. Scale bar is 50 μm.

Chapter 6 Conclusion and Future Outlook

6.1 Discoveries in NIR TMDC Photodetection

In this work several contributions to the existing literature regarding near infrared photodetection are presented by investigating 2D TMDCs in $PdSe_2$ phototransistors, in BP-MoS_2 vertical heterostructures, and in the electron-photon interactions in the charge density phase of $TiSe_2$. Additionally, expected results for the incorporation of 2D materials into perforated micro-electrode arrays is established helping to fill the gap in literature between intracellular and extracellular retinal studies.

Several key results are presented for these NIR photodetectors. For phototransistors fabricated from the puckered pentagonal structure of $PdSe_2$, a fast response time of ~156 μs is observed which presents a two order of magnitude improvement over other noble TMDC devices. SPCM reveals that the photocurrent generation primarily results from the PVE when the transistors are in the off state and is partly attributed to the PTE when they are in the on state. Related gate dependent electrical transport measurements reveal consistency with theoretical predictions for the Seebeck coefficient. Thickness dependent wavelength measurements reveal several NIR peaks that are likely the result of indirect optical transitions induced by strong interlayer coupling. For vertical BP-MoS_2 heterostructures, systematic wavelength and gate dependent SPCM measurements help to answer the observed variability in response times reported for BP and MoS_2 based devices. Tuning the gate voltage results in a reduction of response time by an order of magnitude for certain wavelengths and gate voltages. This is attributed to the modulation of the width of the Schottky barrier at the MoS_2-metal interface. For $TiSe_2$-metal junctions, a halving of the response speed and a doubling of the rate that the responsivity increases with decreasing temperature are observed when in the CDW phase. This reduced photo response speed of ~31 μs represents a two order of

magnitude improvement over other group 4 TMDCs such as $HfSe_2$. Both the PVE and PTE are shown via SPCM to be contributing photocurrent generation mechanisms in the CDW phase, while in the normal phase the PVE appears to dominate. These investigations not only contribute to the understanding of 2D TMDCs for NIR photodetection but also open new avenues for engineering future ultra-thin and fast optoelectronic devices.

6.2 Perspective on 2D Material Devices

Undoubtedly 2D materials offer immense potential for next generation electronic and optoelectronic devices. From ultra-high mobilities enabling unprecedented electrical speeds to enhanced multifunctional photodetection, 2D materials offer unrivaled thinness as well as literal and figurative flexibility. These advantages are often focused on the ability to probe novel biological questions or enhance current biological sensors, as described with reference to retina electrophysiology in this work. And though this emphasis will likely remain a primary route for the incorporation of 2D materials, their use in traditional electrical and optoelectronic devices should not be neglected. The major obstacle to this more traditional approach is the question of how these materials or devices can be scaled. Variability between samples resulting in device uniformity issues as well as the time intensive process of device fabrication are critical concerns. While some of these issues are being addressed through advanced growth techniques to produce wafer sized mono-layer crystals,[227] many materials or device architectures may only be readily accessible in their 2D forms through mechanical exfoliation.

To effectively address these concerns, a turn to data science could prove pivotal for future scaling. Currently emerging work has demonstrated the ability to use machine learning techniques to identify 2D material samples and thicknesses using optical imaging as well as to automate the fabrication of vertical heterostructures.[228-230] Combing these efforts with a transfer

metallization scheme as implemented in this work during the fabrication of $TiSe_2$-metal junctions would greatly accelerate the creation of 2D material devices. Furthermore, the diffusion and increased accessibility of these data science techniques are poised to provide pathways to rapid scaling. A basic example of 2D material identification is shown in Figure 6.1 for a $TiSe_2$ flake used in these studies. The flakes are identified by an edge detection processes recently incorporated into the Image Processing Toolbox offered in Matlab.

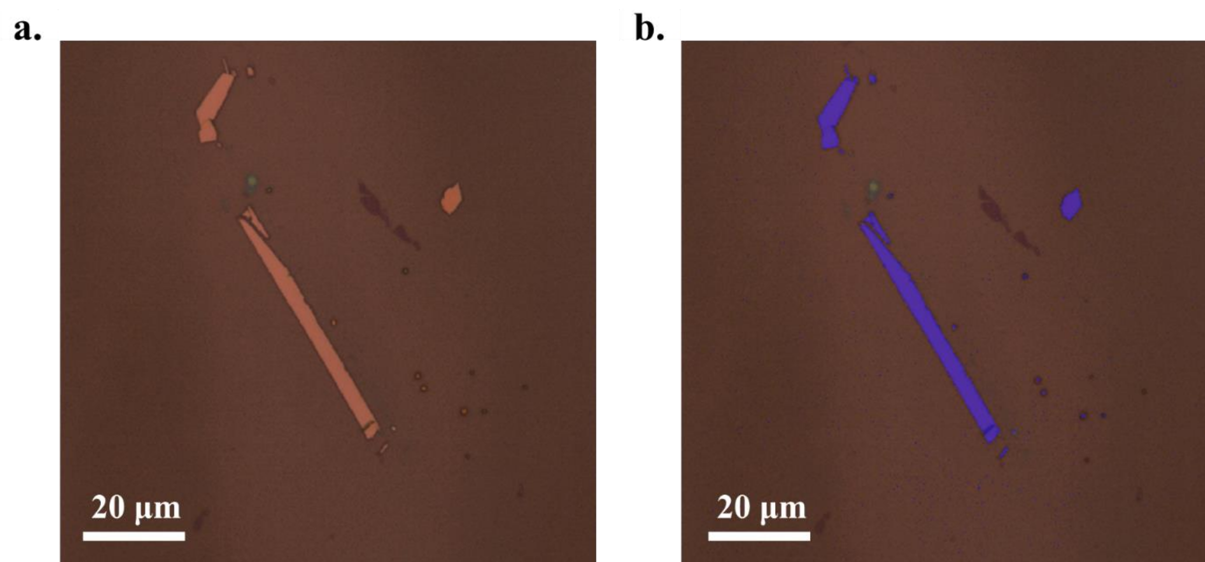

Figure 6.1 Example of Basic Edge Detection. (a) Optical imaging of $TiSe_2$ flakes on a Si/SiO_2 substrate. (b) An overlay of basic edge detection using the sobel method via the Image Process Toolbox available in Matlab.

A final reflection on the trajectory of 2D TMDCs for NIR photodetection is perfectly encapsulated by looking at the first transistor (Figure 6.2) created by physicists John Bardeen, Walter H. Brattain, and William B. Shockley at Bell laboratories. This enormous single transistor revolutionized society and laid the groundwork for the billions of transistors that surround everyone's lives today. In the decades since this monumental discovery, thousands more enabled the massive cheap fabrication of miniaturized and advanced devices. Though the seemingly

Lilliputian endeavor of fabricating and researching 2D materials can engender hopelessness in the face of a need to scale, the recognition of the accelerating pace of scientific innovation in the 20th and 21st century underscores the inevitable advancement and impact of these materials. Modern scientific research is a game of inches, not miles, and only the sustained investment in discovery, *however small*, will continue to propel us forward.

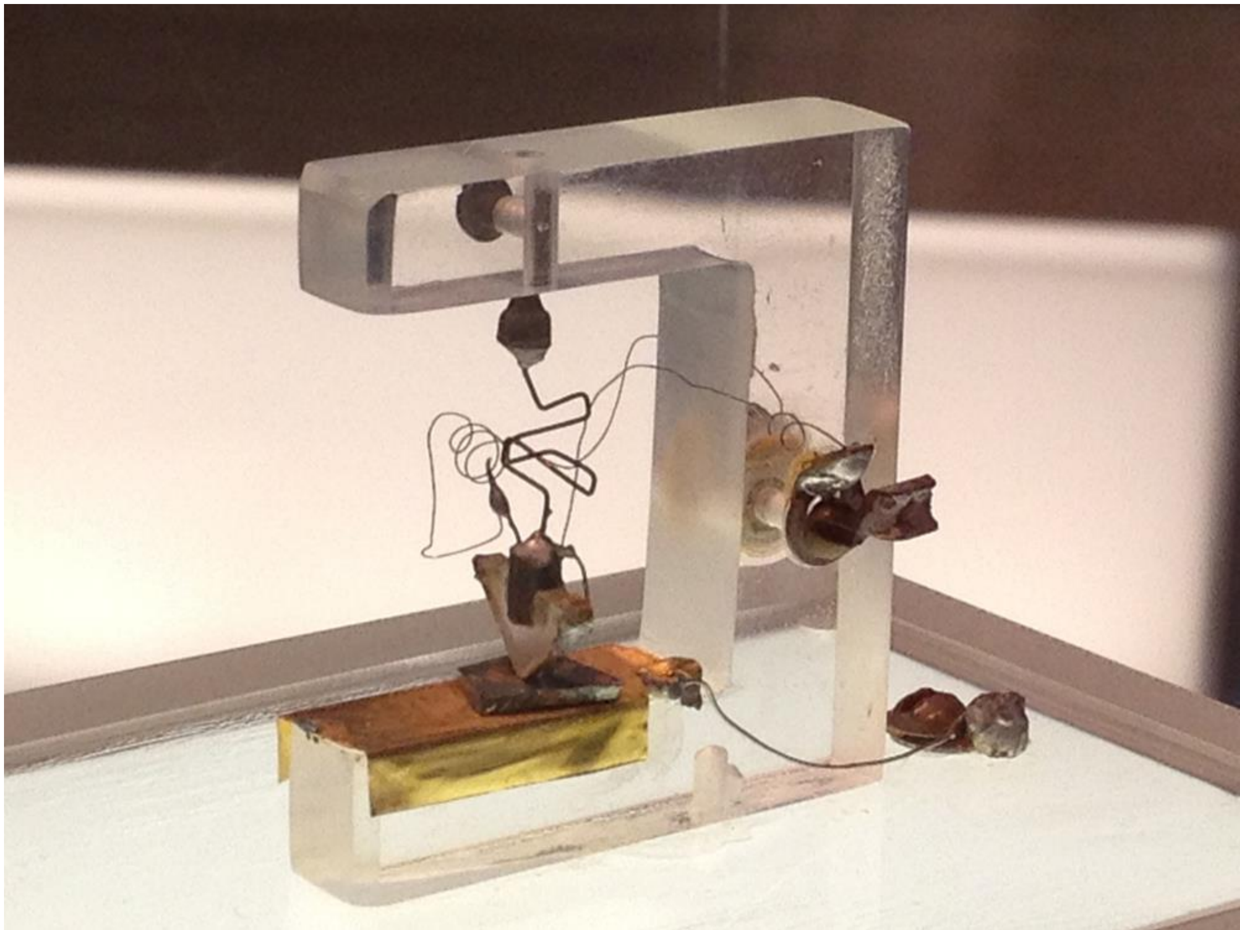

Figure 6.2 First Transistor Fabricated at Bell Laboratories. The point contact transistor consisting of a plastic wedge holding gold foil in contact with germanium. The emitter and collector leads are connected to the gold foil on each side of the wedge. The base lead is connected to the germanium. Reproduced from Unitronic under Creative Commons Attribution-Share Alike 3.0 Unported license (CC BY-SA 3.0).

APPENDIX

A.1 Laser Optical Path

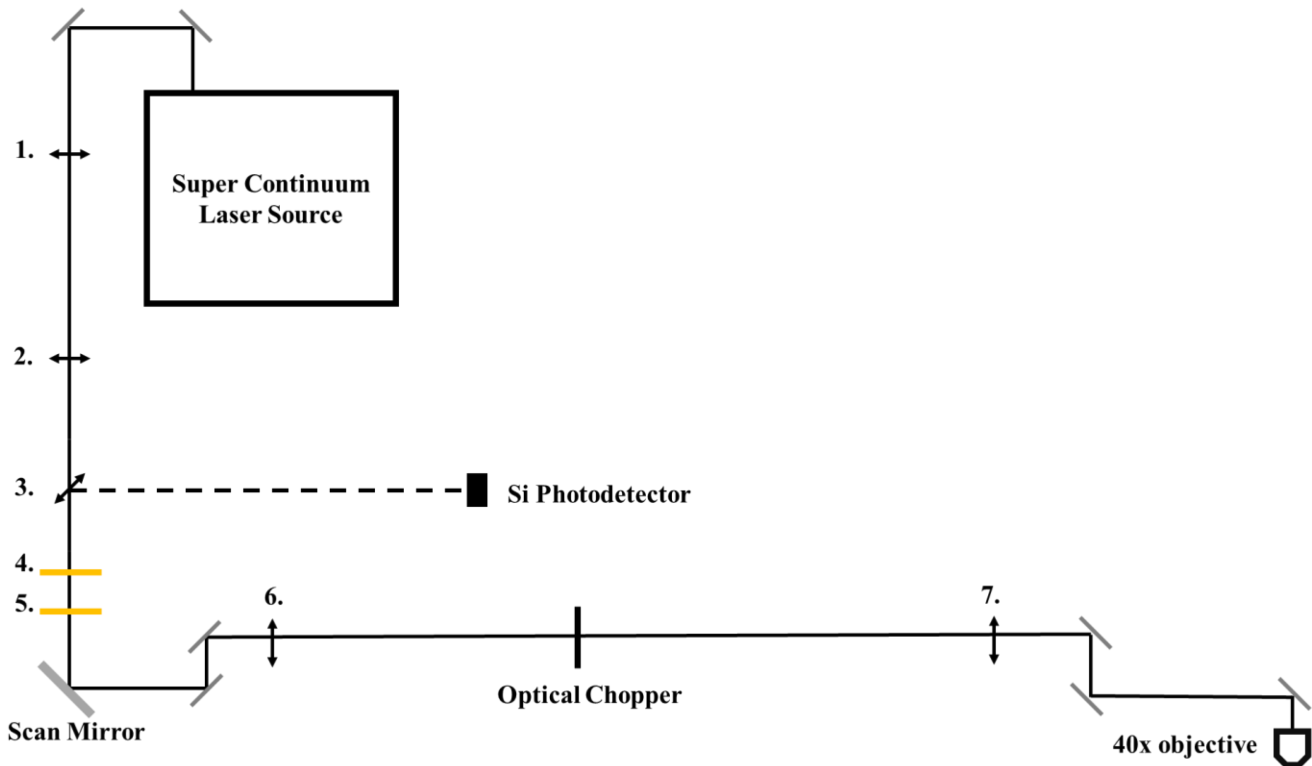

Figure A.0.1 Laser Optical Path for TMDC Scanning Photocurrent Microscopy Setup.

Optical Elements

1. Thorlab, AC254-300B
2. Thorlab, AC254-100B (200mm from 1.)
3. Thorlab, BP108 Beam splitter (R 8% T92%)
4. Thorlab, Halfwave plate (AHWP05M-600/AHWP05M-980)
5. Thorlab, GL10 Glan-Laser Polarizer Uncoated
6. Newport, SPX030 Uncoated 150mm (150mm from scan mirror, 500mm. to 7.)
7. Newport SPX030 Uncoated 350mm (350mm to objective)

45° Gray dashes are Thorlab, PF10-03-P01Silver Mirrors
Si Photodector Thorlab, PDA 36A
Scan Mirrors – pair of Nutfield Technology, RS 15
Optical Chooper – Scitec model 300CD
40x Objective – Olympus LUCPlanFLN, NA 0.60
Super Continuum Laser Source – NKT Photonics, SuperK Select

A.2 Electrode Preparation

1. Spin coat a Silicon wafer with a negative photoresist (NR9, 1000PY) at 4000 rpm for 45 seconds and pre-bake on a hot plate set to 150°C for one minute.
2. Exposure electrode pattern
3. Post-bake on a hot plate set to 100°C for one minute and then develop for 10-20 seconds.
4. Deposit 50nm of gold via electron beam or thermal deposition.
5. Liftoff with acetone then transfer wafer to IPA then DI water and then blow dry with nitrogen.
6. Spin coat prepared wafer with S1805 at 2000 rpm for 45 seconds and bake on a hot plate at 115°C for one minute and dice into desired size.
7. Clean the diced pieces with acetone, IPA, and DI water then blow dry with a nitrogen gun.
8. Treat the clean diced pieces with HDMS. Treatment time and temperature vary and are dependent on electrode pattern. For the given electrode pattern, fill glass desiccator with 200ml of HMDS and heat on a hot plate to 180°C, once HMDS has vaporized treat pieces for 30 minutes.
9. Immediately following HDMS treatment, spin coat two layers of PMMA 495 A11 at 2500 rpm by baking at 180°C for 2 minutes after spinning each layer.

A.3 Substrate Preparation

1. Obtain a blank Si/SiO_2 wafer and note oxide thickness (285nm used for $TiSe_2$ devices).
2. Spin coat wafer with S1805 at 2000 rpm for 45 seconds and bake on a hot plate at 115°C for one minute and dice into desired size. When dicing into desired size consider the size of the target chip carrier and vacuum stage. 8mm x 8mm dicing size is recommended.
3. Clean diced pieces with acetone, IPA, and DI water then blow dry with a nitrogen gun.
4. Clean the diced pieces with Nanostrip. Exercise extreme caution and follow all safety protocol.

A.4 Electrode Transfer

1. Prepare PDMS in a 10g:1g ratio in clean 100mm petri dish to achieve proper stamp thickness. Depending on cure method this should be prepared several days ahead of time to ensure optimal stickiness.

2. Exfoliate desired 2D material onto Si/SiO_2 substrate and identify target flake. Place target substrate on vacuum stage and supply 8V to the vacuum pump. Ensure the substrate is well fixed by gently pushing with a pair of tweezers.

3. Use double sided tape on the backside of prepared electrodes and adhere to a firm surface.

4. Use a razor blade to trim the edges of the prepared electrodes to remove any PMMA that may have a connection with the sides of the sacrificial silicon wafer. Quick deliberate actions produce the most optimal electrodes.

5. Cut PDMS into a square stamp slightly larger than the electrode pattern and place on a clean glass slide.

6. Align PDMS stamp over electrode pattern and press down and then quickly up to pick up the electrodes/PMMA with the PDMS.

7. Insert the electrode/PMMA/PDMS/glass slide stack into the custom alignment stage. Align the electrodes with the target flake and lower the stack ensuring the PMMA makes full contact and the PDMS squishes slightly.

8. Heat custom stage to 60°C.

9. Remove the electrode/PMMA/PDMS/glass slide stack extremely slowly. This final process can take upwards of an hour. As the PMMA adheres to the substrate and peels off the PDMS stamp a line can be observed. This line should move very slowly across the sample as you raise the stack until the PMMA has fully peeled off. Patience is key. It is best to raise slowly until you see movement (the line indicating the peeling off of the PMMA) and only raise further once movement has ceased.

A.5 Electron Beam Lithography (EBL) to Enable Wire Bonding and Finishing Devices

1. Prepare images of devices beforehand to have as reference to know which windows to open.
2. Load samples into the universal specimen holder. Ensure that the electrodes are perpendicular to the edge of the clips.
3. Follow the EBL instructions in the black binder for imaging.
4. Use the 60 µm aperture at 30kV and a working distance of 10mm. This should result in a beam current of ~1.7nA.
5. Once a sharp image of the devices is obtained, approach the samples ensuring not to expose

the target area.

6. Open the pattern file that matches the electrodes and edit to make sure it is writing at the proper location and over the proper electrode pads.
7. Adjust the write area so that the aforementioned boxes correspond with the target area.
8. Set the UV coordinate system by picking three known locations from the pattern. For optimal results choose points that do not have either the same x- or y- coordinate.
9. Perform write field alignment twice once at 10 µm and then again at 5µm. The easiest way to find a feature to focus on for this procedure is to move outside of the PMMA area and find a 2D material piece.
10. Measure the beam current and drive back.
11. Correct all red numbers in the calculator button to ensure the correct dose has been calculated for each feature type.
12. Create a position list and drag the pattern file into it.
13. Make sure to check the layer to be written and check the write field.
14. For a beam current of ~1.7 nA set the dose factor to 12. For a beam current of ~1.9 nA set the does factor to 11.
15. Execute the position list.
16. Drive back to the Faraday cup and approach the next sample.
17. Repeat steps 6 through 15 for each of the samples.
18. Follow the unload procedure in the EBL instructions binder.
19. Develop in 1:3 MIBK/IPA for 15-30 seconds.
20. Wash in DI water for 15-30 seconds.
21. Carefully blow dry with a nitrogen gun.
22. Image samples under optical microscope.
23. Depending on chosen chip carrier, 1 to 3 devices may fit. It is best to place the maximum number of devices on a chip carrier. This may require cutting the Si/SiO_2 substrate. To do this, place sample on the edge of a glass slide then carefully cut with a diamond scribe. Then place and hold tightly a glass slide on top of the sample and glass slide on one side of the scribe and push down with the slide on the other side. Due to the crystalline nature of the Si/SiO_2 substrate it should cleanly break. During this process be sure to choose a cut location that doesn't result in the glass slide being placed on the PMMA.

24. Once devices are cut to size, mount in chip carrier with a piece of carbon tape. Be sure to leave room to bind to the back of the chip carrier to enable the application of a back-gate voltage.
25. Proceed to wire bind the device. Ensure that the profile of the wires are low so as to avoid contact when loading in the cryostat. It is also best to bind several different pads to the back of the chip carrier to have multiple options for the back gate voltage.

A.6 Retina Electrophysiology Setup

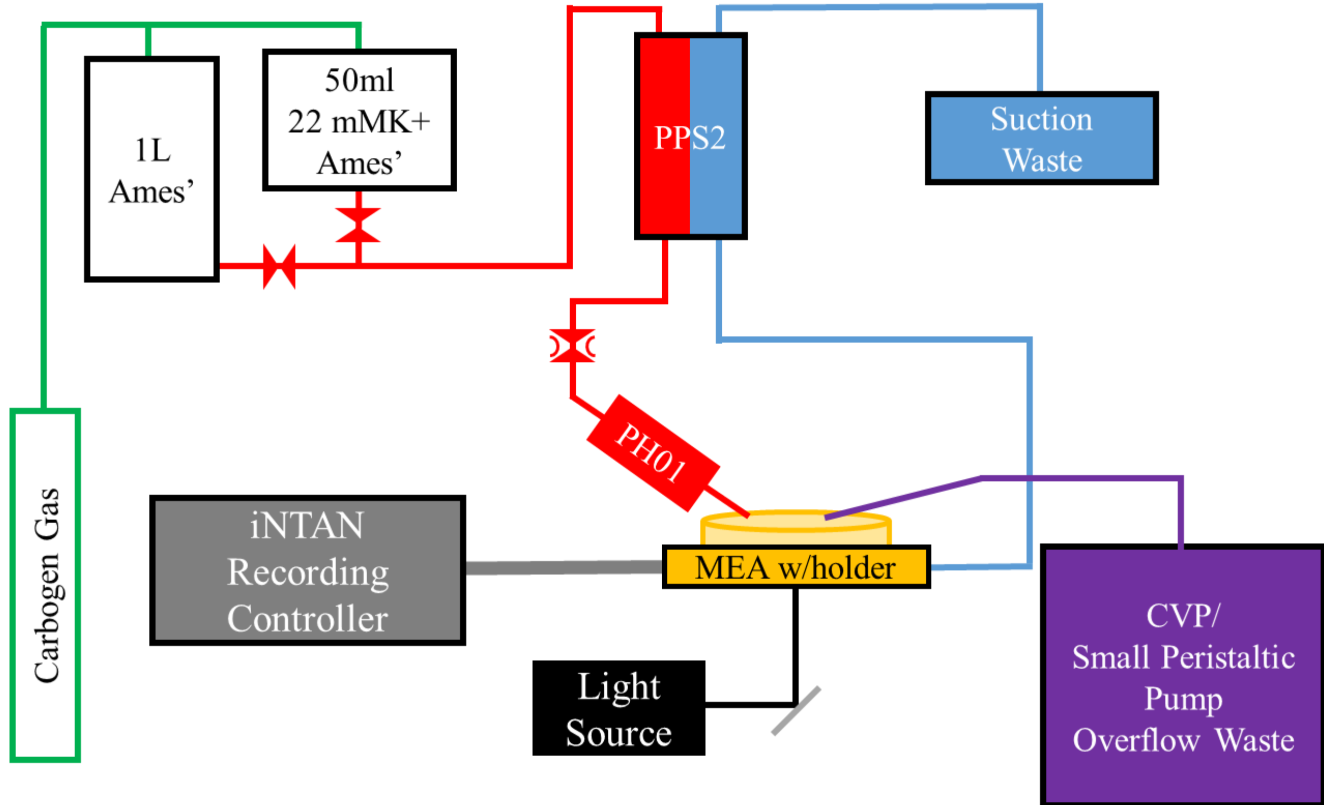

Figure A.0.2 Retina Electrophysiology Setup.

The elements of this setup are defined as follows:

(1) Green lines indicate the tubing that oxygenate the media that will be perfused into the retina well and MEA holder (shown in gold) mounted on an IX-81 Olympus microscope.

(2) Red lines indicate the path of base and stimulant media drawn through by one channel of a two channel peristaltic pump (PPS2, Multichannel Systems) and drip feed through a heated cannula (PH01, Multichannel Systems). Two gate valves and one flow control valve are indicated in the diagram.

(3) Blue lines indicate the suction provided by a second channel of the peristaltic pump (PPS2, Multichannel Systems).

(4) Purple lines indicate the overflow cannula that maintains a constant liquid level in the well via a Constant Vacuum Pump (CVP, Multichannel Systems) or a small

peristaltic pump.

(5) Grey lines the electrical connections to the iNTAN data acquisition unit (RHD 512 channel Recording Controller, iNTAN Technologies)

(6) Black lines indicate the optical path of the light stimulus that comes through a 10X UPlanSApo Olympus objective.

A.7 Retina Preparation and Experimental Protocols

Retina dissection as well as baseline date collection occurs in oxygenated Ames' medium. [231] The medium is glucose enriched and prepared from powder Ames Medium formulation with L-Glutamine (Sigma-Aldrich, A1420 or US Biological Corporation, A1372). For one experiment involving two retina over the course of several hours the following medium preparation instructions and amounts are used to enable the simultaneous preparation of baseline and high K+ Ames'.

1. Fill a clean 1L bottle with deionized (DI) water.
2. Place a magnetic stirrer in the bottle and place on stirring plate (500 rpm for a small stirrer).
3. Prepare Media.
   i. The powdered media from Sigma-Aldrich is proportioned in vials and its contents should be added to the 1L bottle. (Make all the powder makes it into the bottle, to do this reserve some water from the 1L of DI water and rinse the Ames' vial adding back to the 1L bottle).
   ii. For the unproportioned container from US Biological, measure 8.8g of the Ames' powder and add to the 1L bottle of DI water.
4. Mix until liquid is clear (<3 min).
5. Add 3.6g of glucose to the 1L Ames' medium bottle.
6. Pour 100ml of this mixture into a 500ml bottle for the 22mMK+ stimulant.
7. Add 1.71 g of Sodium Bicarbonate $NaHCO_3$ to the remaining 900ml of the Ames' medium bottle and close the cap. Mix until liquid is clear (<3 min).
8. Place a magnetic stirrer in the 22mMK+ stimulant bottle and place on the stirring plate (~300 rpm for a long stirrer).
9. Add 0.22 g of Potassium Bicarbonate ($KHCO_3$) to the 22mMK+ stimulant bottle and close the cap. Mix until liquid is clear (<3 min).
10. If prepared more than an hour before the experiment place both bottles in the refrigerator to maintain purity of the solution. Prepared media should be used within a week.
11. The Ames' medium and 22mMK+ stimulant should be oxygenated with carbogne gas (95% CO_2/5% O_2) for at least 50 minutes prior to dissection.

A.7.1 K^+ Stimulation Protocol

1. Once a steady state of spontaneous activity is reached begin data collection.
2. Collect data and at the 2 minute mark open the value for the stimulant medium and close the Ames' medium line.
3. After ~1:30 to ~2:30 minutes (this is the timing for 2ml/min perfusion in) you will see an increase in frequency of spikes and then all activity will cease. Turn off the stimulant medium and resume the baseline Ames' medium.
4. Continue recording monitoring activity returns and reaches a steady state and the cease recording about the 10 minute mark.
5. Repeat this for two more trials, no delay is necessary between trials.

A.7.2 Light Stimulation Protocol

1. Once a steady state of spontaneous activity is reached begin data collection.
2. Collect data for 2 minutes
3. Pulse light for 1/3/5/10 seconds at 30 second increments three times for each exposure length.

REFERENCE

1. Novoselov, K.S., et al., *A roadmap for graphene.* Nature, 2012. **490**(7419): p. 192-200.
2. Phiri, J., P. Gane, and T.C. Maloney, *General overview of graphene: Production, properties and application in polymer composites.* Materials Science and Engineering: B, 2017. **215**: p. 9-28.
3. Novoselov, K.S., et al., *Electric Field Effect in Atomically Thin Carbon Films.* Science, 2004. **306**(5696): p. 666-669.
4. Novoselov, K.S., et al., *Two-dimensional atomic crystals.* Proceedings of the National Academy of Sciences of the United States of America, 2005. **102**(30): p. 10451-10453.
5. Geim, A.K. and K.S. Novoselov, *The rise of graphene.* Nature Materials, 2007. **6**(3): p. 183-191.
6. Edvinsson, T., *Optical quantum confinement and photocatalytic properties in two-, one- and zero-dimensional nanostructures.* Royal Society Open Science, 2018. **5**(9): p. 180387.
7. Chaves, A., et al., *Bandgap engineering of two-dimensional semiconductor materials.* npj 2D Materials and Applications, 2020. **4**(1): p. 29.
8. Yang, L., et al., *Observation of superdiffusive phonon transport in aligned atomic chains.* Nature Nanotechnology, 2021.
9. Shirasaki, Y., et al., *Emergence of colloidal quantum-dot light-emitting technologies.* Nature Photonics, 2013. **7**(1): p. 13-23.
10. Velický, M. and P.S. Toth, *From two-dimensional materials to their heterostructures: An electrochemist's perspective.* Applied Materials Today, 2017. **8**: p. 68-103.
11. Tang, Q. and D.-e. Jiang, *Stabilization and Band-Gap Tuning of the 1T-MoS_2 Monolayer by Covalent Functionalization.* Chemistry of Materials, 2015. **27**(10): p. 3743-3748.
12. Lee, H.S., et al., *MoS_2 Nanosheet Phototransistors with Thickness-Modulated Optical Energy Gap.* Nano Lett., 2012. **12**(7): p. 3695-3700.
13. Wang, Q.H., et al., *Electronics and optoelectronics of two-dimensional transition metal dichalcogenides.* Nature Nanotechnology, 2012. **7**(11): p. 699-712.
14. Hong, T., et al., *Plasmonic Hot Electron Induced Photocurrent Response at MoS_2–Metal Junctions.* ACS Nano, 2015. **9**(5): p. 5357-5363.
15. Das, S., et al., *High Performance Multilayer MoS_2 Transistors with Scandium Contacts.* Nano Letters, 2013. **13**(1): p. 100-105.
16. Wang, H., et al., *Integrated Circuits Based on Bilayer MoS_2 Transistors.* Nano Letters, 2012. **12**(9): p. 4674-4680.
17. Lopez-Sanchez, O., et al., *Ultrasensitive photodetectors based on monolayer MoS2.* Nature Nanotechnology, 2013. **8**: p. 497.
18. Yin, Z., et al., *Single-Layer MoS_2 Phototransistors.* ACS Nano, 2012. **6**(1): p. 74-80.
19. Wang, Q.H., et al., *Electronics and optoelectronics of two-dimensional transition metal dichalcogenides.* Nature Nanotechnology, 2012. **7**: p. 699.
20. Radisavljevic, B., et al., *Single-layer MoS_2 transistors.* Nature Nanotechnology, 2011. **6**: p. 147.
21. Wang, T., et al., *High-Performance WSe_2 Phototransistors with 2D/2D Ohmic Contacts.* Nano Letters, 2018. **18**: p. 2766-2771.
22. Thakar, K. and S. Lodha, *Optoelectronic and photonic devices based on transition metal dichalcogenides.* Materials Research Express, 2020. **7**(1): p. 014002.

23. Smith, A.M., M.C. Mancini, and S. Nie, *Second window for in vivo imaging.* Nature Nanotechnology, 2009. **4**(11): p. 710-711.
24. Song, J., et al., *High-efficiency and high-speed germanium photodetector enabled by multiresonant photonic crystal.* Nanophotonics, 2021. **10**(3): p. 1081-1087.
25. Antoni Rogalski, M.K., Piotr Martyniuk, *Infrared Detector Characterization*, in *Antimonide-based Infrared Detectors: A New Perspective*. 2018.
26. Ornelas, C.D., et al., *Ultrafast Photocurrent Response and High Detectivity in Two-Dimensional $MoSe_2$-based Heterojunctions.* ACS Applied Materials & Interfaces, 2020. **12**(41): p. 46476-46482.
27. Wang, T. and Y.-Q. Xu, *Photonic Structure-Integrated Two-Dimensional Material Optoelectronics.* Electronics, 2016. **5**(4): p. 93.
28. Cutler, M. and N.F. Mott, *Observation of Anderson Localization in an Electron Gas.* Physical Review, 1969. **181**(3): p. 1336-&.
29. Buscema, M., et al., *Large and Tunable Photothermoelectric Effect in Single-Layer MoS2.* Nano Letters, 2013. **13**(2): p. 358-363.
30. Buscema, M., et al., *Photocurrent generation with two-dimensional van der Waals semiconductors.* Chemical Society Reviews, 2015. **44**(11): p. 3691-3718.
31. Youngblood, N., et al., *Waveguide-integrated black phosphorus photodetector with high responsivity and low dark current.* Nature Photonics, 2015. **9**(4): p. 247-252.
32. Groenendijk, D.J., et al., *Photovoltaic and Photothermoelectric Effect in a Double-Gated WSe_2 Device.* Nano Letters, 2014. **14**(10): p. 5846-5852.
33. Schottky, W., *Zur Halbleitertheorie der Sperrschicht- und Spitzengleichrichter.* Zeitschrift für Physik, 1939. **113**(5): p. 367-414.
34. Mott, N.F., *The theory of crystal rectifiers.* Proceedings of the Royal Society of London. Series A. Mathematical and Physical Sciences, 1939. **171**(944): p. 27-38.
35. Liu, Y., et al., *Approaching the Schottky–Mott limit in van der Waals metal–semiconductor junctions.* Nature, 2018. **557**(7707): p. 696-700.
36. Tung, R.T., *The physics and chemistry of the Schottky barrier height.* Applied Physics Reviews, 2014. **1**(1): p. 011304.
37. Zhang, K., et al., *Recent progress and challenges based on two-dimensional material photodetectors.* Nano Express, 2021. **2**(1): p. 012001.
38. Zhang, X., et al., *Near-ideal van der Waals rectifiers based on all-two-dimensional Schottky junctions.* Nature Communications, 2021. **12**(1): p. 1522.
39. Zhang, E., et al., *ReS_2-Based Field-Effect Transistors and Photodetectors.* Advanced Functional Materials, 2015. **25**(26): p. 4076-4082.
40. Hafeez, M., et al., *Chemical Vapor Deposition Synthesis of Ultrathin Hexagonal $ReSe_2$ Flakes for Anisotropic Raman Property and Optoelectronic Application.* Advanced Materials, 2016. **28**(37): p. 8296-8301.
41. Yu, X., et al., *Atomically thin noble metal dichalcogenide: a broadband mid-infrared semiconductor.* Nature Communications, 2018. **9**(1): p. 1545.
42. Li, L., et al., *Few-Layered PtS_2 Phototransistor on h-BN with High Gain.* Advanced Functional Materials, 2017. **27**(27): p. 1701011.
43. Oyedele, A.D., et al., *$PdSe_2$: Pentagonal Two-Dimensional Layers with High Air Stability for Electronics.* Journal of the American Chemical Society, 2017. **139**(40): p. 14090-14097.
44. Qin, D., et al., *Monolayer $PdSe_2$: A promising two-dimensional thermoelectric material.*

Scientific Reports, 2018. **8**(1): p. 2764.
45. Sun, M., et al., *Few-Layer $PdSe_2$ Sheets: Promising Thermoelectric Materials Driven by High Valley Convergence.* ACS Omega, 2018. **3**(6): p. 5971-5979.
46. Liu, X., et al., *Strain-Modulated Electronic Structure and Infrared Light Adsorption in Palladium Diselenide Monolayer.* Scientific Reports, 2017. **7**: p. 39995.
47. Sun, J., et al., *Electronic, transport, and optical properties of bulk and mono-layer $PdSe_2$.* Applied Physics Letters, 2015. **107**(15): p. 153902.
48. Chow, W.L., et al., *High Mobility 2D Palladium Diselenide Field-Effect Transistors with Tunable Ambipolar Characteristics.* Advanced Materials, 2017. **29**(21): p. 1602969.
49. Zhao, X., et al., *Spin Polarization Properties of Pentagonal $PdSe_2$ Induced by 3D Transition-Metal Doping: First-Principles Calculations.* Materials, 2018. **11**(11): p. 2339.
50. Das, S., et al., *High Performance Multilayer MoS2 Transistors with Scandium Contacts.* Nano Lett., 2012. **13**: p. 100-105.
51. Andrews, K., et al., *Improved Contacts and Device Performance in MoS_2 Transistors Using a 2D Semiconductor Interlayer.* ACS Nano, 2020. **14**(5): p. 6232-6241.
52. Allain, A., et al., *Electrical contacts to two-dimensional semiconductors.* Nature Materials, 2015. **14**(12): p. 1195-1205.
53. Kim, G.-S., et al., *Schottky Barrier Height Engineering for Electrical Contacts of Multilayered MoS_2 Transistors with Reduction of Metal-Induced Gap States.* ACS Nano, 2018. **12**(6): p. 6292-6300.
54. Wang, J., et al., *High Mobility MoS_2 Transistor with Low Schottky Barrier Contact by Using Atomic Thick h-BN as a Tunneling Layer.* Advanced Materials, 2016. **28**(37): p. 8302-8308.
55. Chen, J.-R., et al., *Control of Schottky Barriers in Single Layer MoS_2 Transistors with Ferromagnetic Contacts.* Nano Letters, 2013. **13**(7): p. 3106-3110.
56. Cui, X., et al., *Low-Temperature Ohmic Contact to Monolayer MoS_2 by van der Waals Bonded Co/h-BN Electrodes.* Nano Letters, 2017. **17**(8): p. 4781-4786.
57. Mott, N., F., *Impurity Band Conduction. Experiment And Theorythe Metal-Insulator Transition In An Impurity Band.* J. Phys. Colloques, 1976. **37**(C4): p. C4-301-C4-306.
58. Hong, T., et al., *Polarized photocurrent response in black phosphorus field-effect transistors.* Nanoscale, 2014. **6**(15): p. 8978-8983.
59. Xu, X., et al., *Photo-Thermoelectric Effect at a Graphene Interface Junction.* Nano Letters, 2010. **10**(2): p. 562-566.
60. Gabor, N.M., et al., *Hot Carrier–Assisted Intrinsic Photoresponse in Graphene.* Science, 2011. **334**(6056): p. 648-652.
61. Tsen, A.W., et al., *Imaging the electrical conductance of individual carbon nanotubes with photothermal current microscopy.* Nature Nanotechnology, 2009. **4**(2): p. 108-113.
62. Wang, T., et al., *Visualizing Light Scattering in Silicon Waveguides with Black Phosphorus Photodetectors.* Advanced Materials, 2016. **28**(33): p. 7162-7166.
63. Zuev, Y.M., W. Chang, and P. Kim, *Thermoelectric and Magnetothermoelectric Transport Measurements of Graphene.* Physical Review Letters, 2009. **102**(9).
64. Rosenblatt, S., et al., *High performance electrolyte gated carbon nanotube transistors.* Nano Letters, 2002. **2**(8): p. 869-872.
65. Li, E., et al., *Construction of bilayer $PdSe_2$ on epitaxial graphene.* Nano Research, 2018. **11**(11): p. 5858-5865.

66. Puretzky, A.A., et al., *Anomalous interlayer vibrations in strongly coupled layered PdSe2.* 2D Materials, 2018. **5**(3): p. 035016.
67. Chuang, H.-J., et al., *Low-Resistance 2D/2D Ohmic Contacts: A Universal Approach to High-Performance WSe2, MoS2, and MoSe2 Transistors.* Nano Letters, 2016. **16**(3): p. 1896-1902.
68. Tamalampudi, S.R., et al., *High Performance and Bendable Few-Layered InSe Photodetectors with Broad Spectral Response.* Nano Letters, 2014. **14**(5): p. 2800-2806.
69. Zhang, X., et al., *Photoconductivity of a Single Small-Molecule Organic Nanowire.* Advanced Materials, 2008. **20**(12): p. 2427-2432.
70. Bass, M., *Handbook of Optics: Devices, Measurements, and Properties*. 1994: McGraw-Hill Professoinal. 1568.
71. Geim, A.K. and I.V. Grigorieva, *Van der Waals heterostructures.* Nature, 2013. **499**(7459): p. 419-425.
72. Liu, Y., Y. Huang, and X. Duan, *Van der Waals integration before and beyond two-dimensional materials.* Nature, 2019. **567**(7748): p. 323-333.
73. Dean, C.R., et al., *Hofstadter's butterfly and the fractal quantum Hall effect in moiré superlattices.* Nature, 2013. **497**(7451): p. 598-602.
74. Cao, Y., et al., *Unconventional superconductivity in magic-angle graphene superlattices.* Nature, 2018. **556**(7699): p. 43-50.
75. Tan, C. and H. Zhang, *Epitaxial Growth of Hetero-Nanostructures Based on Ultrathin Two-Dimensional Nanosheets.* Journal of the American Chemical Society, 2015. **137**(38): p. 12162-12174.
76. Duan, X., et al., *Lateral epitaxial growth of two-dimensional layered semiconductor heterojunctions.* Nature Nanotechnology, 2014. **9**(12): p. 1024-1030.
77. Gong, Y., et al., *Vertical and in-plane heterostructures from WS2/MoS2 monolayers.* Nature Materials, 2014. **13**(12): p. 1135-1142.
78. Jariwala, D., T.J. Marks, and M.C. Hersam, *Mixed-dimensional van der Waals heterostructures.* Nature Materials, 2017. **16**(2): p. 170-181.
79. Mukherjee, S., et al., *Infrared tunable, two colour-band photodetectors on flexible platforms using 0D/2D PbS–MoS2 hybrids.* Nanoscale Advances, 2019. **1**(8): p. 3279-3287.
80. Wang, R., et al., *Probing photoresponse of aligned single-walled carbon nanotube doped ultrathin MoS2.* Nanotechnology, 2018. **29**(34): p. 345205.
81. Yao, J., Z. Zheng, and G. Yang, *Ultrasensitive 2D/3D Heterojunction Multicolor Photodetectors: A Synergy of Laterally and Vertically Aligned 2D Layered Materials.* ACS Applied Materials & Interfaces, 2018. **10**(44): p. 38166-38172.
82. Tan, J., et al., *Structure, Preparation, and Applications of 2D Material-Based Metal–Semiconductor Heterostructures.* Small Structures, 2021. **2**(1): p. 2000093.
83. Liu, X., et al., *Modulation of Quantum Tunneling via a Vertical Two-Dimensional Black Phosphorus and Molybdenum Disulfide p–n Junction.* ACS Nano, 2017. **11**(9): p. 9143-9150.
84. Xu, J., et al., *Tunneling field effect transistor integrated with black phosphorus-MoS2 junction and ion gel dielectric.* Applied Physics Letters, 2017. **110**(3): p. 033103.
85. Lim, S.K., et al., *Operation Mechanism of a MoS_2/BP Heterojunction FET.* Nanomaterials (Basel, Switzerland), 2018. **8**(10): p. 797.
86. Huang, M.Q., et al., *Multifunctional high-performance van der Waals heterostructures.*

Nature Nanotechnology, 2017. **12**(12): p. 1148-1155.
87. Jiang, X., et al., *Multifunctional black phosphorus/MoS2 van der Waals heterojunction.* Nanophotonics, 2020. **9**(8): p. 2487-2493.
88. Zong, X., et al., *Black phosphorus-based van der Waals heterostructures for mid-infrared light-emission applications.* Light: Science & Applications, 2020. **9**(1): p. 114.
89. Deng, Y., et al., *Black Phosphorus–Monolayer MoS 2 van der Waals Heterojunction p–n Diode.* ACS Nano, 2014. **8**(8): p. 8292-8299.
90. Chaojian, H., et al., *Plasmon-Enhanced Photovoltaic Characteristics of Black Phosphorus-MoS2 Heterojunction.* IEEE Open Journal of Nanotechnology, 2021. **2**: p. 41-51.
91. Xiao, S., et al., *Nonlinear optical modulation of MoS2/black phosphorus/MoS2 at 1550 nm.* Physica B: Condensed Matter, 2020. **594**: p. 412364.
92. Mak, K.F., et al., *Atomically thin MoS2: A new direct-gap semiconductor.* Physical Review Letters, 2010. **105**(13): p. 136805-136805.
93. Liu, H., et al., *Phosphorene: An Unexplored 2D Semiconductor with a High Hole Mobility.* ACS Nano, 2014. **8**(4): p. 4033-4041.
94. Buscema, M., et al., *Fast and Broadband Photoresponse of Few-Layer Black Phosphorus Field-Effect Transistors.* Nano Letters, 2014. **14**(6): p. 3347-3352.
95. Deng, Y., et al., *Black Phosphorus–Monolayer MoS2 van der Waals Heterojunction p–n Diode.* ACS Nano, 2014. **8**(8): p. 8292-8299.
96. Ye, L., et al., *Near-Infrared Photodetector Based on MoS2/Black Phosphorus Heterojunction.* ACS Photonics, 2016. **3**(4): p. 692-699.
97. Yuan, H., et al., *Polarization-sensitive broadband photodetector using a black phosphorus vertical p–n junction.* Nature Nanotechnology, 2015. **10**(8): p. 707-713.
98. Liu, Y., et al., *Highly responsive broadband black phosphorus photodetectors.* Chinese Optics Letters, 2018. **16**(2): p. 020002.
99. Huang, M., et al., *Broadband Black-Phosphorus Photodetectors with High Responsivity.* Advanced Materials, 2016. **28**(18): p. 3481-3485.
100. Lopez-Sanchez, O., et al., *Ultrasensitive photodetectors based on monolayer MoS2.* Nature Nanotechnology, 2013. **8**(7): p. 497-501.
101. Choi, W., et al., *High-detectivity multilayer MoS2 phototransistors with spectral response from ultraviolet to infrared.* Advanced Materials, 2012. **24**(43): p. 5832-5836.
102. Ye, L., et al., *Near-Infrared Photodetector Based on MoS 2 /Black Phosphorus Heterojunction.* ACS Photonics, 2016. **3**(4): p. 692-699.
103. Zheng, S., et al., *Acoustically enhanced photodetection by a black phosphorus–MoS2 van der Waals heterojunction p–n diode.* Nanoscale, 2018. **10**(21): p. 10148-10153.
104. Wang, L., et al., *Perovskite/Black Phosphorus/MoS2 Photogate Reversed Photodiodes with Ultrahigh Light On/Off Ratio and Fast Response.* ACS Nano, 2019. **13**(4): p. 4804-4813.
105. Bass, M., *Handbook of Optics: Devices, Measurements, and Properties.* 1994: McGraw-Hill Professoinal:.
106. Chen, P., et al., *Gate tunable MoS2-black phosphorus heterojunction devices.* 2d Materials, 2015. **2**(3).
107. Kim, T.-Y., et al., *Transparent Large-Area MoS_2 Phototransistors with Inkjet-Printed Components on Flexible Platforms.* ACS Nano, 2017. **11**(10): p. 10273-10280.
108. Radisavljevic, B., et al., *Single-layer MoS_2 transistors.* Nature Nanotechnology, 2011.

6(3): p. 147-150.
109. Yue, D., et al., *Passivated ambipolar black phosphorus transistors.* Nanoscale, 2016. **8**(25): p. 12773-12779.
110. Chen, X., et al., *High-quality sandwiched black phosphorus heterostructure and its quantum oscillations.* Nature Communications, 2015. **6**(1): p. 7315.
111. Koenig, S.P., et al., *Electric field effect in ultrathin black phosphorus.* Applied Physics Letters, 2014. **104**(10): p. 103106.
112. Ju, L., et al., *Photoinduced doping in heterostructures of graphene and boron nitride.* Nature Nanotechnology, 2014. **9**(5): p. 348-352.
113. Lee, C.-H., et al., *Atomically thin p–n junctions with van der Waals heterointerfaces.* Nat. Nanotechnol., 2014. **9**: p. 676.
114. Rose, A., *Recombination Processes in Insulators and Semiconductors.* Physical Review, 1955. **97**(2): p. 322-333.
115. Zhao, Q., et al., *The role of traps in the photocurrent generation mechanism in thin InSe photodetectors.* Materials Horizons, 2020. **7**(1): p. 252-262.
116. Ghatak, S., A.N. Pal, and A. Ghosh, *Nature of Electronic States in Atomically Thin MoS2 Field-Effect Transistors.* ACS Nano, 2011. **5**(10): p. 7707-7712.
117. Hong, T., et al., *Anisotropic photocurrent response at black phosphorus-*MoS_2 *p-n heterojunctions.* Nanoscale, 2015. **7**(44): p. 18537-18541.
118. Sazonova, V., et al., *A tunable carbon nanotube electromechanical oscillator.* Nature, 2004. **431**(7006): p. 284-287.
119. Freitag, M., et al., *Imaging of the schottky barriers and charge depletion in carbon nanotube transistors.* Nano Letters, 2007. **7**(7): p. 2037-2042.
120. Ahn, Y., J. Dunning, and J. Park, *Scanning photocurrent imaging and electronic band studies in silicon nanowire field effect transistors.* Nano Letters, 2005. **5**(7): p. 1367-1370.
121. Peng, C., et al., *Gate tunable MoS 2 –black phosphorus heterojunction devices.* 2D Materials, 2015. **2**(3): p. 034009.
122. Jiang, X., et al., *A Symmetric Tunnel Field-Effect Transistor Based on MoS2/Black Phosphorus/MoS2 Nanolayered Heterostructures.* ACS Applied Nano Materials, 2019. **2**(9): p. 5674-5680.
123. Cao, B., et al., *Low temperature photoresponse of monolayer tungsten disulphide.* APL Materials, 2014. **2**(11): p. 116101.
124. Yoo, G., et al., *Flexible and Wavelength-Selective MoS2 Phototransistors with Monolithically Integrated Transmission Color Filters.* Scientific Reports, 2017. **7**: p. 40945.
125. Lopez-Sanchez, O., et al., *Ultrasensitive photodetectors based on monolayer* MoS_2. Nat. Nanotechnol., 2013. **8**: p. 497.
126. Perera, M.M., et al., *Improved Carrier Mobility in Few-Layer MoS2 Field-Effect Transistors with Ionic-Liquid Gating.* ACS Nano, 2013. **7**(5): p. 4449-4458.
127. Chamlagain, B., et al., *Mobility Improvement and Temperature Dependence in MoSe 2 Field-Effect Transistors on Parylene-C Substrate.* ACS Nano, 2014. **8**(5): p. 5079-5088.
128. Lee, H., et al., *High-Responsivity Multilayer MoSe2 Phototransistors with Fast Response Time.* Scientific Reports, 2018. **8**(1): p. 11545-11545.
129. Quereda, J., et al., *Observation of bright and dark exciton transitions in monolayer MoSe 2 by photocurrent spectroscopy.* 2D Materials, 2017. **5**(1): p. 015004-015004.

130. Arora, A., et al., *Exciton band structure in layered MoSe 2 : from a monolayer to the bulk limit.* Nanoscale, 2015. **7**(48): p. 20769-20775.
131. Hanbicki, A.T., et al., *Double Indirect Interlayer Exciton in a MoSe 2 /WSe 2 van der Waals Heterostructure.* ACS Nano, 2018. **12**(5): p. 4719-4726.
132. Ambrosi, A., Z. Sofer, and M. Pumera, *2H → 1T phase transition and hydrogen evolution activity of MoS2, MoSe2, WS2 and WSe2 strongly depends on the MX2 composition.* Chemical Communications, 2015. **51**(40): p. 8450-8453.
133. Hossain, M., et al., *Recent Advances in Two-Dimensional Materials with Charge Density Waves: Synthesis, Characterization and Applications.* Crystals, 2017. **7**(10): p. 298.
134. Ogawa, N. and K. Miyano, *Charge-density wave as an electro-optical switch and memory.* Applied Physics Letters, 2002. **80**(17): p. 3225-3227.
135. Mihailovic, D., et al., *Femtosecond data storage, processing, and search using collective excitations of a macroscopic quantum state.* Applied Physics Letters, 2002. **80**(5): p. 871-873.
136. Adelman, T.L., S.V. Zaitsev-Zotov, and R.E. Thorne, *Field-Effect Modulation of Charge-Density-Wave Transport in*$NbSe_3$ *and* TaS_3. Physical Review Letters, 1995. **74**(26): p. 5264-5267.
137. Tissen, V.G., et al., *Pressure dependence of superconducting critical temperature and upper critical field of 2H-NbS${}_{2}$.* Physical Review B, 2013. **87**(13): p. 134502.
138. Valla, T., et al., *Quasiparticle Spectra, Charge-Density Waves, Superconductivity, and Electron-Phonon Coupling in $2\mathrm{H}\mathrm{\text{\ensuremath{-}}}{\mathrm{N}\mathrm{b}\mathrm{S}\mathrm{e}}_{2}$.* Physical Review Letters, 2004. **92**(8): p. 086401.
139. Sipos, B., et al., *From Mott state to superconductivity in 1T-TaS2.* Nature Materials, 2008. **7**(12): p. 960-965.
140. Luo, H., et al., *Polytypism, polymorphism, and superconductivity in TaSe₂_{−x}Te_x.* Proceedings of the National Academy of Sciences, 2015. **112**(11): p. E1174-E1180.
141. Dardel, B., et al., *Spectroscopic observation of charge-density-wave-induced changes in the electronic structure of 2H-TaSe2.* Journal of Physics: Condensed Matter, 1993. **5**(33): p. 6111-6119.
142. Wang, L., et al., *Distinctive Performance of Terahertz Photodetection Driven by Charge-Density-Wave Order in CVD-Grown Tantalum Diselenide.* Advanced Functional Materials, 2019. **29**(45): p. 1905057.
143. Li, L.J., et al., *Controlling many-body states by the electric-field effect in a two-dimensional material.* Nature, 2016. **529**(7585): p. 185-189.
144. Goli, P., et al., *Charge Density Waves in Exfoliated Films of van der Waals Materials: Evolution of Raman Spectrum in TiSe2.* Nano Letters, 2012. **12**(11): p. 5941-5945.
145. Di Salvo, F.J., D.E. Moncton, and J.V. Waszczak, *Electronic properties and superlattice formation in the semimetal* $TiSe_2$. Physical Review B, 1976. **14**(10): p. 4321-4328.
146. Lian, C., et al., *Ultrafast charge ordering by self-amplified exciton–phonon dynamics in TiSe2.* Nature Communications, 2020. **11**(1): p. 43.
147. Wu, D., et al., *Ultrabroadband photosensitivity from visible to terahertz at room temperature.* Science Advances, 2018. **4**(8): p. eaao3057.
148. Yan, C., et al., *2D Group IVB Transition Metal Dichalcogenides.* Advanced Functional Materials, 2018. **28**(39): p. 1803305.

149. Wan, C., et al., *Flexible n-type thermoelectric materials by organic intercalation of layered transition metal dichalcogenide TiS_2.* Nature Materials, 2015. **14**(6): p. 622-627.
150. Ge, Y., et al., *Broadband Nonlinear Photoresponse of 2D TiS_2 for Ultrashort Pulse Generation and All-Optical Thresholding Devices.* Advanced Optical Materials, 2018. **6**(4): p. 1701166.
151. Fiori, G., et al., *Electronics based on two-dimensional materials.* Nature Nanotechnology, 2014. **9**(10): p. 768-779.
152. Zhang, W., et al., *Two-dimensional semiconductors with possible high room temperature mobility.* Nano Research, 2014. **7**(12): p. 1731-1737.
153. Yin, L., et al., *Ultrafast and ultrasensitive phototransistors based on few-layered $HfSe_2$.* Applied Physics Letters, 2016. **109**(21): p. 213105.
154. Holy, J.A., et al., *Raman and infrared studies of superlattice formation in $TiSe_2$.* Physical Review B, 1977. **16**(8): p. 3628-3637.
155. Snow, C.S., et al., *Quantum Melting of the Charge-Density-Wave State in 1T-$TiSe_2$.* Physical Review Letters, 2003. **91**(13): p. 136402.
156. Wang, H., et al., *Large-Area Atomic Layers of the Charge-Density-Wave Conductor $TiSe_2$.* Advanced Materials, 2018. **30**(8): p. 1704382.
157. Chen, P., et al., *Charge density wave transition in single-layer titanium diselenide.* Nature Communications, 2015. **6**(1): p. 8943.
158. Sugawara, K., et al., *Unconventional Charge-Density-Wave Transition in Monolayer 1T-$TiSe_2$.* ACS Nano, 2016. **10**(1): p. 1341-1345.
159. Chen, P., et al., *Hidden Order and Dimensional Crossover of the Charge Density Waves in $TiSe_2$.* Scientific Reports, 2016. **6**(1): p. 37910.
160. Chen, P., et al., *Dimensional Effects on the Charge Density Waves in Ultrathin Films of $TiSe_2$.* Nano Letters, 2016. **16**(10): p. 6331-6336.
161. Xu, S.-Y., et al., *Spontaneous gyrotropic electronic order in a transition-metal dichalcogenide.* Nature, 2020. **578**(7796): p. 545-549.
162. Zan, R., et al., *Control of Radiation Damage in MoS2 by Graphene Encapsulation.* ACS Nano, 2013. **7**(11): p. 10167-10174.
163. Hasegawa, H. and T. Sawada, *On the electrical properties of compound semiconductor interfaces in metal/insulator/ semiconductor structures and the possible origin of interface states.* Thin Solid Films, 1983. **103**(1): p. 119-140.
164. Heine, V., *Theory of Surface States.* Physical Review, 1965. **138**(6A): p. A1689-A1696.
165. Chaves, F.A. and D. Jiménez, *The Role of the Fermi Level Pinning in Gate Tunable Graphene-Semiconductor Junctions.* IEEE Transactions on Electron Devices, 2016. **63**(11): p. 4521-4526.
166. Schulman, D.S., A.J. Arnold, and S. Das, *Contact engineering for 2D materials and devices.* Chemical Society Reviews, 2018. **47**(9): p. 3037-3058.
167. Kim, C., et al., *Fermi Level Pinning at Electrical Metal Contacts of Monolayer Molybdenum Dichalcogenides.* ACS Nano, 2017. **11**(2): p. 1588-1596.
168. Sotthewes, K., et al., *Universal Fermi-Level Pinning in Transition-Metal Dichalcogenides.* The Journal of Physical Chemistry C, 2019. **123**(9): p. 5411-5420.
169. Spicer, W.E., et al., *The surface electronic structure of 3–5 compounds and the mechanism of Fermi level pinning by oxygen (passivation) and metals (Schottky barriers).* Surface Science, 1979. **86**: p. 763-788.
170. Liu, Y., et al., *Van der Waals heterostructures and devices.* Nature Reviews Materials,

2016. **1**(9): p. 16042.
171. Novoselov, K.S., et al., *2D materials and van der Waals heterostructures.* Science, 2016. **353**(6298): p. aac9439.
172. Gong, C., et al., *The Unusual Mechanism of Partial Fermi Level Pinning at Metal–MoS2 Interfaces.* Nano Letters, 2014. **14**(4): p. 1714-1720.
173. Liu, Y., P. Stradins, and S.-H. Wei, *Van der Waals metal-semiconductor junction: Weak Fermi level pinning enables effective tuning of Schottky barrier.* Science Advances, 2016. **2**(4): p. e1600069.
174. Farmanbar, M. and G. Brocks, *First-principles study of van der Waals interactions and lattice mismatch at ${\mathrm{MoS}}_{2}/\text{metal}$ interfaces.* Physical Review B, 2016. **93**(8): p. 085304.
175. Desai, S.B., et al., *Gold-Mediated Exfoliation of Ultralarge Optoelectronically-Perfect Monolayers.* Advanced Materials, 2016. **28**(21): p. 4053-4058.
176. Wang, T., et al., *Tunneling Effects in Crossed Ta2Pt3Se8–Ta2Pd3Se8 Nanowire Junctions: Implications for Anisotropic Photodetectors.* ACS Applied Nano Materials, 2021. **4**(2): p. 1817-1824.
177. Jang, A.R., et al., *Reversibly Light-Modulated Dirac Point of Graphene Functionalized with Spiropyran.* ACS Nano, 2012. **6**(10): p. 9207-9213.
178. Guo, B., et al., *Controllable N-Doping of Graphene.* Nano Letters, 2010. **10**(12): p. 4975-4980.
179. Zhang, X., T.S. Walmsley, and Y.-Q. Xu, *In situ monitoring of electrical and optoelectronic properties of suspended graphene ribbons during laser-induced morphological changes.* Nanoscale Advances, 2020.
180. Bing, D., et al., *Optical contrast for identifying the thickness of two-dimensional materials.* Optics Communications, 2018. **406**: p. 128-138.
181. Li, H., et al., *Rapid and Reliable Thickness Identification of Two-Dimensional Nanosheets Using Optical Microscopy.* ACS Nano, 2013. **7**(11): p. 10344-10353.
182. Sun, L., et al., *Suppression of the Charge Density Wave State in Two-Dimensional 1T-$TiSe_2$ by Atmospheric Oxidation.* Angewandte Chemie International Edition, 2017. **56**(31): p. 8981-8985.
183. Wang, Y., et al., *Transport properties of a few nanometer-thick $TiSe_2$ films grown by molecular-beam epitaxy.* Applied Physics Letters, 2018. **113**(7): p. 073101.
184. Watson, M.D., A.M. Beales, and P.D.C. King, *On the origin of the anomalous peak in the resistivity of $TiSe_2$.* Physical Review B, 2019. **99**(19): p. 195142.
185. Uchida, S. and S. Sugai, *Infrared and Raman studies on commensurate CDW states in transition metal dichalcogenides.* Physica B+C, 1981. **105**(1): p. 393-399.
186. Temple, P.A. and C.E. Hathaway, *Multiphonon Raman Spectrum of Silicon.* Physical Review B, 1973. **7**(8): p. 3685-3697.
187. Li, I.L., et al., *Resonant Raman study of confined Se single helix and Se8 rings.* Applied Physics Letters, 2005. **87**(7): p. 071902.
188. Poborchii, V.V., et al., *Dynamics of Single Selenium Chains Confined in One-Dimensional Nanochannels of $AlPO_4$-5: Temperature Dependencies of the First- and Second-Order Raman Spectra.* Physical Review Letters, 1999. **82**(9): p. 1955-1958.
189. Walmsley, T.S., et al., *Gate-Tunable Photoresponse Time in Black Phosphorus–MoS_2 Heterojunctions.* Advanced Optical Materials, 2019. **7**(5): p. 1800832.
190. Nayeb Sadeghi, S., M. Zebarjadi, and K. Esfarjani, *Non-linear enhancement of*

thermoelectric performance of a $TiSe_2$ monolayer due to tensile strain, from first-principles calculations. Journal of Materials Chemistry C, 2019. **7**(24): p. 7308-7317.
191. Lakhani, A.A., et al., *Thermoelectric power of $TiSe_{2-x}S_x$.* Physical Review B, 1983. **28**(4): p. 1978-1982.
192. Lopez-Castillo, J.M., et al., *Phonon-drag effect in $TiSe_{2-x}S_x$ mixed compounds.* Physical Review B, 1987. **36**(8): p. 4249-4253.
193. McIver, J.W., et al., *Control over topological insulator photocurrents with light polarization.* Nature Nanotechnology, 2012. **7**(2): p. 96-100.
194. Zhang, Y., et al., *Photothermoelectric and photovoltaic effects both present in MoS2.* Scientific Reports, 2015. **5**(1): p. 7938.
195. Massicotte, M., et al., *Dissociation of two-dimensional excitons in monolayer WSe2.* Nature Communications, 2018. **9**(1): p. 1633.
196. Guo, X., et al., *High-performance graphene photodetector using interfacial gating.* Optica, 2016. **3**(10): p. 1066-1070.
197. Kang, C.G., et al., *Intrinsic photocurrent characteristics of graphene photodetectors passivated with Al2O3.* Optics Express, 2013. **21**(20): p. 23391-23400.
198. Li, G., et al., *Semimetal-to-Semimetal Charge Density Wave Transition in $TiSe_2$.* Physical Review Letters, 2007. **99**(2): p. 027404.
199. Wang, L., et al., *Toward Sensitive Room-Temperature Broadband Detection from Infrared to Terahertz with Antenna-Integrated Black Phosphorus Photoconductor.* Advanced Functional Materials, 2017. **27**(7): p. 1604414.
200. Wu, J., et al., *Enhanced photoresponse of highly air-stable palladium diselenide by thickness engineering.* Nanophotonics, 2020. **9**(8): p. 2467-2474.
201. Wei, R., et al., *Ultrafast and large optical nonlinearity of a TiSe2 saturable absorber in the 2 μm wavelength region.* Nanoscale, 2019. **11**(46): p. 22277-22285.
202. Velebit, K., et al., *Scattering-dominated high-temperature phase of 1T-$TiSe_2$: An optical conductivity study.* Physical Review B, 2016. **94**(7): p. 075105.
203. Cheney, N., J. Clune, and H. Lipson. *Evolved Electrophysiological Soft Robots*. in *ALIFE 14: The Fourteenth International Conference on the Synthesis and Simulation of Living Systems*. 2014.
204. Novak, P., et al., *Nanoscale-Targeted Patch-Clamp Recordings of Functional Presynaptic Ion Channels.* Neuron, 2013. **79**(6): p. 1067-1077.
205. Fairless, R., et al., *Membrane Potential Measurements of Isolated Neurons Using a Voltage-Sensitive Dye.* PLOS ONE, 2013. **8**(3): p. e58260.
206. Kelly, R.C., et al., *Comparison of Recordings from Microelectrode Arrays and Single Electrodes in the Visual Cortex.* The Journal of Neuroscience, 2007. **27**(2): p. 261-264.
207. Zhang, Y., et al., *Probing electrical signals in the retina via graphene-integrated microfluidic platforms.* Nanoscale, 2016. **8**(45): p. 19043-19049.
208. Kojima, D., et al., *UV-Sensitive Photoreceptor Protein OPN5 in Humans and Mice.* PLOS ONE, 2011. **6**(10): p. e26388.
209. Wang, R., et al., *Ultrasensitive Graphene Optoelectronic Probes for Recording Electrical Activities of Individual Synapses.* Nano Letters, 2018. **18**(9): p. 5702-5708.
210. Masvidal-Codina, E., et al., *High-resolution mapping of infraslow cortical brain activity enabled by graphene microtransistors.* Nature Materials, 2019. **18**(3): p. 280-288.
211. Rastogi, S.K., et al., *Graphene Microelectrode Arrays for Electrical and Optical Measurements of Human Stem Cell-Derived Cardiomyocytes.* Cellular and Molecular

Bioengineering, 2018. **11**(5): p. 407-418.
212. Reinhard, K., et al., *Step-By-Step Instructions for Retina Recordings with Perforated Multi Electrode Arrays.* PLOS ONE, 2014. **9**(8): p. e106148.
213. Obien, M.E.J., et al., *Revealing neuronal function through microelectrode array recordings.* Frontiers in Neuroscience, 2015. **8**(423).
214. Bean, B.P., *The action potential in mammalian central neurons.* Nature Reviews Neuroscience, 2007. **8**(6): p. 451-465.
215. Henze, D.A., et al., *Intracellular Features Predicted by Extracellular Recordings in the Hippocampus In Vivo.* Journal of Neurophysiology, 2000. **84**(1): p. 390-400.
216. Pettersen, K.H. and G.T. Einevoll, *Amplitude Variability and Extracellular Low-Pass Filtering of Neuronal Spikes.* Biophysical Journal, 2008. **94**(3): p. 784-802.
217. Sanes, J.R. and R.H. Masland, *The Types of Retinal Ganglion Cells: Current Status and Implications for Neuronal Classification.* Annual Review of Neuroscience, 2015. **38**(1): p. 221-246.
218. Zhong, Y.S., et al., *Potassium ion channels in retinal ganglion cells (Review).* Mol Med Rep, 2013. **8**(2): p. 311-319.
219. Dacey, D.M. and S. Brace, *A coupled network for parasol but not midget ganglion cells in the primate retina.* Visual Neuroscience, 1992. **9**(3-4): p. 279-290.
220. Rey, H.G., C. Pedreira, and R. Quian Quiroga, *Past, present and future of spike sorting techniques.* Brain Research Bulletin, 2015. **119**: p. 106-117.
221. Rall, W., *Electrophysiology of a Dendritic Neuron Model.* Biophysical Journal, 1962. **2**(2, Part 2): p. 145-167.
222. R, L.d.N., *A study of nerve physiology.* Stud Rockefeller Inst Med Res Repr, 1947. **131**: p. 1-496.
223. Terzuolo, C.A. and T. Araki, *An analysis of intra- versus extracellular potential changes associated with activity of single spinal motoneurons.* Ann N Y Acad Sci, 1961. **94**: p. 547-58.
224. Heinricher, M.M., *Principles of Extracellualr Single-Unit Recording*, in *Microelectrode recording in Movement Diosrder Surgery*, K.J.B. Zvi Israel, Editor. 2004, Thieme Medical Publishers: New York. NY. p. 8-13.
225. Rosa, C.J.L.d.l., et al., *Frame assisted H2O electrolysis induced H2 bubbling transfer of large area graphene grown by chemical vapor deposition on Cu.* Applied Physics Letters, 2013. **102**(2): p. 022101.
226. Ishikawa, M., et al., *Effects of acutely elevated hydrostatic pressure in a rat ex vivo retinal preparation.* Investigative ophthalmology & visual science, 2010. **51**(12): p. 6414-6423.
227. Wang, D., et al., *Wafer-Scale Growth of Pristine and Doped Monolayer MoS2 Films for Electronic Device Applications.* Inorganic Chemistry, 2020. **59**(23): p. 17356-17363.
228. Masubuchi, S., et al., *Deep-learning-based image segmentation integrated with optical microscopy for automatically searching for two-dimensional materials.* npj 2D Materials and Applications, 2020. **4**(1): p. 3.
229. Han, B., et al., *Deep-Learning-Enabled Fast Optical Identification and Characterization of 2D Materials.* Advanced Materials, 2020. **32**(29): p. 2000953.
230. Masubuchi, S., et al., *Autonomous robotic searching and assembly of two-dimensional crystals to build van der Waals superlattices.* Nature Communications, 2018. **9**(1): p. 1413.

231. Ames, A., 3rd and F.B. Nesbett, *In vitro retina as an experimental model of the central nervous system.* J Neurochem, 1981. **37**(4): p. 867-77.